2-1-2012

Utilizing equivalent circuits to describe the strain- and temperature-dependence of electromagnetic metamaterials

Brandon Arritt

Brandon J. Arritt
Candidate

DEPARTMENT OF MECHANICAL ENGINEERING
Department

This dissertation is approved, and it is acceptable in quality and form for publication:

Approved by the Dissertation Committee:

Tariq A. Khraishi, Chairperson

David R. Smith

Yu-Lin Shen

Jeffry S. Welsh

UTILIZING EQUIVALENT CIRCUITS TO DESCRIBE THE STRAIN- AND TEMPERATURE-DEPENDENCE OF ELECTROMAGNETIC METAMATERIALS

BY

BRANDON J. ARRITT

B.S., Mechanical Engineering, The United States Air Force Academy, 1998
M.S., Mechanical Engineering, The George Washington University, 1999

DISSERTATION

Submitted in Partial Fulfillment of the
Requirements for the Degree of
Doctor of Philosophy

Engineering

The University of New Mexico
Albuquerque, New Mexico

December, 2011

ACKNOWLEDGMENTS

This would not have been possible without the help and support of a lot of people. To my advisor, Professor Tariq Khraishi, thank you for your guidance, patience, and support. Your timely advice was instrumental in keeping me focused and moving forward. Professor David Smith, thank you for the hospitality and support that you and your whole group showed me out at Duke University. I don't believe I could have ever finished this without your help. To my professional mentor, Dr. Jeffry Welsh, thank you for taking a chance and hiring me all those years ago, and for pushing me to challenge myself and continue my education. Professor Yu-Lin Shen, thank you for your time and efforts and the distinct honor of having you serve on my committee.

I have the great pleasure of working with an extraordinary Team at the Air Force Research Laboratory/Space Vehicles Directorate. I am especially grateful for the world-class expertise and contributions from Mr. Greg Sanford, Dr. Emil Ardelean, and 1Lt. Bryan Adomanis. I want to acknowledge the help from Mr. Bryan Justice and Mr. Vihn Nguyen who were instrumental in teaching a mechanical engineer how to use RF test equipment. And thank you to Dr. Anthony Starr, who along with Professor Smith, is the person most responsible for focusing my research interests in this direction.

I would like to thank my parents for the innumerable lessons they taught me throughout my life. Thank you for setting the example I hope to pass onto my kids.

To my children; thank you for your love, patience, and understanding. I am sorry for all the times I could not go play and instead had to go do my homework. And thank you for all the words of encouragement and hugs when things weren't progressing according to plan. Most importantly, I am eternally grateful for the love and support of

my best friend: my amazing wife. You paid the biggest price in this endeavor, yet you continued to selflessly push me onward. I look forward to again spending my evenings with you, and not this blasted computer.

BRANDON J. ARRITT

UTILIZING EQUIVALENT CIRCUITS TO DESCRIBE THE STRAIN- AND TEMPERATURE-DEPENDENCE OF ELECTROMAGNETIC METAMATERIALS

BY

BRANDON J. ARRITT

ABSTRACT OF DISSERTATION

Submitted in Partial Fulfillment of the
Requirements for the Degree of

Doctor of Philosophy

Engineering

The University of New Mexico
Albuquerque, New Mexico

December, 2011

UTILIZING EQUIVALENT CIRCUITS TO DESCRIBE THE STRAIN- AND TEMPERATURE-DEPENDENCE OF ELECTROMAGNETIC METAMATERIALS

by

Brandon J. Arritt

B.S., Mechanical Engineering, The United Stated Air Force Academy
M.S., Mechanical Engineering, The George Washington University
Ph.D., Engineering, The University of New Mexico

ABSTRACT

Electromagnetic metamaterials have demonstrated unique and unprecedented behaviors in a laboratory setting. They achieve these novel properties by utilizing geometry and structure, as opposed to a strict reliance on chemical composition, to dictate their interactions with electromagnetic (EM) radiation. As such, metamaterials significantly expand the toolkit from which engineers can draw when designing devices that interact with EM waves. However, the flexibility afforded by these structures also implies environmental sensitivities not seen in traditional material systems. Some recent efforts have bore this out; demonstrating significant strain- and temperature-dependence in metamaterial samples.

To date, little has been done to fundamentally understand the mechanisms driving these dependencies. This understanding is crucial for developing engineering-quality predictions of the EM performance of metamaterial structures in a relevant environment; a crucial step in transitioning this technology from laboratory novelty to fielded capability.

This study leverages equivalent circuit models to understand and predict the strain- and temperature-dependent EM properties of metamaterial structures. Straightforward analytic expressions for the equivalent circuit parameters (resistance, inductance, capacitance) detail the strain-induced changes in geometry as well as the temperature-dependence of the metamaterial's constituent materials. These expressions are initially utilized to predict the strain-dependent shift in resonant frequency; a key descriptor of the metamaterial's EM behavior. These same expressions are then utilized to describe the metamaterial's strain- and temperature-dependent EM constitutive properties (permittivity, ε, and permeability, μ), which are critical for solving Maxwell's equations and performing EM simulations within the material.

This study focused on the Electric-LC (ELC) resonator; a design commonly used to provide a tailored response to the electric field of the EM wave. However, the author believes that the same process, and similar analytic expressions for the circuit parameters and constitutive properties, could be used to successfully predict the strain- and temperature-dependence of other metamaterial structures, to include Split-Ring-Resonators (SRRs), a design commonly used to provide a tailored magnetic response to EM waves.

TABLE OF CONTENTS

LIST OF FIGURES

LIST OF TABLES

GLOSSARY

Dielectric Constant	See Permittivity
Index of Refraction	(η) Ratio of the speed of light in vacuum, to the phase velocity in the medium of interest: $\eta = \frac{c}{v_p}$. Can be less than one, or negative.
Group Velocity	The speed of light in a medium. Always less than the speed of light in a vacuum. The speed at which information is propagated.
Permeability	(μ) a measure of the change in magnetic induction produced when a magnetic material replaces air, expressed as a coefficient or a set of coefficients that multiply the components of magnetic intensity to give the components of magnetic induction [1]. Is technically a 2^{nd} order tensor (denoted by bold faced font), composed of complex variables (**μ**).
Permittivity	(ε) A measure of the ability of a material to resist the formation of an electric field within it, equal to the ratio between the electric flux density and the electric field strength generated by an electric charge in the material [1]. Also called the dielectric constant. As with the permeability, also a complex, 2^{nd} order tensor (**ε**).
Phase Velocity	(v_p) The velocity with which a simple harmonic wave is propagated, equal to the wavelength divided by the period of vibration [2]. Note: can be higher than the speed of light.
Polarization	Describes the plane of the electric field in an electromagnetic wave.

Q/Quality-Factor — For resonant structures, describes the sharpness, or steepness of the response. In Figure 1, it is $f_0/\Delta f$, where f_0 is the resonant frequency, and Δf is the width at half the maximum power.

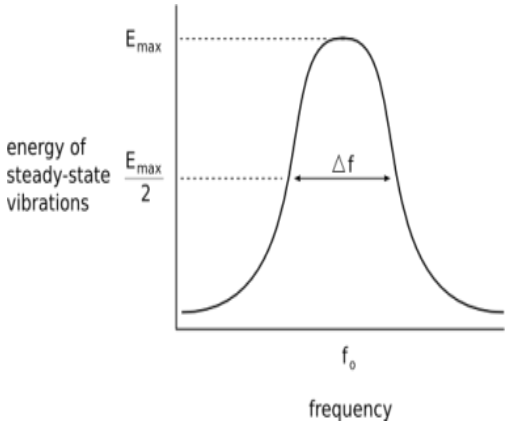

Figure 1. *Quality Factor (Q) for a resonant structure.*

RF — Radio Frequency. GHz/Microwaves fall within this regime.

S parameters — Scattering parameters. Specifically S11, S12, S21, S22. S11 and S22 describe the relative power of the reflection off a sample and S12 and S21 describe the relative transmission through a sample. S21 refers to the power of the signal, received at 2, normalized by what was transmitted at 1. Often presented on a power dB scale, where doubling a quantity equates to a change of ~6 dB [$dB=20\log_{10}(P2/P1)$].

Wavenumber — (k) The angular frequency divided by the phase velocity ($k=2\pi f/v_p$)

1 INTRODUCTION

1.1 RELEVANCE OF THE RESEARCH

Over the last decade, the nascent field of ElectroMagnetic (EM) metamaterials has received an extraordinary amount of interest [3]. Metamaterials [4] are artificially structured composite materials, made by patterning subwavelength inclusions, which yield effective medium behaviors that can be equivalently described as homogeneous materials with effective constitutive parameters: i.e., permittivity and permeability [5][6][7][8]. This is analogous to mechanical systems, where a complex medium consisting of innumerable molecular and atomic bonds, grain boundaries, engineering composites, etc., can be equivalently described via effective parameters (e.g. stiffness and thermal conductivity tensors). Metamaterials can exhibit electromagnetic properties difficult or even impossible to achieve with naturally occurring materials; one of the most widely known being Negative Index of refraction Materials (NIM). The ability to design and deliver novel electromagnetic properties (reflectivity, absorptivity, transmittance, index of refraction, wave impedance, and negative phase advance) opens a world of possibilities and potentially conveys unprecedented capabilities for a variety of applications. As a result, multiple government agencies, industry, and academia have invested heavily in the development of metamaterials for a wide range of frequencies of interest [9].

At microwave frequencies, where wavelengths are of length scales equal to or greater than centimeters, associated devices and systems tend to be correspondingly large. This naturally suggests, or in cases requires, the incorporation of electromagnetic response into structurally large systems. This, in turn, can place mechanical and other

environmental demands on the material, particularly where said material is designed to be inherently multifunctional. Areas where metamaterials might be used include EM windows, signature control, surface wave control in phased arrays, or in devices such as lenses, waveguides, beam manipulators, reflectors, antennas, gratings, or cloaks. While tremendous advancements have been made in our abilities to produce metamaterials exhibiting novel electromagnetic properties, little has yet been done to understand the material's suitability to an operational environment. Of critical importance is an understanding of the interplay between electromagnetic and mechanical phenomena.

Because metamaterial EM response is so strongly tied to geometry and locally enhanced fields [10], it implies metamaterials have the potential to exhibit environmental sensitivities beyond those observed in traditional approaches and materials. Understanding the interdependencies between mechanical and thermal loading, and the resultant changes in EM performance is crucial for transitioning this technology from laboratory novelty to operational capability. As described in Section 1.4, a number of efforts have illustrated, but not fully developed the physical mechanisms driving these linkages. This research seeks to describe metamaterial strain and temperature-dependence in a manner that enables engineers to accurately predict metamaterial behavior in an operational environment.

To illustrate the relevance of this research, consider the metamaterial lens depicted in Figure 2. The flat composite plate is able to focus microwaves through a radially varying index of refraction. As mechanical loads and/or changing temperatures are applied to the lens, the strains and/or shifts in material properties induce changes to the EM characteristics of the subwavelength inclusions/unit cells. Aggregating that effect

over the entirety of the lens affects a change in focal length and potentially induces significant aberrations in the image. An engineer would need to understand the lens' sensitivity to the operational environment in order to a) mitigate those effects, b) develop adequate compensation schemes, or c) possibly maximize that sensitivity for a given application.

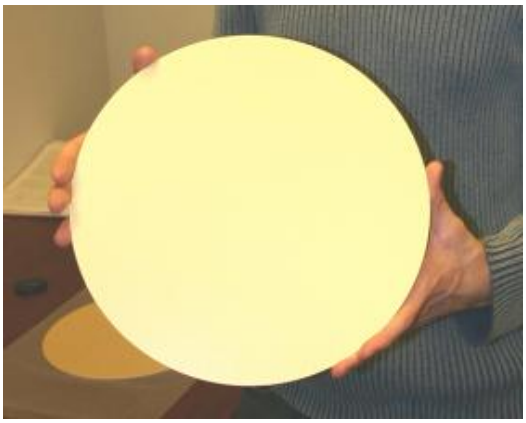

Figure 2. *Gradient index lens. The index of refraction is varied radially, enabling a flat plate to focus microwave frequencies. Additionally, the lens is impedance-matched to free space to minimize reflections [11].*

1.2. BACKGROUND ON ELECTROMAGENTIC METAMATERIALS

In 1996, Sir John Pendry and his colleagues demonstrated that an array of thin wires could produce a medium with an effective negative permittivity at GHz frequencies; analogous to the behavior of solid metals at ultraviolet (UV) frequencies [5]. In 1999, Sir Pendry presented the concept of artificial magnetic materials, where a composite structure, composed of non-magnetic parts, is able to exhibit a magnetic response [10]. Additionally, the paper presents the design and analytical expression for the Split Ring Resonator (SRR, an example is depicted in Figure 3) that enables the development of structures with a negative effective permeability (a phenomenon not known to occur in natural materials).

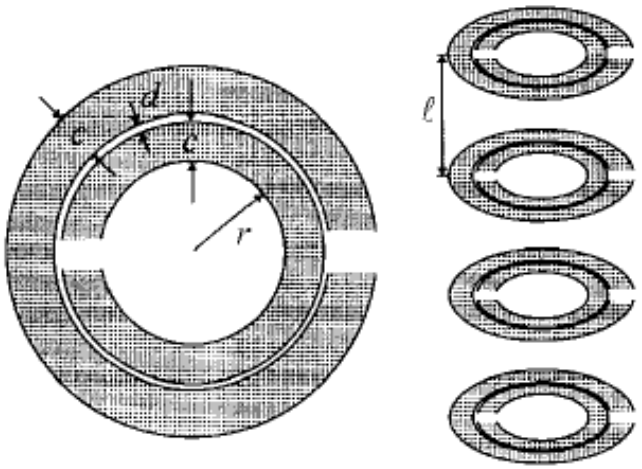

Figure 3. *Split-Ring Resonator (SRR) from [10]*.

In 2000, David Smith and his colleagues combined Pendry's negative permittivity and negative permeability structures to create a Negative-Index Material (NIM) [7][8]. Such materials exhibit the non-natural phenomenon of negative index of refraction; electromagnetic waves are refracted in the negative direction of the angle specified by Snell's law, and phase velocity is anti-parallel to the group velocity. This demonstration

of patently un-natural behavior suggested that metamaterials could greatly enhance our ability to control, and engineer, a structure's interaction with electromagnetic waves. Since these publications, the field of metamaterials has boomed, with developments covering such wide ranging topics as perfect lenses [12], cloaks [13][14], gradient index lenses [11], waveguide filters [15], perfect absorbers [16], and imaging beyond the diffraction limit [17]. As exemplified in [13][14][11], metamaterials enable the designer to develop intricate anisotropic and non-homogenous structures, further expanding our ability to manipulate interactions with electromagnetic waves. To enhance the design process, the concept of Transformation Optics [18] was produced. Transformation Optics allows the designer to determine how the permittivity and permeability tensors can vary, throughout a structure, in order to produce the desired propagation of EM within the medium.

As depicted in Figure 4, normal materials provide a limited range of electromagnetic properties. Furthermore, most materials are non-magnetic ($\mu=1$), so they elicit no response when subjected to a magnetic field. Therefore, the vast majority of materials fall along a single vector in the ε-μ design space, severely limiting the designer's ability to control interactions with EM waves. However, metamaterials have the potential to dramatically broaden that trade space, by enabling the design of materials with a wide range of ε and μ values.

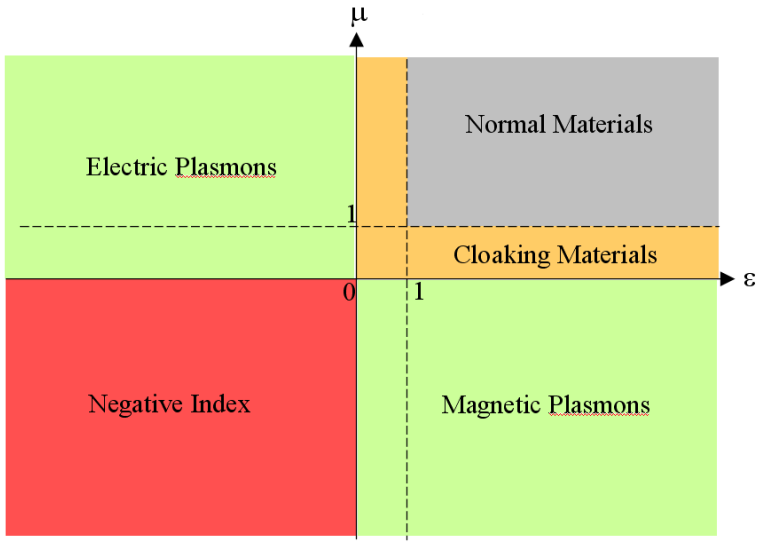

Figure 4: *Metamaterials open up a much broader design space, in terms of controlling the propagation of electromagnetic waves.*

While tremendous advancements have been made in our abilities to produce novel electromagnetic properties (some examples are presented in Figure 5), little has been done to understand the material's suitability in an operational environment. Of critical importance is an understanding of the interplay between electromagnetic and mechanical phenomena.

A significant benefit of metamaterials is that the numerous, sub-wavelength inclusions result in effective medium behaviors that can equivalently be described as piecewise continuous constitutive parameters; i.e. permittivity and permeability [19]. This ability to model the EM properties of the metamaterial as a continuous medium enables straightforward coupling with similar models utilized for assessing mechanical behavior.

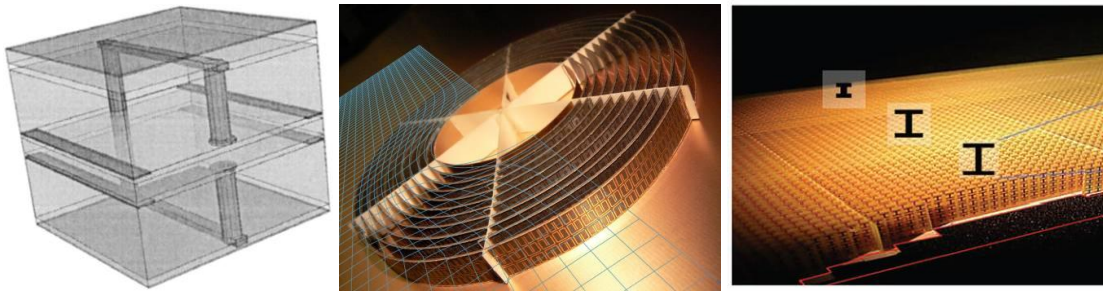

Figure 5. *At left, depiction of a metametarial unit cell used in the gradient index lens shown in Figure 2; typical metamaterial samples contain many thousands of cells. Central picture; hardware from Duke University's successful 2-D cloaking experiment, where the central section was virtually invisible at the frequency of interest [13]. At right, Duke's broadband ground-plane cloak which operated over a wide range of frequencies and incidence angles [14].*

1.3 ELECTROMAGNETIC WAVE PROPAGATION THROUGH A MEDIUM

Before talking about the specifics of this research effort, it is pertinent to briefly cover the physics of electromagnetic wave propagation through a medium. The following four equations are the differential form of Maxwell's equations for propagation in matter [20][21]

$$\vec{\nabla} \cdot \vec{D} = \rho_f$$

$$\vec{\nabla} \times \vec{E} = -\frac{\partial \vec{B}}{\partial t} \qquad \{0\}$$

$$\vec{\nabla} \cdot \vec{B} = 0$$

$$\vec{\nabla} \times \vec{H} = \vec{J}_f + \frac{\partial \vec{D}}{\partial t}$$

Where the arrow indicates a vector quantity, ρ_f is the free charge density, and $\vec{J}_f$ is the free electrical current.

Additionally, the constitutive parameters for linear, isotropic media provide the following relationships

$$\vec{D} = \boldsymbol{\varepsilon}\vec{E} \qquad \{1\}$$

$$\vec{H} = \frac{1}{\boldsymbol{\mu}}\vec{B}$$

It is important to note that the permeability and permittivity of a material can be anisotropic; thus, they are more accurately defined as a tensor of rank 2 (as opposed to the scalar values detailed for typical/isotropic materials). Additionally, the flexibility of metamaterials allows the designer to develop materials that enable direct coupling between the electric and magnetic field [22][23][24][25][26]; referred to as bi-anisotropy

or magneto-electric coupling. Thus, a more appropriate constitutive relationship for a generic metamaterial is captured via the following equation, which describes a fully bi-anisotropic material

$$\begin{pmatrix} \vec{D} \\ \vec{B} \end{pmatrix} = \begin{pmatrix} \boldsymbol{\varepsilon} & \boldsymbol{\xi} \\ \boldsymbol{\zeta} & \boldsymbol{\mu} \end{pmatrix} \begin{pmatrix} \vec{E} \\ \vec{H} \end{pmatrix} \quad \{2\}$$

Where the arrow again indicates a 1st order tensor (vector field), and bold font indicates a 2nd order tensor. **ε** and **μ** are the permittivity and permeability tensors of the material, respectively, and ξ and ζ are the coupling tensors.

This shows that a fully bi-anisotropic material may require the definition of up to 36 material parameters in order to model the propagation of electromagnetic waves. As in mechanical systems, certain laws of physics and symmetries in the material system can be used to eliminate and/or develop dependencies between the terms [27]; thus, reducing the number of independent terms which must be solved. This will be demonstrated in Section 2.1.

Understanding how these material parameters vary throughout the region of interest allows relatively simple and efficient solutions to the propagation of electromagnetic waves through complex media. The difficulties lie in a) developing materials with the correct material parameters, and b) retrieving all of parameters necessary to perform accurate electromagnetic simulations involving arbitrary polarizations and angles of incidence. Additionally, because the EM properties are so strongly tied to geometry and locally enhanced electric and/or magnetic fields**, the fundamental hypothesis of this research is that these parameters (ε, μ, ξ, and ζ) are functions of temperature and strain (T, E).**

1.4 LITERATURE SEARCH

A limited number of efforts have investigated the strain- [28][29][30] and temperature-dependence [31][32][33][34][35] of electromagnetic metamaterials. Melik, et al. proposed to use metamaterials as wireless strain sensors [28][29]. In laboratory tests, the authors tracked resonant frequency as a function of applied load, demonstrating linear sensitivity over an extended range. However, neither paper properly conveyed the full strain profile acting on the metamaterial unit cell (shown in Figure 6); both papers described strain as a scalar quantity, as opposed to defining the individual components of the strain-tensor. As detailed in Section 2.2, an infinite combination of strain components can result in the same shift in resonant frequency; thus, the resonant shift, taken alone, cannot uniquely describe the strain field present on the structure. The test results also demonstrated appreciable loss of Quality-factor (Q) with load, likely due to a non-uniform strain profile (as detailed in Section 2.4) and the resultant spreading of the metamaterial's EM response. Pryce, et al. placed gold metamaterial traces on a Polydimethylsiloxane (PDMS) substrate [30]. The frequency response of the samples demonstrated significant sensitivity to strain and the authors utilized equivalent circuit parameters to qualitatively describe the observed strain-dependence. Unfortunately, the authors incorrectly attributed the observed hysteresis to plasticity in the PDMS. Given the geometry, and the direction of loading, plastic deformation in the gold would increase the conductive path length, inducing a reduction in the gap between conducting elements. As detailed in Section 2.2, this results in an increase in both the metamaterial's inductance and capacitance, leading to the observed permanent red-shift in the resonant frequency. Plasticity in the PDMS, however, would cause a permanent increase in the

gap between conductive elements, as well as compressive loads on the conductive traces, thereby reducing the overall capacitance and inductance. Thus, plasticity in the PDMS would serve to increase the metamaterial's resonance (which was not the observed effect). While these efforts empirically demonstrated metamaterial strain-dependence, they illustrate a fundamental misunderstanding of the complexity of mechanical phenomena and their role in metamaterial strain-dependent EM response.

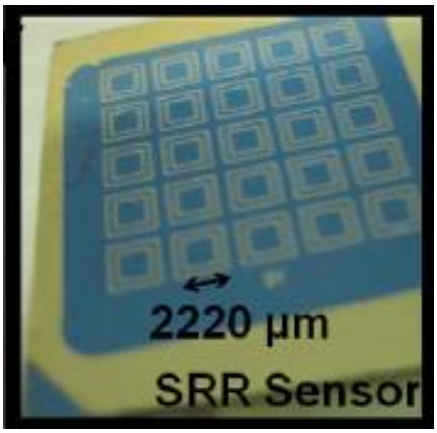

Figure 6. *SRR from [28]*.

Alici and Ozbay demonstrated the temperature dependent behavior of a magnetic ring resonator [31]. The authors utilized equivalent circuit parameters to describe the increase in the metamaterial's resonant strength at lower temperatures. Varadan and Ji demonstrated the temperature-dependence of SRRs in a laboratory environment [32]. The authors attributed the temperature-dependence to three causes; temperature-dependent permittivity of the substrate, temperature-dependent conductivity in metallic conductive traces, and thermally-driven strain. Equivalent circuit parameters were utilized to describe the change in the metamaterial's resonance. Aside from the research captured in this dissertation, Varadan and Ji's work provides the most significant description of, and insight into, metamaterial sensitivity to mechanical and/or thermal loading.

The efforts detailed in [33][34][35] also investigated temperature-dependence in metamaterial samples. However, the configurations for these samples are not generally traceable to designs that operate at radio frequencies. These papers also did not provide significant insight into the mechanics driving the metamaterial temperature-dependence, thus providing limited applicability to other metamaterial designs.

All of the studies detailed previously describe the behavior of magnetic (μ-only) metamaterials (designed to interact with the magnetic field of the EM wave). However, many metamaterials are ε-only (designed to interact with the electric field of the EM wave), or require both electric and magnetic contributions. Additionally, with the exception of [32], the studies did not present sufficient insight into metamaterial strain- and/or temperature-dependence such that the knowledge could be applied to other metamaterial designs and/or loading scenarios.

1.5 RESEARCH OBJECTIVES

This research seeks to quantitatively describe how electrical (ε-only) metamaterials behave when subjected to temperature changes and mechanical loading. Equivalent circuit models, and circuit parameters, are utilized to analytically describe metamaterial EM performance as a function of strain and temperature.

While standard numerical techniques can be used to model metamaterial strain- and temperature-dependence, analytic expressions provide a number of unique benefits:

1. Analytic expressions can be leveraged to *rapidly* predict the unique strain- and temperature-dependent constitutive properties of a wide range of unit cell designs that share a common equivalent circuit model.
2. Analytic expressions describe the behavior over the continuum of strains and temperatures of interest, whereas numerical techniques provide discrete sets of results for the conditions explicitly modeled.
3. Analytic expressions for metamaterial constitutive properties enable the use of continuum approaches for EM modeling. The use of continuum approaches, as opposed to directly solving interactions with a metamaterial's complex geometry, reduces model size by at least five orders of magnitude.
4. As a result, the use of analytic expressions are crucial for the efficient determination of the EM performance of large structures, with multiple unit cell designs, subjected to complicated strain and temperature profiles.

Additionally, the use of analytic expressions provides the design engineer with significant insight into the physics behind metamaterial strain- and temperature-dependence. The same level of understanding is not provided when conducting numerical analyses.

The ultimate goal of this research is to develop a process that enables engineers to quickly produce analytic expressions for the strain- and temperature-dependent permittivity (ε) and permeability (μ) for a family of metamaterial elements (family is meant to convey a set of elements with the same equivalent circuit model, but with different material properties and/or dimensions). In this way, if the strain field and temperature profile for a complex structure are known, the curves for the permittivity and permeability can be quickly generated over the entirety of the loaded structure, leading to rapid and accurate electromagnetic modeling of dynamic, time-variant problems. This understanding will also allow engineers to more competently mitigate, or possibly enhance, a metamaterial's strain- and/or temperature-sensitivities, dependent upon the requirements of the system.

2 METAMATERIAL STRAIN-DEPENDENCE

2.1 UNIT CELL DESIGN

The metamaterial unit cell design that forms the basis of this research is shown in Figure 7. The electric-inductor-capacitor (ELC) resonator is a design commonly used in metamaterials to provide a tailored electric response to electromagnetic waves [36]. Designed by SensorMetrix [37], this ELC operates at X-band, and utilizes two parallel capacitors for enhanced resonant response. It is produced by electrode depositing 1-oz copper (34 μm) on a 1/16th inch thick sheet of Rogers' RT/Duroid-5880 [38].

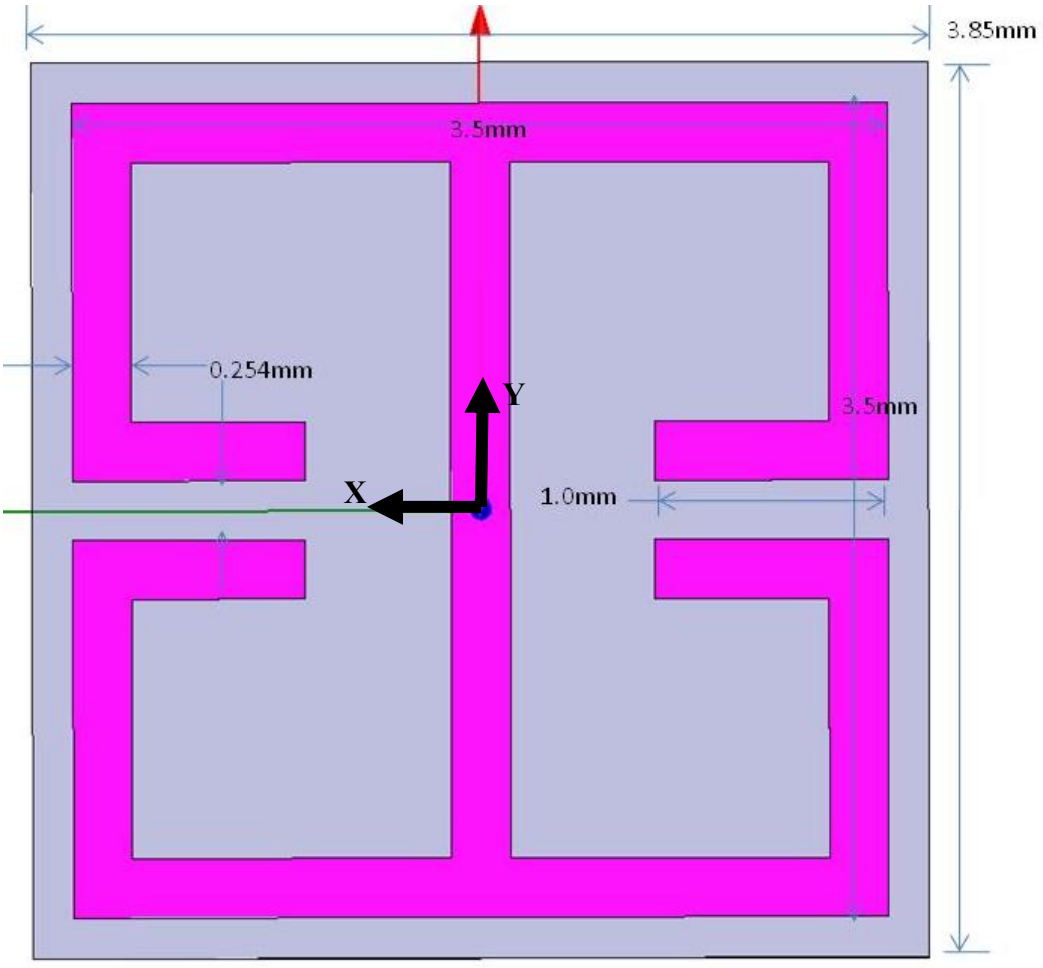

Figure 7. *ELC unit cell with pertinent dimensions. Also shown is the reference coordinate frame that will be used throughout the remainder of this research.*

Figure 8 shows the scattering (S) parameters and phase for one unit cell of the medium, utilizing standard numerical techniques [39]. Only S11 and S21 are shown, because this unit cell is reciprocal (i.e. the performance is the same for waves propagating in the +Z and –Z direction), so S11=S22 and S21=S12 [40]. As the figure shows, the cell is designed to resonate at 9.33 GHz, with a Quality Factor (Q) of ~200.

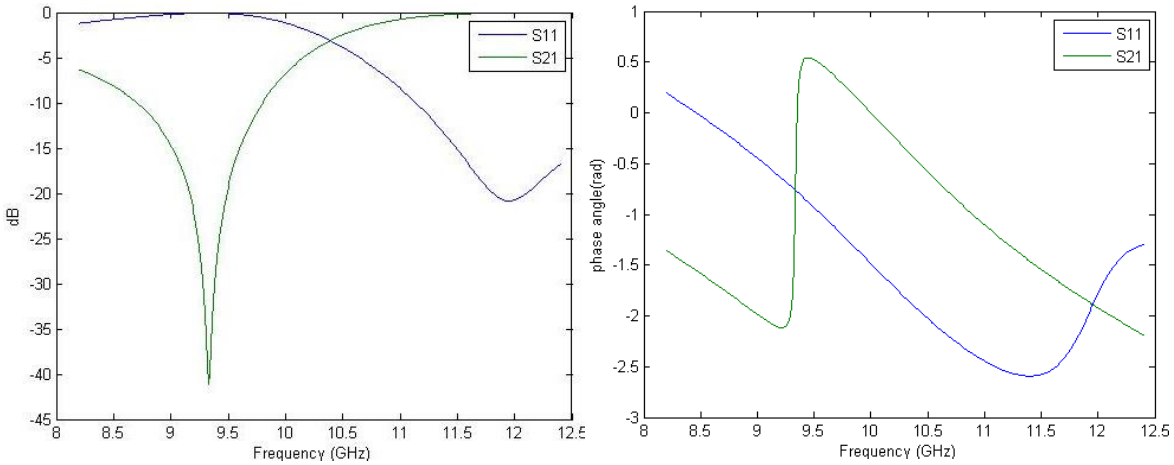

Figure 8. *Numerically generated S-parameter curves and phase diagram for the baseline/unstrained unit cell, illustrating a resonance at 9.33 GHz.*

An important design feature is that this cell is designed to operate at a single polarization; specifically, it is designed to interact with the vector component of the electric field oriented in the Y-direction (refer to Figure 7) of an electromagnetic wave propagating normal to the surface of the cell. The research detailed in this document will restrict the analysis to this designed orientation (normal incidence, Y-polarized).

Another feature that plays a role in this research is the flexibility provided by this unit cell design. Metamaterial designers often take a unit cell that operates close to the frequency of interest and alter the length of the capacitor pads (1mm in Figure 7), the separation between capacitor pads (0.254 mm in Figure 7), and/or the dielectric constant of the substrate to tune the metamaterial to provide an optimized response for a particular

requirement. It is therefore an underlying goal of this research to enable the efficient determination of strain- and temperature-dependence for a family of unit cells, as opposed to a single point design.

As mentioned previously, the most general form of the constitutive relationship for electromagnetic materials is captured in Eq. {2} (re-copied for clarity). Understanding the material properties that relate $\vec{D}$ and $\vec{B}$ to $\vec{E}$ and $\vec{H}$ allow efficient modeling of the propagation of electromagnetic waves through complex media.

$$\begin{pmatrix} \vec{D} \\ \vec{B} \end{pmatrix} = \begin{pmatrix} \boldsymbol{\varepsilon} & \boldsymbol{\xi} \\ \boldsymbol{\zeta} & \boldsymbol{\mu} \end{pmatrix} \begin{pmatrix} \vec{E} \\ \vec{H} \end{pmatrix} \quad \{2\}$$

Even restricting the analysis to normal incidence and a single polarization (electric field aligned with the Y-axis) requires the definition of up to twelve distinct material properties in order to solve Maxwell's equations. However, the symmetries present in this study allow one to quickly eliminate terms from consideration.

The first symmetry is due to the fact that the material is reciprocal; the behavior is the same for propagation in the positive and negative Z-direction. The second is due to the assumption that the gradients in mechanical loading and temperature operate over length scales much larger than the unit cell. This ensures that the loads being applied through the boundaries are symmetric. Coupled with the inherent symmetry of the unit cell, these symmetries dictate that the loaded unit cell displays point of inversion symmetry, even for the complex strain profiles encountered with low stiffness substrates (presented in Section 2.4). As presented in [41][42], inversion symmetry explicitly requires an absence of bi-anisotropy; therefore, $\boldsymbol{\zeta}$ and $\boldsymbol{\xi}$ are identically equal to zero.

It is also reasonable to assume a lack of out-of-plane rotations of the electromagnetic wave, since the metamaterial sample, as well as all of the layers that comprise the composite structure, are normal to the direction of the propagation. Additionally, numerical analyses showed that the rotated electromagnetic fields induced via cross-polarization (off-diagonal) terms are insignificant when compared to the fields aligned with the primary polarization. Therefore, the material properties of interest for this effort are ε_{YY} and μ_{XX}.

2.2 ANALYTICALLY DESCRIBING A METAMATERIAL'S STRAIN-DEPENDENT RESONANT FREQUENCY

As shown in Section 2.1 and Figure 8, the resonant frequency is often a critical design feature for a metamaterial structure; resonance is often necessary for achieving the unique EM properties enabled by metamaterials [5][6][7][8][10][11][12]. Standard electrical engineering practices [20][21] and investigations into metamaterial behavior [28][29][30][31][32][43] frequently utilize lumped circuit elements (in this case, inductors and capacitors) to analytically describe a structure's resonant frequency. As a result, initial attempts to analytically describe metamaterial strain-dependent behavior focused on predicting the shift in resonance with applied strain.

2.2.1. Introduction

A significant amount of interest lies in integrating metamaterial functionality into load-bearing structures [11][44][45][46]. These interests are utilized to formulate some of the underlying assumptions for the subsequent analyses:

a) As mentioned in Section 1.1, many systems operating at X-band frequencies are structurally large. As a result, each metamaterial unit cell can be modeled as a nearly infinitesimal part of a much larger structure; it also enables the complex unit cell to be equivalently modeled as a homogenous slab with effective constitutive parameters [22][47]. Therefore, neglecting the strong gradients that occur at locations of structural attachment, it is assumed that the load profile for the preponderance of the metamaterial surface is homogeneous and symmetric at the unit cell level; i.e. that the gradients of

stress and temperature operate over scales much larger than the dimensions of the unit cell.

b) The subwavelength inclusions of the metamaterial do not contribute significantly to the stiffness of the composite structure. Load-bearing implies that the structure is produced from high modulus materials, and has sufficient thickness to resist bending loads. As a result, the copper is assumed to move uniformly with the underlying substrate; i.e. perfect strain transfer into the copper, and negligible local stiffening effects. Section 2.4 will detail how metamaterial strain-dependence is affected when this assumption is removed.

c) The analysis assumes linear-elastic behavior in the constituent materials, in order to produce processes and trends that are general and easily transitioned to other designs and material choices. The onset and growth of plastic deformation is path-dependent and necessarily implies a loss of generality. While the strain levels used in this study routinely exceed the elastic limit of the materials implemented in the model, the extended range of strains engendered high confidence in the form of the relationships between strain, temperature, and EM performance. For the metamaterial designer, material choice, and their inherent elastic limits, will serve to dictate which portions of the curves/trends are applicable for their particular design. This analysis also neglects the onset of buckling, and other mechanical phenomena that are structure-dependent.

2.2.2 Numerical Modeling

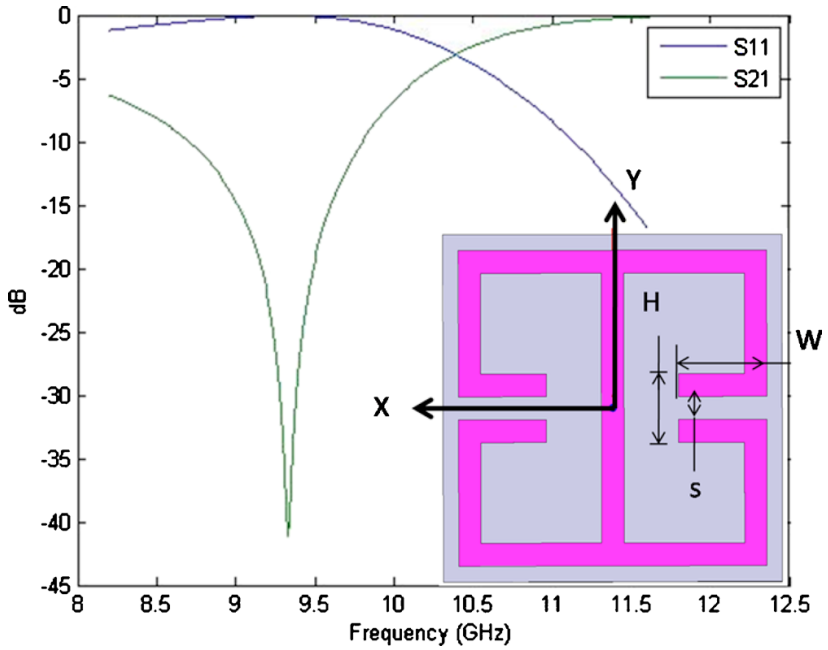

Figure 9. *Unit cell and baseline/unloaded S-Parameter data [50].*

As a result of these assumptions, the strain profile is approximately uniform across the unit cell depicted in Figure 9. Due to the uniformity in the strain profile, and the resultant absence of higher order terms, a linear system can be utilized to describe the deformed geometry of the unit cell, taking the form [48]:

$$\begin{Bmatrix} X^1 \\ Y^1 \\ Z^1 \end{Bmatrix} = \begin{bmatrix} E_{XX} & E_{XY} & E_{XZ} \\ E_{XY} & E_{YY} & E_{YZ} \\ E_{XZ} & E_{YZ} & E_{ZZ} \end{bmatrix} \begin{Bmatrix} X^0 \\ Y^0 \\ Z^0 \end{Bmatrix} + \begin{Bmatrix} X^0 \\ Y^0 \\ Z^0 \end{Bmatrix} \quad \{3\}$$

The superscript 0 and 1 refer to the undeformed and deformed geometries, respectively, and the 3x3 matrix is the mechanical strain tensor. The model accommodates different values of E_{zz} in the substrate and copper, due to the differing mechanical properties in the materials. As significant out-of-plane bending is not expected, the analysis is restricted to in-plane loads. This assumption is further supported in prior analysis and experiments on curved, transformation optical metamaterials (Figure 10), where changes in the

electromagnetic performance of metamaterial structures, due to curvature in the unit cell, were shown to be negligible [13][49]. Therefore, the terms E_{XZ} and E_{YZ} are set equal to zero.

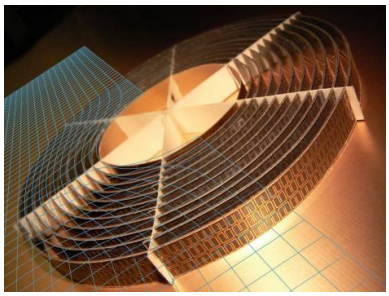

Figure 10. *Microwave cloak from [13]*

The unit cell was modeled in ANSYS-HFSS [39], utilizing equation surfaces that integrate the strain tensor transformation, Eq. {3}, into the surface descriptions. Thus, the model accommodates geometry changes resulting from any arbitrary in-plane loading scenario. To determine the impact of various strain states on the electromagnetic scattering properties (S-parameters), parametric sweeps were run in which the global variables E_{XX}, E_{XY}, E_{YY}, E_{ZZS}, and E_{ZZC} were varied; where S and C in the subscript refer to the substrate and copper, respectively. Each strain component was stepped over the range -5% and +5% with the S-parameters computed at each step. The influence of each strain component was evaluated separately.

Although the form of the strain-dependence was not known a-priori (power, logarithmic, linear, etc.), it was assumed that the trend should be consistent over the tested range; e.g. monotonically increasing the strain value consistently decreases the resonant frequency. When the parametric analysis did not produce a consistent trend, the convergence criteria was tightened and the analysis re-run. The modeling results were considered accurate when tightening the convergence criteria resulted in identical curves

for the resonant frequency as a function of strain. This process was chosen, because a significant problem with the modeling task was that the errors were deterministic; if a particular set-up returned an incorrect solution, re-initializing the model, and then re-accomplishing the analysis simply returned the same incorrect solution.

The process utilized by HFSS to produce the S-parameter curves (S11, S21, S12, S22) was to first determine the S-parameters at the user defined solution frequency. It then refined the mesh and re-solved the problem until the difference between sequential solutions (referred to as the "delta-S") fell below the convergence criteria. The solver then used that same mesh to solve over the entire frequency range of interest (known as a "Fast Sweep"). The software then incremented to the next strain value and repeated the process.

A significant amount of effort was required to force the software to refine the mesh sufficiently, such that it delivered a consistent trend over the entire range of strain values. A satisfactory trade between speed and accuracy was found by using the higher of the frequencies at which S21=S11 (10.3 GHz for this cell) as the solution frequency, setting a very tight tolerance (delta-S = 0.0025, or -52.04 dB), and requiring two consecutive passes within that tolerance. Speed was increased significantly by allowing the software to utilize curvilinear and mixed mode elements (allows solution within each element to be either scalar, linear, quadratic, etc.).

Even after significant optimization, the software still required approximately 24 hrs to solve 40 permutations of strain. The computer used for the simulation was a Dell Precision T7500, with 25GB of memory and eight parallel processors, running at near

100%. Each successfully converged solution required between 200,000 to 300,000 tetrahedra.

The solutions from the simulation demonstrated that out-of-plane normal strains (affecting the thickness of the copper and substrate) produce a negligible effect on the electromagnetic scattering. However, the in-plane strains (E_{XX}, E_{XY}, and E_{YY}) produce a measurable effect, as depicted in Figure 11.

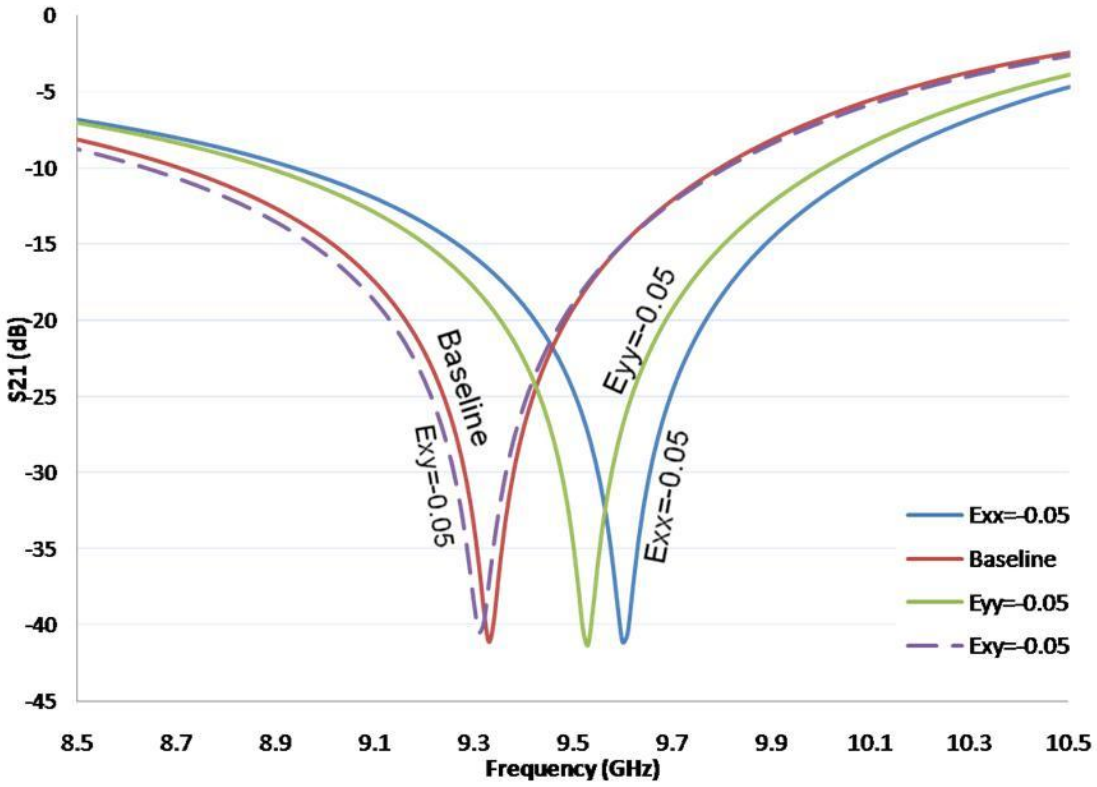

Figure 11. *Transmission (S21) of the metamaterial with different strain inputs. Baseline implies no applied strain [50].*

2.2.3 Analytic Description

To better understand the mechanisms associated with the strain-dependent scattering, analytic expressions for the equivalent circuit parameters of the ELC medium were applied. The capacitance (C) for a co-planar capacitor can be approximated as [51]

$$C = C_a + C_s$$
$$C_a = \varepsilon_0 \frac{2}{\pi} \ln\left(2\beta \frac{H}{s}\right) W \qquad \{4\}$$
$$C_s = \varepsilon_0 \frac{\varepsilon_s - 1}{\frac{s}{h_s} + \frac{4}{\pi} \ln \beta} W$$

Where *W, s,* and *H* are the geometrical parameters of the ELC, as depicted in Figure 9. The subscripts *a* and *s* refer to air/vacuum and substrate, respectively, and β=5/2. The self-inductance (L) of a thin, conducting strip can be approximated as [52]

$$L = \frac{\mu_0 l}{2\pi}\left[\ln\left(\frac{2l}{b}\right) + \frac{1}{2} + \frac{b}{3l} - \frac{b^2}{24l^2}\right] \qquad \{5\}$$

Where *l* is length and *b* is width of the conducting strip. Loop inductance can be neglected, due to the symmetry of the unit cell [53]. The total effective inductance and capacitance for the unit cell (accounting for the addition of parallel and/or series capacitors and inductors, as well as inter- and intra-cell capacitances) were computed, and used to determine the element's resonant frequency as a function of strain. The resonant frequency of the strained unit cell can be written relative to the unstrained resonant frequency as [21]

$$\omega_0' = \frac{1}{\sqrt{L'C'}} = \frac{1}{\sqrt{L\frac{L'}{L}C\frac{C'}{C}}} = \omega_0 \sqrt{\frac{L}{L'}\frac{C}{C'}} \qquad \{6\}$$

Where the primes correspond to the strained unit cell and unprimed corresponds to the baseline/unstrained cell. Eqs. {4-6} allow predictions of the shift in the resonant frequency that are in quantitative agreement with the full-wave simulations. Figure 12 depicts the resonant frequency as a function of the applied, in-plane normal strain, comparing the analytic predictions to the solutions of the full-wave simulation. As

Figure 12 shows, the analytic predictions and the simulation results for E_{XX} and E_{YY} are in strong agreement.

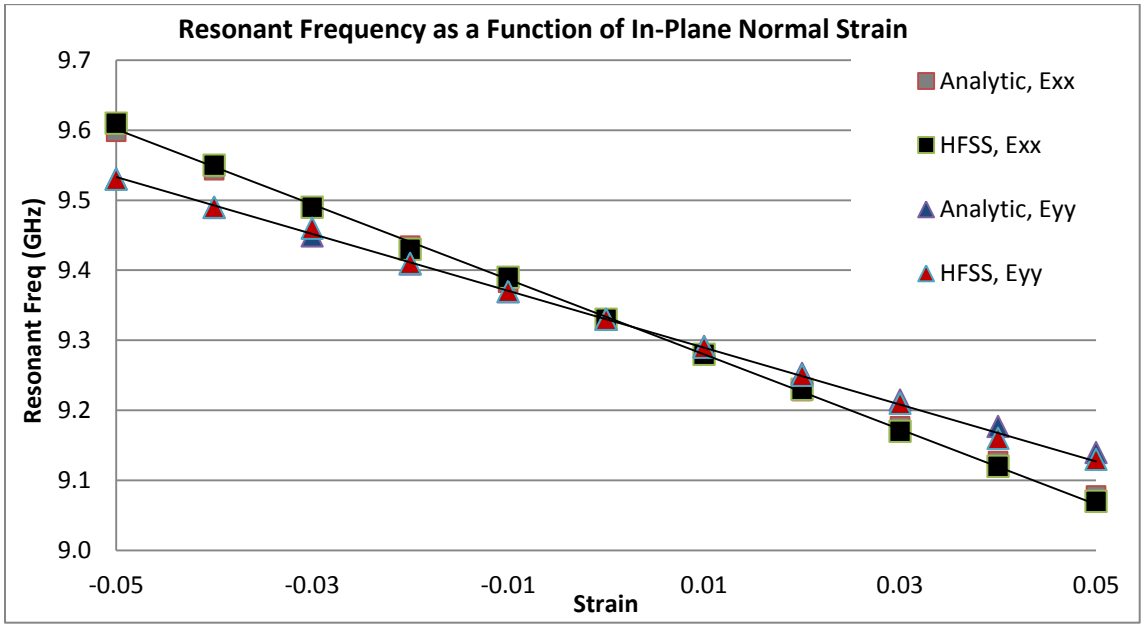

Figure 12. *Resonant frequency as a function of in-plane normal strains*

Referring to Figure 9, one can qualitatively observe that a tensile strain (extension) in the X-direction causes an increase in both the ELC element's self-inductance (increases l in Eq. {5}) and capacitance (increases W in Eqs. {4}), resulting in a decrease in the resonant frequency. A compressive strain causes the opposite effect. Conversely, a tensile strain in the Y-direction causes an increase in the ELC element's inductance (again by increasing l in Eq. {5}), while decreasing the cell's capacitance (increasing s in Eqs. {4}). While the two influences are in opposition, the inductance change dominates, resulting in a net decrease in the resonant frequency. A shear strain (irrespective of sign) causes a small increase in the ELC element's inductance (increases l) as well as a slight increase in the cell's capacitance (decreases s), resulting in a slight drop in the resonant frequency.

While the trends in Figure 12 are not strictly linear (according to Eqs. {4-6}), they can be approximated by linear trends for the range of deformations pertinent to most mechanical systems. The apparent linearity of the trends allows the resultant resonant frequency—for a metamaterial surface subjected to any complex in-plane loading scenario (components of E_{XX}, E_{XY}, and E_{YY})—to be accurately predicted via superposition of the influence from each of the individual strain components. Thus, the strain-dependent resonant frequency for this particular unit cell is described by the equation $f_0(GHz) = 9.33 - 5.35E_{XX} - 4.06E_{YY} - 0.4|E_{XY}|$.

2.2.4 Conclusion

The resonance is a critical parameter in many metamaterial designs and provides a critical data point for describing and understanding the structure's effective medium properties. Analytically describing the strain-dependence of the resonant frequency provides significant insight into a metamaterial's behavior when mechanically loaded. However, as detailed in Section 1.3, efficient modeling of metamaterial performance is enabled through the description of the EM constitutive parameters (ε and μ). The next section details efforts to analytically describe the strain-dependent permittivity and permeability of the metamaterial structure.

2.3 EQUIVALENT CIRCUIT ANALYSIS OF METAMATERIAL STRAIN-DEPENDENT EFFECTIVE MEDIUM PARAMETERS

As detailed in Section 2.1, the metamaterial's effective permittivity (ε_{YY}) and permeability (μ_{XX}) are the key constitutive material properties required to efficiently solve the propagation and interaction of EM waves. This section expands upon the analysis of Section 2.2 to analytically describe and predict how the permittivity and permeability change with applied strain.

2.3.1 Numerical Modeling and Parameter Retrieval

Utilizing the S-parameter results from the previous section (Figure 9 and Figure 11), effective medium parameters (ε, μ) were retrieved via the following standard inversion algorithm [40].

$$n = \frac{1}{kd}\cos^{-1}\left[\frac{1}{2S_{21}}\left(1 - S_{11}^2 + S_{21}^2\right)\right] \qquad \{7\}$$

$$z = \sqrt{\frac{\left(1+S_{11}\right)^2 - S_{21}^2}{\left(1-S_{11}\right)^2 - S_{21}^2}}$$

$$\varepsilon = n/z, \mu = nz$$

Where n is the index of refraction, z is the characteristic impedance, k is the wavenumber ($2\pi/\lambda$), and d is shown in Figure 13. Figure 14 shows values for the metamaterial's permittivity, permeability, characteristic impedance, and index of refraction.

Of note, even though the dimensions of the unit cell necessarily change with the applied strain, the lattice constant d was kept constant in the parameter retrieval process

for all configurations/strain states. Figure 15 shows the material's permittivity at several different strain conditions.

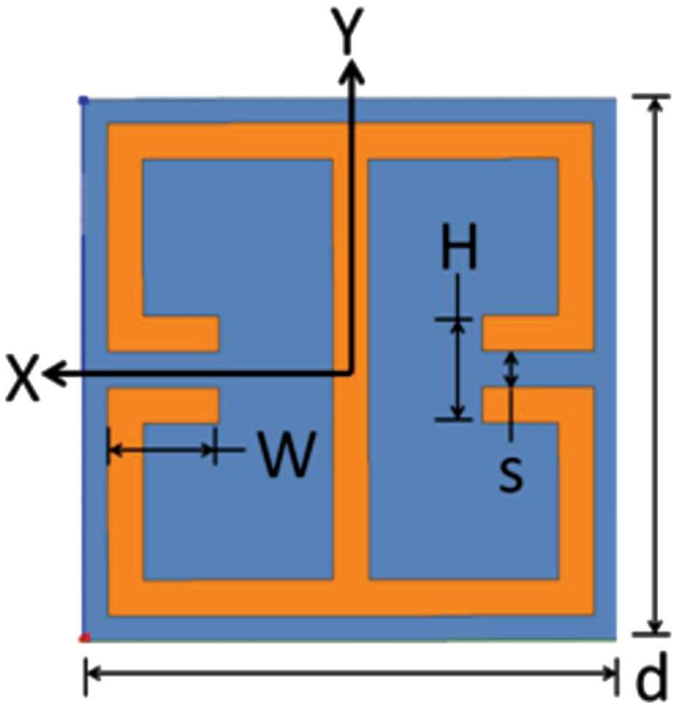

Figure 13. *Unit cell geometry.W=1mm, d=3.85mm, H=0.762mm, s=0.254mm [54].*

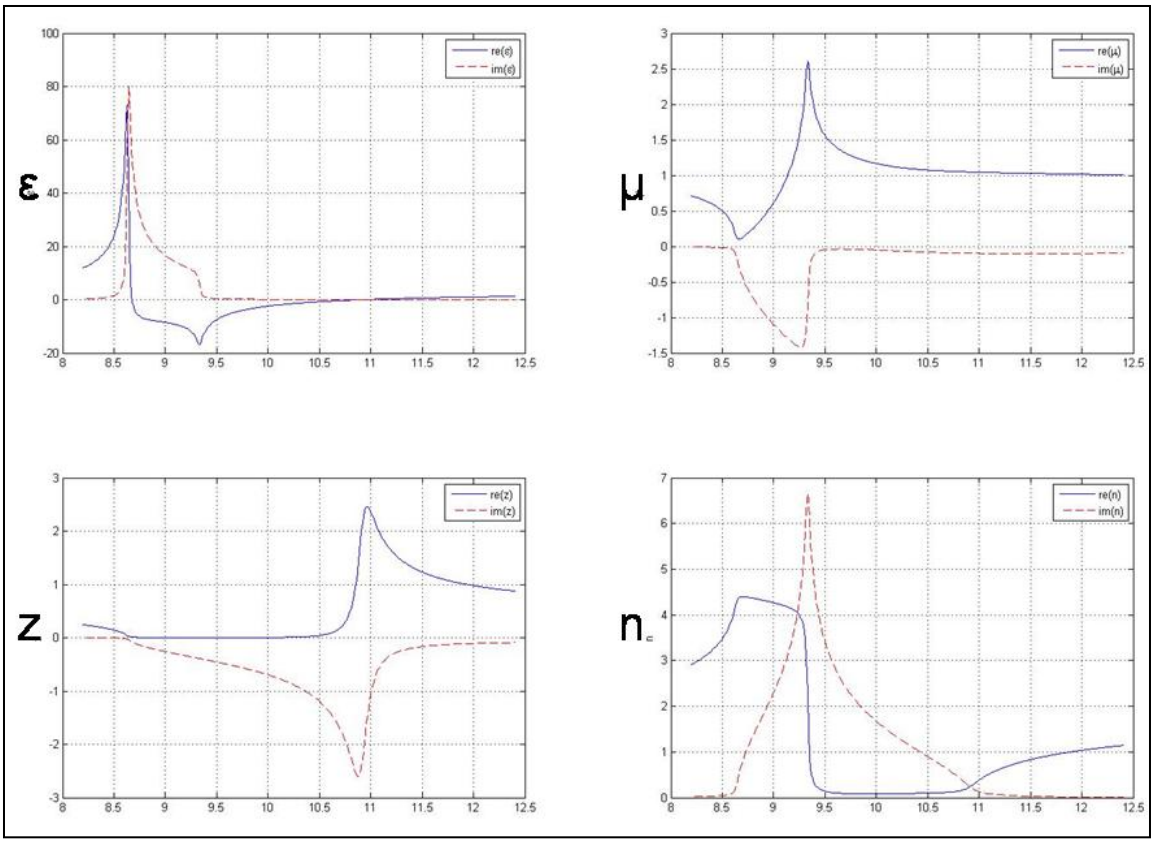

Figure 14. *Retrieved parameters for the baseline/unloaded unit cell, showing both the real (solid line) and imaginary (dashed line) components of the permittivity (ε), permeability (μ), wave impedence (z), and index of refraction (n). The X-axis is frequency (in GHz).*

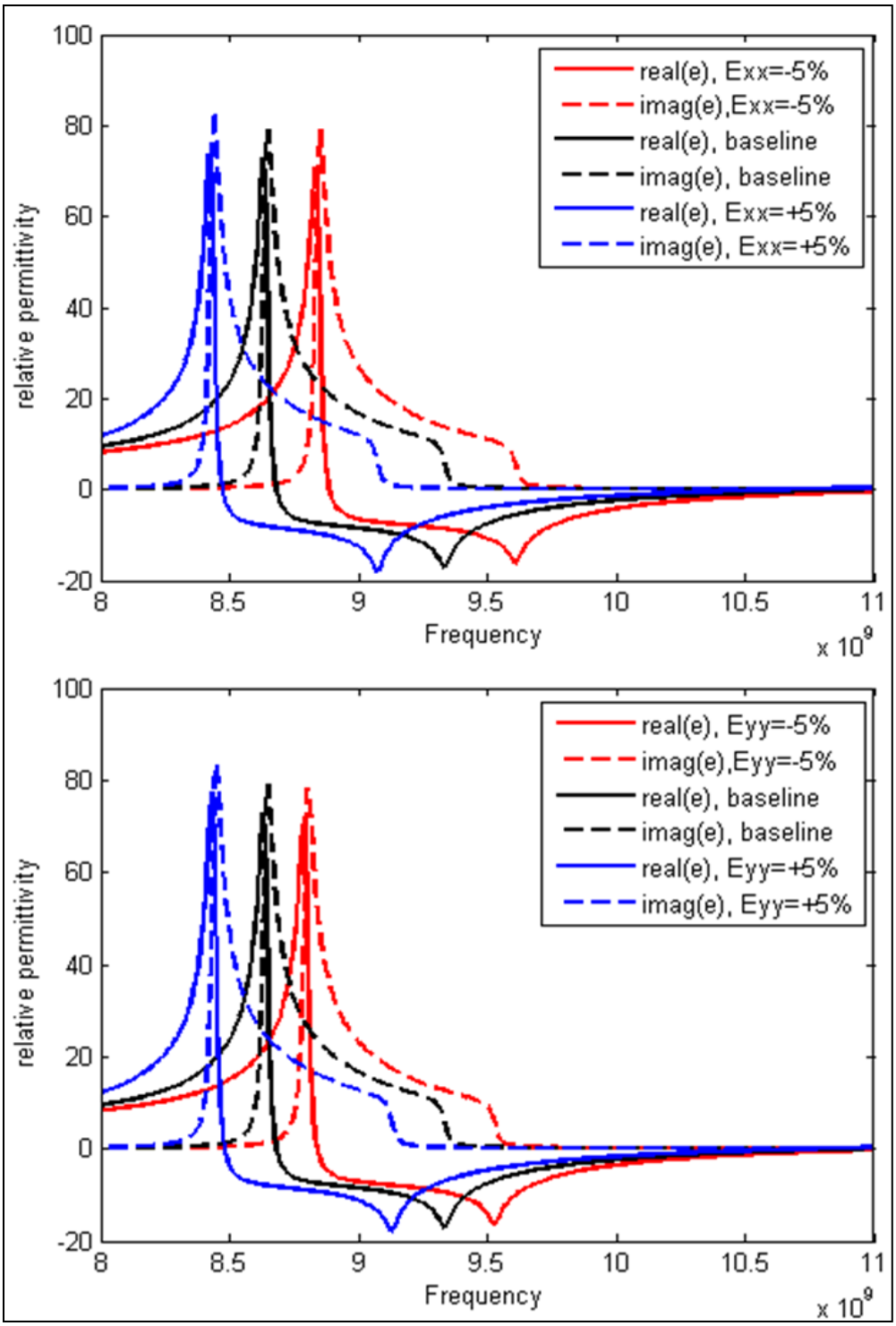

Figure 15. *Effective permittivity of the unit cell at different strain states (simulated in HFSS). The top chart shows the permittivity change with respect to normal strains in the X-direction (Exx), while the bottom chart shows the permittivity curves responding to a normal strain in the Y-direction (Eyy). As detailed in Section 2.2, the unit cell is more sensitive to Exx than Eyy [54].*

The permittivity and permeability for this electrically resonant (non-magnetic) metamaterial can be described analytically, via the following set of equations [22]

$$\varepsilon = \bar{\varepsilon}\frac{\frac{\theta d}{2}}{\sin\frac{\theta d}{2}\cos\frac{\theta d}{2}} \qquad \{8\}$$
$$\mu = \frac{\frac{\theta d}{2}}{\sin\frac{\theta d}{2}}\cos\frac{\theta d}{2}$$

Eqs. {8} represent an approximate analytical form for the effective medium parameters of a thin layer of electrically resonant polarizable elements embedded within a cubic cell of dimension *d*. The effective permittivity of the layer is assumed to have the Drude-Lorentz form given by

$$\bar{\varepsilon}(f) = \varepsilon_b - \frac{f_p^2}{f^2 - f_0^2 + i\Gamma_e f} \qquad \{9\}$$

Where f_p, f_0 and Γ_e are the plasma frequency, resonant frequency, and damping parameters of the ELC, respectively. These parameters are generally related to the geometry and equivalent circuit parameters associated with the element. The propagation constant, θ, has the form

$$\theta = n_{eff}\frac{\omega}{c}. \qquad \{10\}$$

The sine and cosine terms in Eq. {8} account for *spatial dispersion*—or the spatial inhomogeneity of the structure. While the ELC (as with other metamaterial structures) occupies a significant portion of the unit cell, the effective response can nevertheless be modeled as being situated in a small volume within that cell, with the

remainder being air (or whatever the host dielectric material is). The inhomogeneity introduces artifacts into the otherwise Lorentzian-like constitutive parameters that are well described by the additional terms in Eqs. {8}. In particular, utilizing the relationship for θ, it is possible to remove the effects of spatial dispersion from the simulated constitutive parameters, and finally extract values for the Lorentzian-like ELC oscillator ($\bar{\varepsilon}$, shown later in Figure 17). Standard curve fitting procedures (such as those available in MatLab's Curve Fitting Toolbox [55]) can then be applied to determine the values of ε_b, f_0, f_p, and Γ_e.

2.3.2 Description via Equivalent Circuit Parameters

While Eq. {9} has been previously applied to evaluate electric metamaterial structures, it does not quite represent a full description of the ELC and must be modified through the use of a more detailed circuit model, depicted schematically in Figure 16.

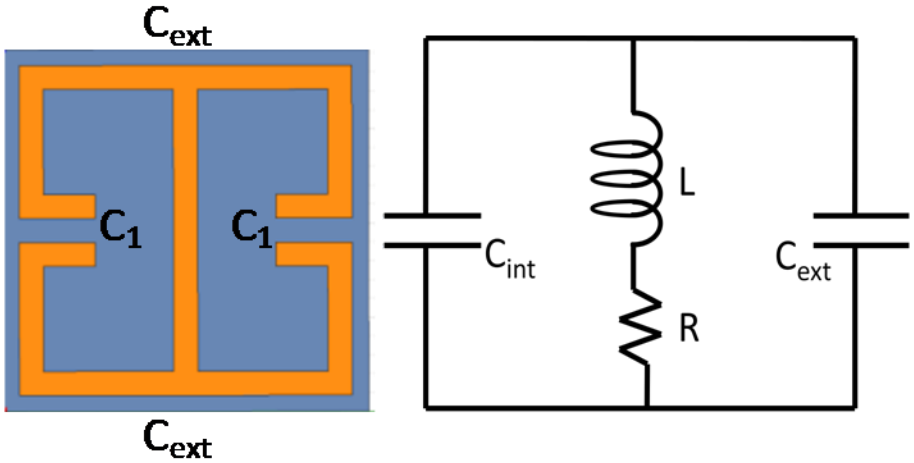

Figure 16. *Equivalent circuit model of the ELC metamaterial unit cell. For this design, $C_{int}=2C_1$ [54].*

To obtain the appropriate expression for the effective permittivity, one must first calculate the impedance for the circuit model shown in Figure 16, which consists of

external capacitances in series with a parallel LC circuit. The impedance of the structure can be written as $z_{tot} = z_{C_{ext}} + z_L \,||\, z_{C_{\text{int}}}$. Using $z_C = 1/(i\omega C)$ and $z_L = i\omega L$, results in

$$z_{tot} = \frac{1-\omega^2 L\left(C_{ext}+C_{int}\right)}{i\omega C_{ext}\left(1-\omega^2 L C_{int}\right)}. \qquad \{10\}$$

The expression for the impedance, Eq. {10}, can be utilized in conjunction with a transmission line formulation to arrive at an approximate expression for the effective permittivity of the ELC. In the limit that the free-space wavelength is much larger than the unit cell dimension, the transmission line model gives [56]

$$\bar{\varepsilon} = 1 + \frac{z_0}{i z_{tot} kd}. \qquad \{11\}$$

Inserting the impedance expression Eq. {10} into Eq. {11}, gives

$$\bar{\varepsilon} = 1 + \frac{C_{ext}}{d\varepsilon_0}\frac{\omega_0^2 - \omega^2}{\omega_0^2 - \omega^2\left(1+\dfrac{C_{ext}}{C_{int}}\right)}, \qquad \{12\}$$

where $\omega_0^2 = \dfrac{1}{LC_{int}}$. The effect of resistive losses can be incorporated into the model by assuming the resistive paths are identical to the inductive paths, and letting $L \to L + \dfrac{R}{i\omega}$.

Analogous to the process outlined in Section 2.2, Eqs. {4 and 5} are used to describe the equivalent circuit parameters required for Eq. {12}. Since these expressions reveal the explicit dependence of the circuit parameters on geometry, a complete analytical description of the strain-dependent permittivity and permeability is facilitated. The capacitance (C) for a co-planar capacitor can be approximated as [51]

$$C = C_a + C_s$$
$$C_a = \varepsilon_0 \frac{2}{\pi} \ln\left(2\beta \frac{H}{s}\right) W \qquad \{4\}$$
$$C_s = \varepsilon_0 \frac{\varepsilon_s - 1}{\frac{s}{h_s} + \frac{4}{\pi} \ln \beta} W$$

Where *W*, *s*, and *H* are the geometrical parameters of the ELC, as depicted in Figure 13. The subscripts *a* and *s* refer to air/vacuum and substrate, respectively, and β=5/2. The self-inductance (L) of a thin, conducting strip has the form [52]

$$L = \frac{\mu_0 l}{2\pi}\left[\ln\left(\frac{2l}{b}\right) + \frac{1}{2} + \frac{b}{3l} - \frac{b^2}{24l^2}\right] \qquad \{5\}$$

Where *l* is length and *b* is width of the conducting strip. The resistance of any length resistor can be simply approximated by

$$R = \frac{l}{\sigma A} \qquad \{13\}$$

where σ is the conductivity, and *l* and A the length and cross-sectional area of the conductor.

Inserting the analytic circuit parameter equations into Eq. {12} results in an expression for the effective permittivity that can be compared with that retrieved from a full wave simulation. First consider an unstrained unit cell to obtain a baseline response. While Eqs. {4, 5, and 13} are only approximate (the unit cell geometry lies outside some of the assumptions used for their derivation), they are nevertheless accurate enough to enable curve-fitting between the two functions. A good fit, utilizing MatLab's Curve Fitting Toolbox, was achieved using the following values: C_{int}=2.94x10^{-14} F, C_{ext}=4.84x10^{-14} F, *L*=3.74x10^{-9} H, and *R*=0.74 Ω (refer to Figure 16 for the circuit model

of the unit cell). Figure 17 shows the $\bar{\varepsilon}$ extracted from the simulation, compared to the analytic expression. For the resistance calculation, it is well known that the harmonic input causes the induced currents to reside on the surface of the conductor. Good agreement with the curve fit results was achieved by using 1 skin-depth at resonance $\left(\delta = \sqrt{2/\omega_0 \mu \sigma}\right)$ to calculate the cross-sectional area (A=$b\delta$) of the conductor in Eq. {13}.

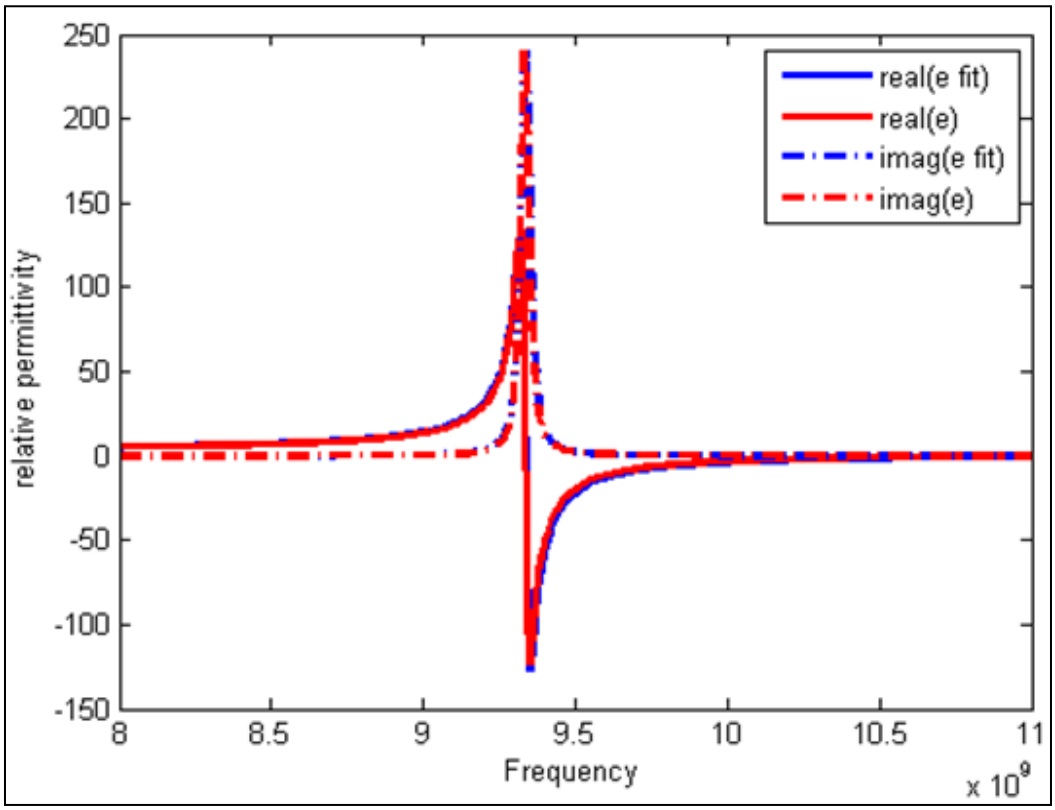

Figure 17. *Analytic (e fit) vs simulation-derived (e) Lorentzian-like ELC oscillator ($\bar{\varepsilon}$) used for curve-fitting purposes [54].*

A curve fit was also performed on the original form of $\bar{\varepsilon}$ to check the appropriateness of the values used for the circuit model. The following relationships demonstrate concurrence between the alternative forms of the analytic expression $(\bar{\varepsilon})$ [21]:

$$\Gamma_e = \frac{1}{2\pi}\frac{R}{L} = 31.5\ MHz$$
$$f_0 = \frac{1}{2\pi}\sqrt{\frac{1}{L\left(C_{int}+C_{ext}\right)}} = 9.33\ GHz \qquad \{14\}$$

With $\bar{\bar{\varepsilon}}$ successfully defined, the effects of spatial dispersion are then included via the relationship [22]:

$$sin\frac{\theta d}{2} = \sqrt{\bar{\bar{\varepsilon}}}\frac{kd}{2} \qquad \{15\}$$

This last piece of information is crucial, because it implies that full knowledge of $\bar{\bar{\varepsilon}}$ (Eq. {12}) allows *full* reconstruction of the permittivity *and* permeability curves. So understanding the strain-dependent behavior of the metamaterial is distilled to understanding the strain-dependent behavior of four critical parameters: C_{int}, C_{ext}, L, and R. Furthermore, each of these parameters is a readily described function of geometry. Thus, mechanical strain (a change in geometry) can be readily integrated into Eqs. {4, 5, and 13} to ascertain the strain-dependent electromagnetic behavior of the metamaterial.

With Eq. {12} defined, Eq. {15} is utilized to determine the phase advance across the unit cell, subsequently applying the determined values of $\bar{\bar{\varepsilon}}$ and θd to Eq. {8}. In this way, the full frequency dependent permittivity and permeability functions can be determined. Figure 18 shows the analytically-constructed permittivity compared to the permittivity retrieved from the full-wave simulation for the baseline/unstrained unit cell.

Equations {4, 5, and 13} are then used to describe the strain-dependence of C_{int}, C_{ext}, L, and R. These trends are linearized, with minor loss of accuracy, providing the following strain-dependent descriptions for the circuit elements of Eq. {12}:

$$C'_{\text{int}} = C_{\text{int}}\left(1 + E_{XX} - 0.056E_{YY}\right) \qquad \{16\}$$

$$C'_{ext} = C_{ext}\left(1 + E_{XX} - 0.042E_{YY}\right)$$

$$L' = L\left(1 + 0.11E_{XX} + 0.89E_{YY}\right)$$

$$R' = R\left(1 - 0.58E_{XX} + 0.58E_{YY}\right)$$

Where the primes again denote the strained configuration and the unprimed values correspond to the baseline/unloaded condition.

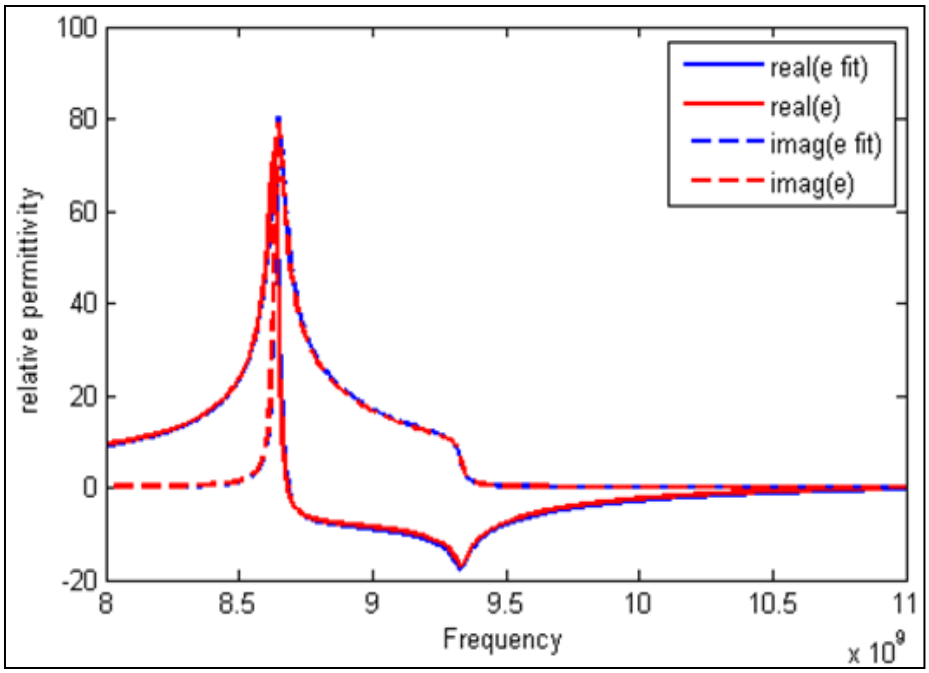

Figure 18. *Analytic (e fit) vs simulation-derived (e) permittivity curves for unit cell show in Figure 13 [54].*

As a general rule, a metamaterial's sensitivity to strain is configuration dependent. Relationships like Eqs. {4, 5, and 13} can be used to quickly and efficiently determine the strain–dependence (i.e. the slopes in the above expressions) of many unit cell variations that share the same circuit model.

Using the relationships of Eqs. {16}, the values for the capacitances, inductance, and resistance were determined for a given strain state. These values were input into equation {12}, and the aforementioned process repeated to produce the permittivity

curves for the deformed/strained unit cell. In Figure 19 and Figure 20, the strain-dependent analytic expression for the permittivity and permeability are compared to that found by retrieving the relevant parameters extracted from full-wave simulations. The curves shown are from the extreme values of the strain envelope modeled for this effort; $E_{XX}=E_{YY}=-5\%$ and $E_{XX}=E_{YY}=+5\%$.

As Figure 19 and Figure 20 clearly demonstrate, these relatively simple expressions accurately reproduce the quite disparate frequency responses at the different strain states.

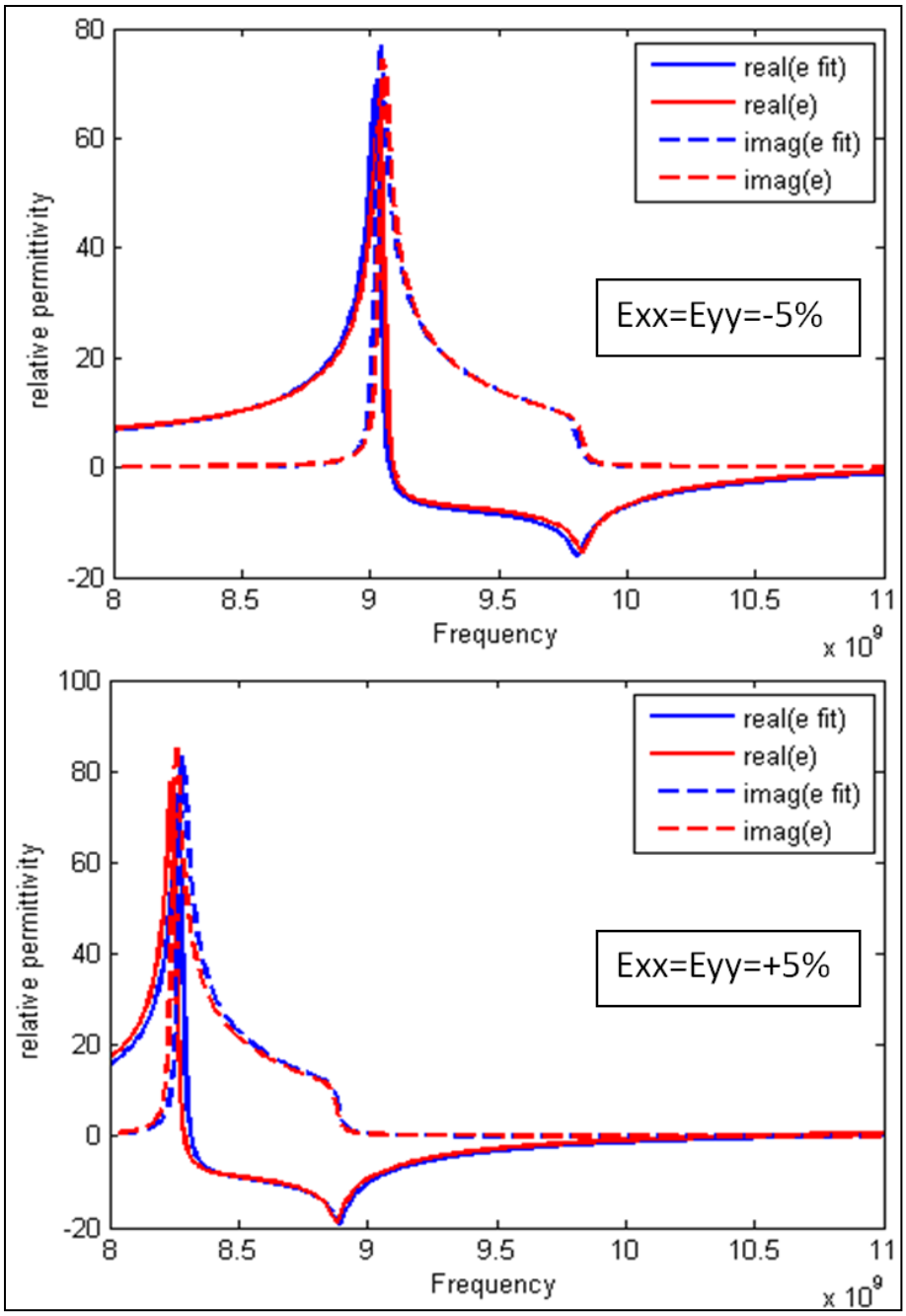

Figure 19. *Strain-dependent analytic expression of the permittivity (e fit) compared to full-wave simulations (e). The two graphs again demonstrate the high degree of agreement over a large range of strain states [54].*

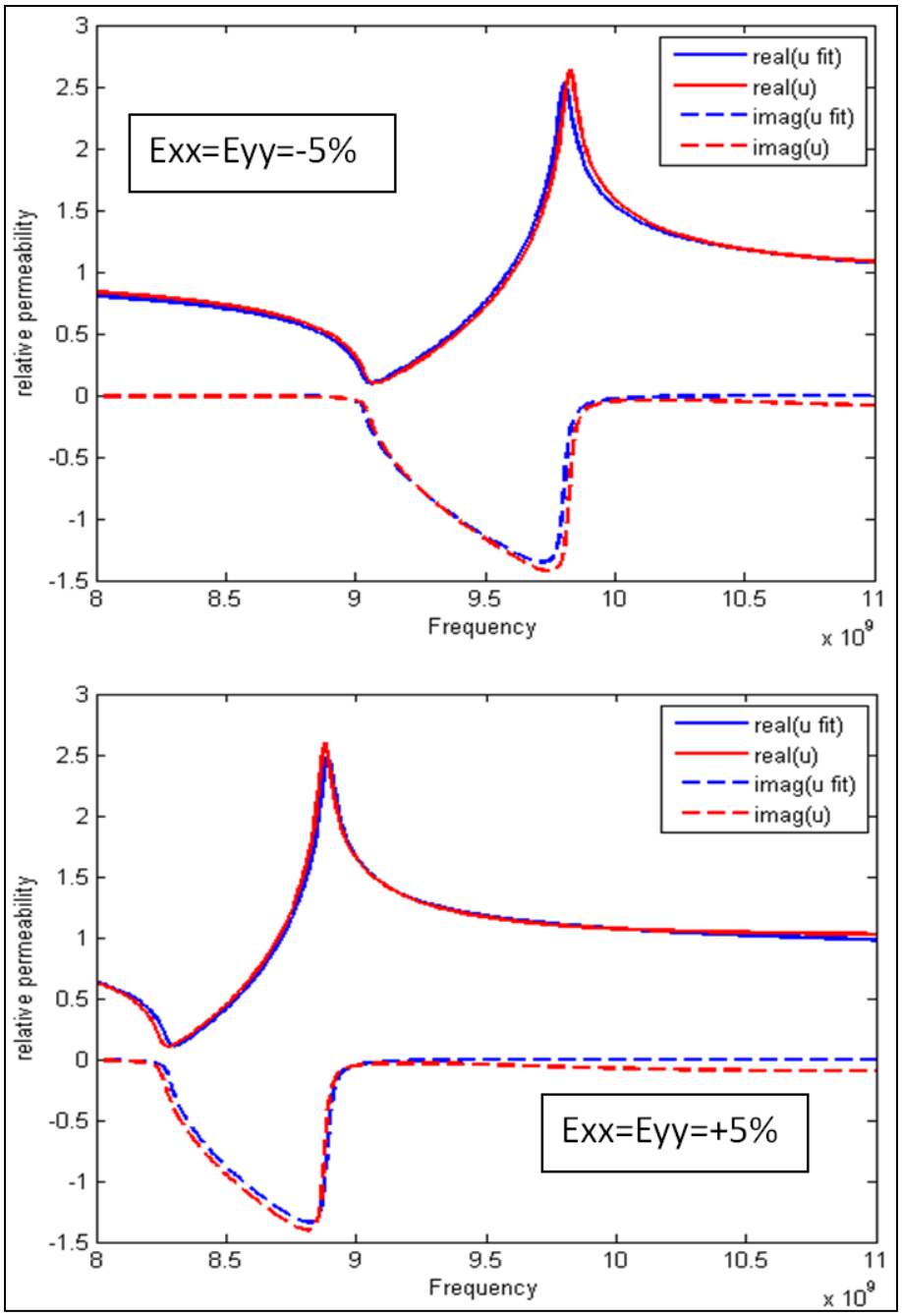

Figure 20. *Strain-dependent analytic expression of the permeability (u fit) compared to full-wave simulations (u). The two graphs again demonstrate the high degree of agreement over a large range of strain states [54].*

2.3.3 Conclusion

The agreement found for the permittivity of the ELC as derived from the analytic model and the full wave simulations demonstrates that a metamaterial's strain-dependent permittivity and permeability curves can be accurately reproduced though the use of an equivalent circuit model, and explicit expressions for those equivalent circuit elements (as verified using full-wave simulations). The expressions for capacitance, inductance, and resistance are readily described functions of geometry, and are thus easily modified to include small changes to that geometry (i.e. mechanical strain). Similar expressions and processes could be used to describe the strain-dependent electromagnetic behavior of magnetic metamaterials, owing to similar analytic expressions for their constitutive properties and equivalent circuit elements.

The use of analytical approximations to the circuit parameters as a means to introduce the effect of strain might seem unnecessary, since numerical simulations can readily account for these effects. Still, the set of analytical formulas enables a library to be developed for a given structure, and its performance rapidly assessed without resorting to full wave simulations. Moreover, as other physical effects are included, such as temperature dependence, quasi-analytical approaches become increasingly efficient and advantageous.

2.4 THE ROLE OF SUBSTRATE ELASTIC MODULUS IN THE STRAIN-DEPENDENT BEHAVIOR OF ELECTROMAGNETIC METAMATERIALS: MULTIPHYSICS MODELING AND TEST RESULTS

ψ Ratio of the strain in the conducting layer, to the strain at the unit cell level, $(\Delta l/l)/(\Delta d/d)$

E_{ii} Strain of the unit cell in the i-direction, $\Delta d_i/d_i$

ϵ_{ii} Differential strain at a point. Analysis restricted to normal strains, $\partial u_i/\partial x_i$

f_0 Resonant Frequency. $f_0=\omega_0/2\pi$

χ Ratio of the strain in the substrate, between conductive traces, to the strain at the unit cell level, $(\Delta s/s)/(\Delta d/d)$

ω_0 Angular resonant frequency. $\omega_0 = 2\pi f_0$

Y Young's, or Elastic, Modulus. The use of a subscript denotes a particular material.

2.4.1 Introduction

The studies detailed in the previous two sub-sections imparted the simplifying assumption that the stiffness (Elastic/Young's modulus) of the substrate was on the order of the stiffness of the conductive traces (in this case, copper). This assumption is valid for a wide range of envisioned metamaterial implementations, particularly those where the metamaterial will be integrated directly into/onto a load-bearing structure [44][45][46]. This simplification imparts a near uniform in-plane strain-profile throughout the metamaterial unit cell ($E_{ij} \approx \epsilon_{ij}$); i.e. the differential term for the in-plane

mechanical strain is constant throughout the unit cell, and identical to the global value. This enables straightforward analytic description of the metamaterial's strain-dependent constitutive properties through relatively simple geometric expressions.

However, a number of metamaterial structures utilize lower modulus dielectrics as the substrate material. When a softer substrate is utilized, mechanical loading imparts a significantly more complicated strain profile within the unit cell, as demonstrated in Figure 21 and Figure 22. As a result, interpretation of the deformed geometry, and the resultant change in the geometric parameters of the equivalent circuit elements, becomes increasingly complicated.

This section details efforts to understand the role that Elastic Modulus plays in the strain-dependent EM properties of metamaterial structures. Shear-lag models are utilized to explain strain transfer into the conductive traces of a metamaterial, and equivalent circuit models are leveraged to convey that knowledge into approximate predictions of a metamaterial's strain-dependent EM performance. Multi-physics modeling was performed to assess the metamaterial's strain-dependent EM performance, as a function of substrate modulus, and testing was conducted to verify and corroborate those models.

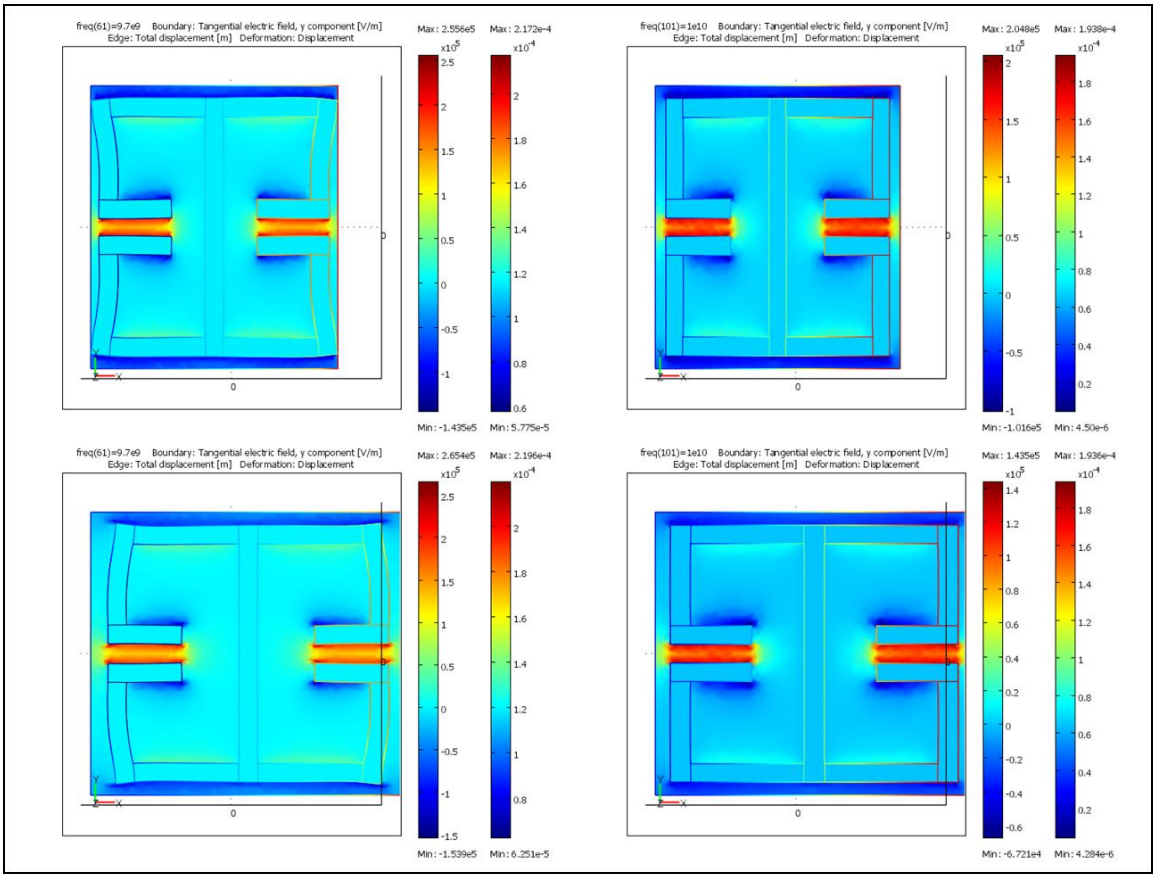

Figure 21. *Simulation results from COMSOL Multiphysics [57]. Electric field, superimposed on the (software exaggerated) deformed geometry. On the left are samples with low modulus substrates (Y*=1%), on the right are samples with high modulus substrates (Y*=100%). Y* is the ratio of the substrate to copper modulus. Top two pictures depict E_{xx}=-5%, bottom two pictures depict E_{xx}=+5%. The two scales to the right of each picture detail the strength of the electric field (left bar) and total displacement (right bar).*

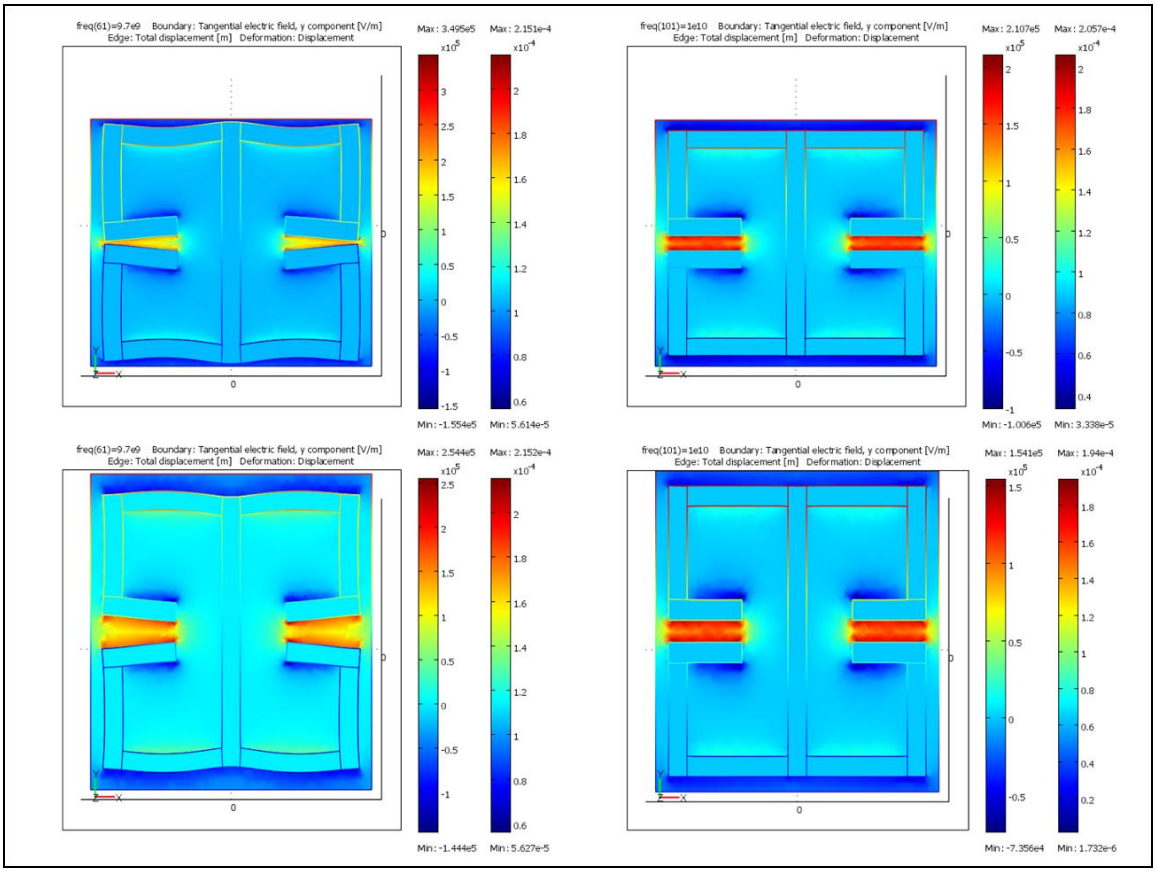

Figure 22. *Simulation results from COMSOL Multphysics [57]. Electric field, superimposed on the (software exaggerated) deformed geometry. On the left are samples with low modulus substrates (Y*=1%), on the right are samples with high modulus substrates (Y*=100%). Y* is the ratio of the substrate to copper modulus. Top two pictures depict* E_{yy}*=-5%, bottom two pictures depict* E_{yy}*=+5%. The two scales to the right of each picture detail the strength of the electric field (left bar) and total displacement (right bar)*

2.4.2. Multiphysics Modeling

2.4.2.1 Shear-Lag Models

Shear lag models, developed and utilized for the composites-repair and structural health monitoring communities [58][59][60][61][62], describe strain transfer into layered systems. These provide useful insight and intuition into the increasing level of non-homogeneity in the unit cell's strain profile as the substrate's modulus is decreased. Figure 23 depicts the geometric parameters used in the following shear-lag analysis.

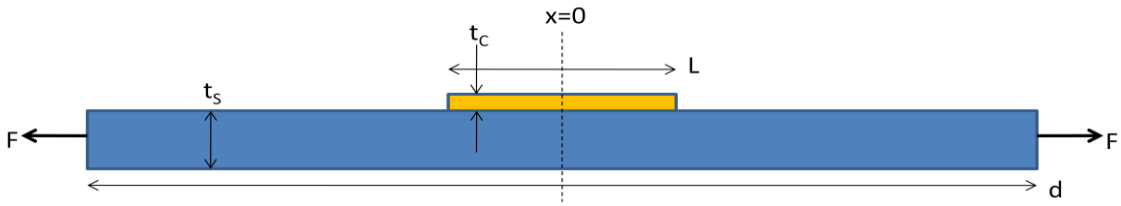

Figure 23. *Depiction of a conductive trace placed on a dielectric substrate. For the shear lag analysis, d>>L and L>>t_c, t_c=0.034mm and t_s=1.5875mm.*

The expressions from the 2-D analysis performed in [58] are normalized for a given boundary displacement (as opposed to a load at the boundary) to determine the level of stress in the conductive layer. Additionally, due to the construction of many metamaterial unit cells, it is reasonable to assume perfect bonding between the substrate and copper [63] (i.e. the substrate will fail before the bond), leading to the following expression for the stress in the copper.

$$\sigma_{XXC} = FS \Big/ t_C(1+S) = E_{XX}\left[St_S Y_S \Big/ t_C(1+S)\right] = E_{XX}\left[St^* Y_S \Big/ (1+S)\right] \quad \{17\}$$

Where S is the ratio defined by $S = \left(Y_C t_C / Y_S t_S\right) = 1/\left(Y^* t^*\right)$, Y is the material's Young's Modulus, $E_{XX} = \Delta d \Big/ d$, t are the thicknesses (Figure 23), $t^* = t_S / t_C$, and $Y^* = Y_S / Y_C$.

Assuming linear elastic behavior, the strain in the conductive layer is then found via Hook's Law

$$\in_{XXC} = \frac{\sigma_{XXC}}{Y_C} = \frac{E_{XX}}{Y_C}\left[St_S Y_S \Big/ t_C(1+S) \right] = E_{XX}\left[\frac{Y^* t^*}{Y^* t^* + 1} \right]. \qquad \{18\}$$

Figure 24 shows the strain profile in the copper, given a number of different modulus ratios (Y^*), and a prescribed 5% tensile boundary extension $(E_{XX} = 0.05)$.

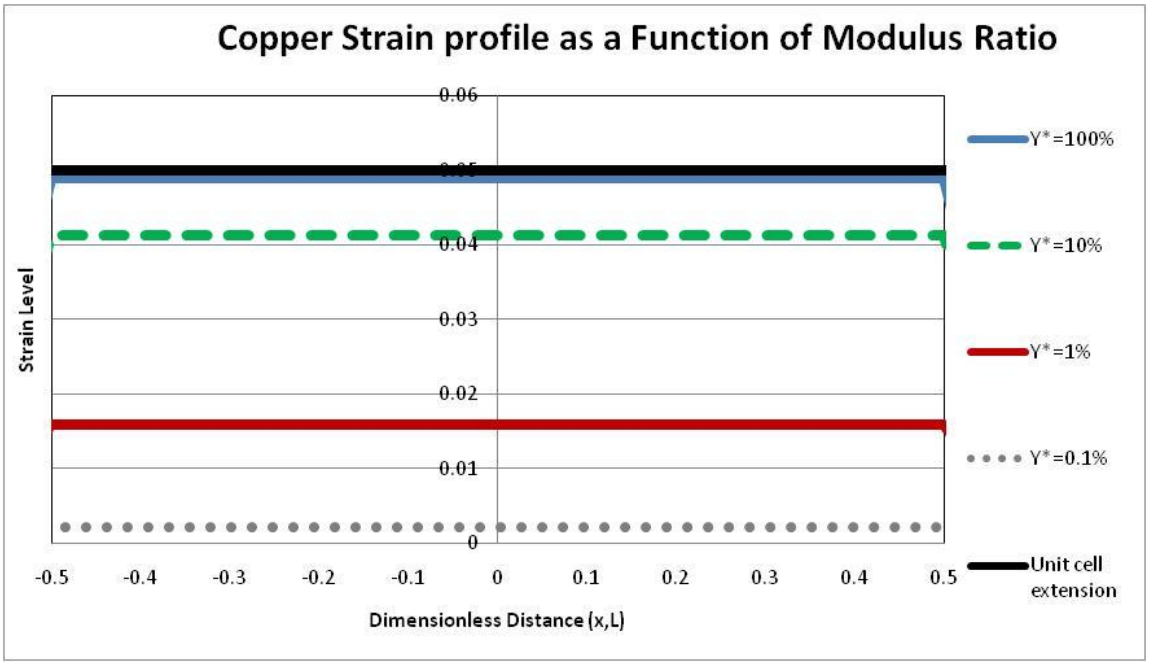

Figure 24. *Strain profile in the copper/conductive trace as a function of modulus ratio (Y^*). Analysis assumes perfect bonding between the conductive and dielectric substrate layers, a boundary strain of 5%, and t^*=46.7 (Figure 23).*

Integrating these solutions, with respect to *x*, provides the change in length in the copper (ΔL), for the given boundary displacement. Figure 25 shows the strain level in the copper $(\Delta L/L)$, as a function of modulus ratio (Y^*) and strain at the boundaries $(\Delta d/d)$.

As Figure 25 demonstrates, due to the thicknesses of the substrate and conductive layers, $\Delta L/L$ experiences a relatively minor change, even when there is a significant

disparity in the moduli (10:1) of the materials. As a result, there is little difference in the strain-dependent EM-performance of the Y^*=10% and Y^*=100% metamaterial structures. However, as the modulus ratio is further reduced, the extension of the copper decreases appreciably; implying a significantly different strain-dependence. These implications are validated later, via multi-physics FEM analyses.

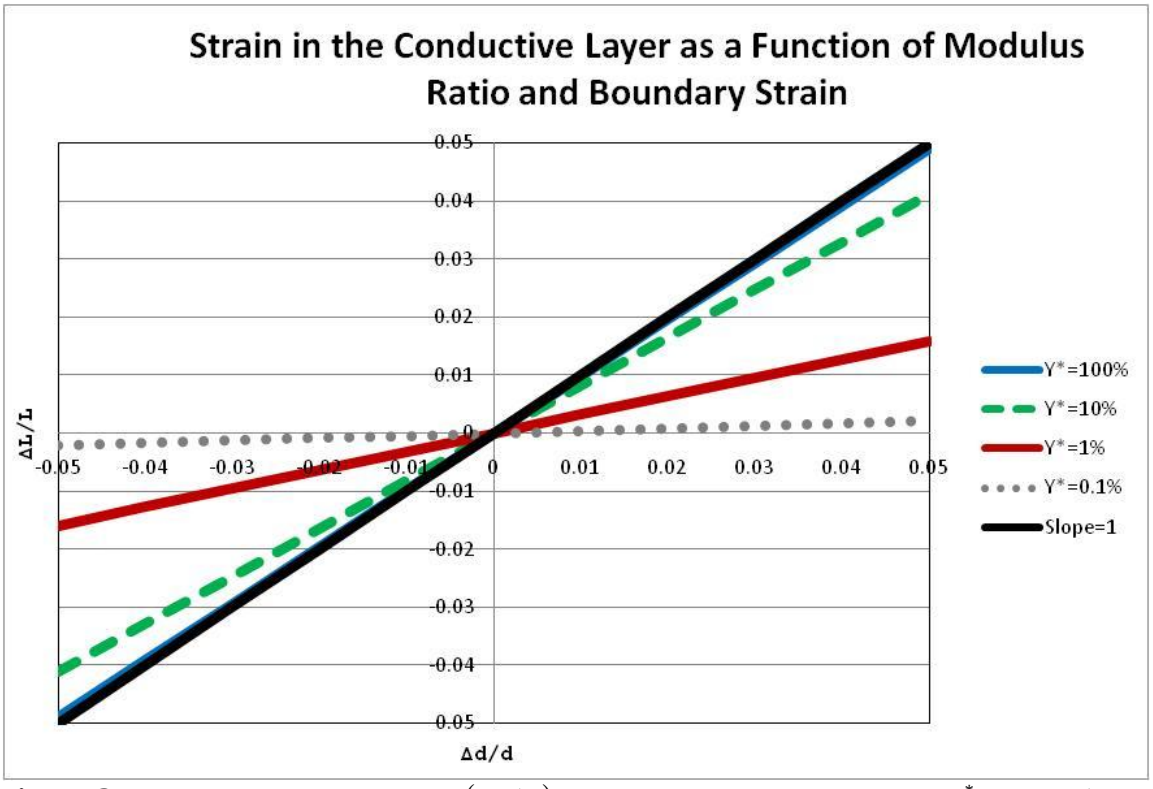

Figure 25. *Strain in the copper layer* $(\Delta L/L)$*, as a function of modulus ratio (*Y^**) and* $\Delta d/d$ *. A slope of 1* $(\Delta L/L = \Delta d/d)$ *is provided for reference.*

While the preceding shear-lag analysis was conducted on an idealized geometry (i.e. 2-D and d>>L, which are not representative of the geometry of a metamaterial unit cell), and does not account for shear-lag effects near the edges of the copper layer, the insight shall prove beneficial for understanding the interplay between substrate elastic modulus and the metamaterial's strain-dependent EM response.

2.4.2.2 Description via Equivalent Circuit Elements

As demonstrated in [28][29][30][50][54], the use of equivalent circuit elements can be extremely useful for gaining insight into the strain-dependent behavior of metamaterial structures. In Section 2.2, the strain-dependent resonant frequency for an ELC was predicted through the use of analytic expressions. The resonant frequency for the deformed unit cell is given by

$$\omega_0' = \sqrt{\frac{1}{L'C'}} = \omega_0 \sqrt{\frac{LC}{L'C'}} = \omega_0 \frac{1}{\sqrt{L^* C^*}}, \qquad \{19\}$$

Where the primes denote the deformed geometry and the unprimed values are the baseline/unstrained parameters, and $L^* = L'/L$ and $C^* = C'/C$. For reference, the self-inductance (L) of a thin, conducting strip can be approximated as [52]

$$L = \frac{\mu_0 l}{2\pi}\left[\ln\left(\frac{2l}{b}\right) + \frac{1}{2} + \frac{b}{3l} - \frac{b^2}{24l^2}\right] \qquad \{5\}$$

where l is length and b (Figure 13) is the width of the conducting strip. Loop inductance can be neglected, due to the symmetry of this unit cell [50][53][54]. The capacitance (C) for a co-planar capacitor can be approximated as [51]

$$\begin{aligned} C &= C_a + C_s \\ C_a &= \varepsilon_0 \frac{2}{\pi} \ln\left(2\beta \frac{2b+s}{s}\right) W \\ C_s &= \varepsilon_0 \frac{\varepsilon_s - 1}{\frac{s}{t_s} + \frac{4}{\pi}\ln\beta} W \end{aligned} \qquad \{4\}$$

Where the geometric parameters are detailed in Figure 13 and Figure 23, the subscript a and s refer to air and substrate, respectively, and $\beta = 5/2$.

As mentioned before, the previous sections analyzed a metamaterial that was constructed on a thick, high modulus substrate. These simplifying assumptions enabled direct integration of the strained geometry into the above analytic expressions, and ensured the capacitors remained approximately parallel in the strained condition. However, as the substrate modulus is decreased, the strain-profile for a mechanically-loaded unit cell becomes increasing complex (as depicted in Figure 21 and Figure 22) and defies direct description via analytic expressions.

However, utilizing the values for the strain in the copper that were determined in Section 2.4.2.1, as well as the geometry of the unit cell (Figure 26), it is possible to generate first-order approximations of the changes in dimensions for both the copper layer, and the substrate regions between conductive traces. The strain level in the conductive traces is found via Eq. {18}

$$\in_{iiC} = \psi E_{ii} = \left[\frac{Y^* t^*}{Y^* t^* + 1}\right] E_{ii} \qquad \{20\}$$

Where ψ is the ratio of the strain in the copper to the strain in the unit cell. To determine the strain level in the substrate layer, between conductive traces, one can leverage a natural consequence of strain compatibility in solid mechanics; because the analysis is limited to linear-elastic behavior, strain is a continuous function and does not allow regions of material gapping or overlap [64]. The following equation details that the total extension of the unit cell is equal to the sum of the extensions in the unit cell's components (conductive traces plus regions of substrate between conductive traces)

$$d\left(1+E_{ii}\right) = l_c\left(1+\psi E_{ii}\right) + l_s\left(1+\chi E_{ii}\right) = l_c\left(1+\psi E_{ii}\right) + \left(d-l_c\right)\left(1+\chi E_{ii}\right) \qquad \{21\}$$

Where l_c is the length of the conductive trace along the path of interest (Figure 26), l_s is the total length of substrate along the same path $\left(l_s = d - l_c\right)$, and χ is the ratio of the strain in the substrate (between conductive traces) to the strain at the unit cell level.

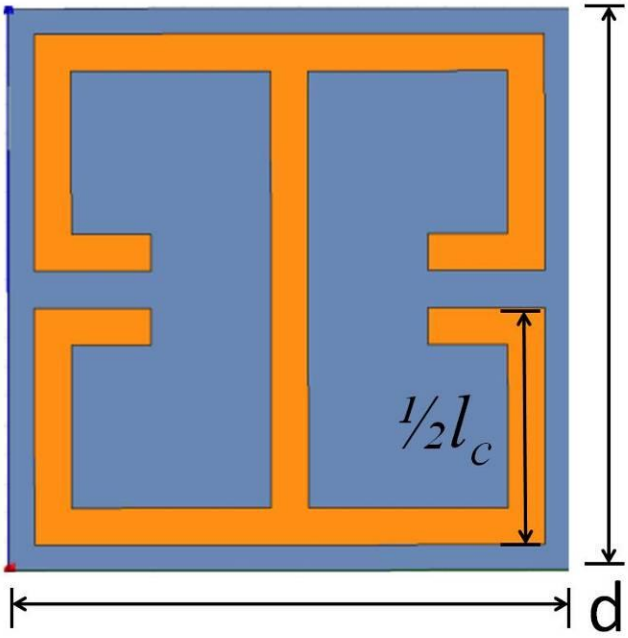

Figure 26. *Length of copper, used to calculate C_1 when subjected to E_{YY}.*

Solving Eq. {21} for χ leads to

$$\chi = \frac{1}{E_{ii}}\left(\frac{d\left(1+E_{ii}\right)-l_c\left(1+\psi E_{ii}\right)}{d-l_c}-1\right)=\frac{d-l_c\psi}{d-l_c}. \qquad \{22\}$$

The strain level in the substrate it then determined via the following equation,

$$\in_{iiS} = \chi E_{ii} = \frac{d-l_c\psi}{d-l_c}E_{ii} = \frac{d-l_c\left(\frac{Y^*t^*}{Y^*t^*+1}\right)}{d-l_c}E_{ii} = \frac{1-\frac{l_c}{d}\left(\frac{Y^*t^*}{Y^*t^*+1}\right)}{1-\frac{l_c}{d}}E_{ii}. \qquad \{23\}$$

Table 1 shows ψ and χ for a variety of Y^* values, given the dimensions shown in Figure 13 and Figure 23. As the table shows, a reduction in Y^* implies a reduction in the strain level in the conductive traces (ψ details the magnitude of the strain-reduction) and a

corresponding increase in strain in the substrate region between conductive traces (χ details the degree of strain-magnification).

Y^* (Modulus Ratio)	Ψ (Strain multiplier for Copper)	χ (strain multiplier for substrate)
∞	1	1
100%	0.98	1.11
10%	0.82	1.95
1%	0.32	4.67
0.1%	0.04	6.13
0	0	6.39

Table 1. *Strain multipliers for the conducting and substrate regions of the metamaterial sample. Analysis utilized dimensions detailed in Figure 13 and Figure 23; t*=46.7 and l_c=3.264mm.*

These values for ϵ_{iiC} and ϵ_{iiS} can then be incorporated into Eqs. {4 and 5} to determine the deformed geometry and describe the metamaterial's strain-dependent inductance and capacitance. The values for *L* and *C* are then used to determine the resonant frequency as a function of modulus ratio and strain/boundary displacement, via Eq. {19}. It is again important to note that this analysis is approximate because the analysis of Section 2.4.2.1 does not properly account for a) the finite dimensions of the unit cell, b) the unit cell's resistance to rotations in the conductive traces, and c) Eqs. {5} assume parallel capacitor pads when the unit cell is deformed under load; an assumption that is violated for certain loading scenarios as the modulus ratio decreases (Figure 21 and Figure 22). As a result this analysis tends to underpredict the extension in the copper and overpredict the extension in the unreinforced substrate layers.

Figure 27 and Figure 28 show the analytically-derived shifts in resonant frequency as a function of modulus ratio and E_{XX} and E_{YY}, respectively. The shift in resonant frequency is defined as

$$\Delta f_0 = f_0' - f_0 = \frac{\omega_0'}{2\pi} - \frac{\omega_0}{2\pi} \quad \{24\}$$

Where the primed values are at the deformed/loaded condition, and the unprimed values correspond to the baseline/unloaded state.

As Figure 27 demonstrates, the metamaterial's sensitivity to E_{XX} decreases monotonically with reduced modulus ratios. However, Figure 28 (E_{YY}) shows significantly different behavior. As the modulus ratio is reduced from 100% to 10%, the unit cell exhibits decreased sensitivity to loading in the Y-direction; similar to the results in Figure 27. However, as the modulus ratio is decreased further, the trend reverses direction (i.e. a tensile load now induces an increase, as opposed to a decrease, in the resonant frequency) and departs from linearity.

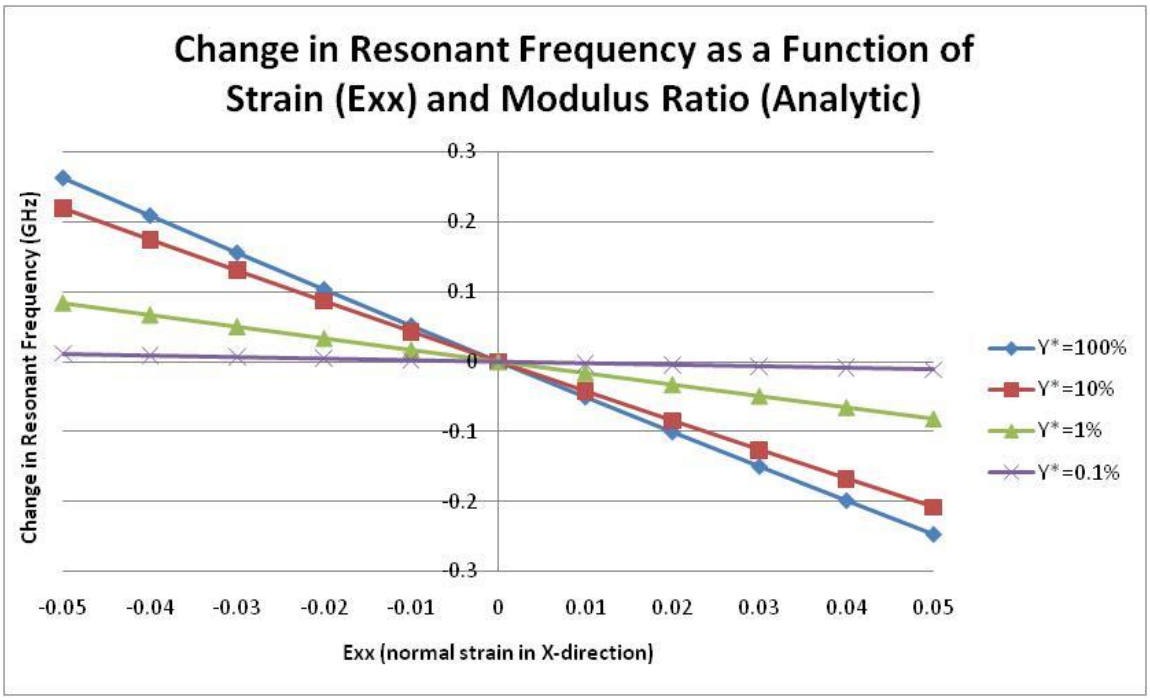

Figure 27. *Analytically derived shift in resonant frequency as a function of strain (E_{XX}) and modulus ratio*

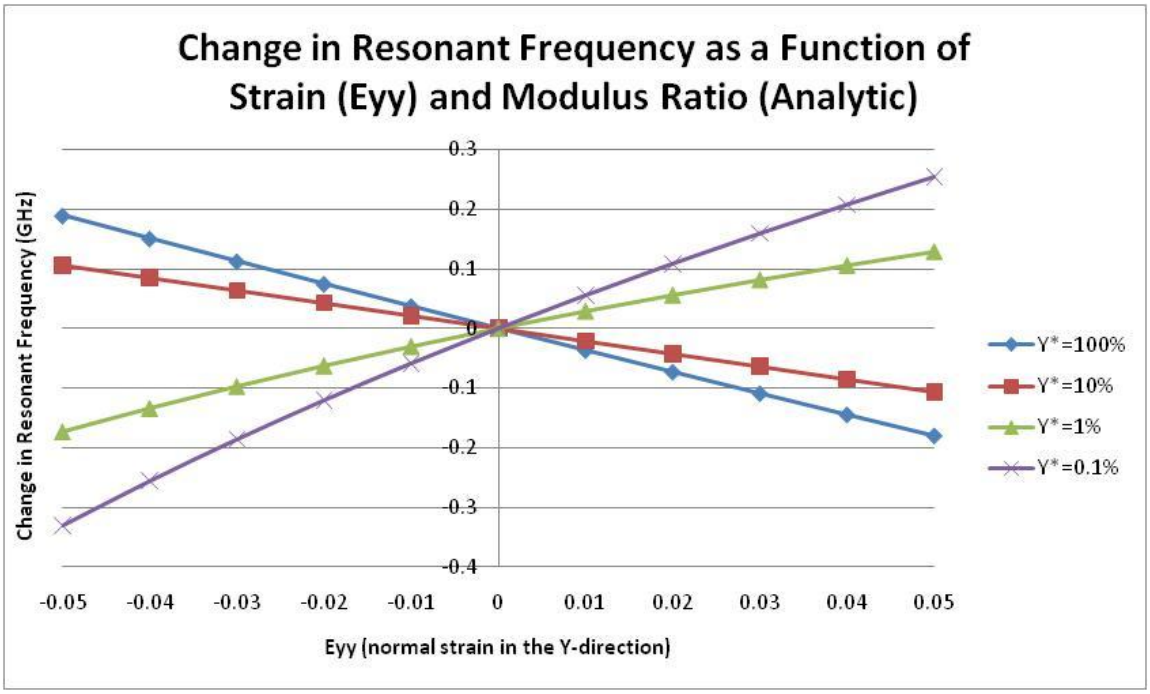

Figure 28. *Analytically derived shift in resonant frequency as a function of strain (E_{YY}) and modulus ratio*

To understand the physical mechanisms driving the relationship between modulus ratio, applied strain, and resonant frequency, it is useful to break that function into its constituent components: L and C.

Figure 29 shows how the unit cell's inductance changes with E_{XX}, for a variety of modulus ratios. Strain/boundary displacements in the X-direction impart changes to the dimensions "*l*" and "*b*" in Eq. {5}; both of which are dimensions relating to the conductive traces of the metamaterial unit cell. Since low values of Y^* lead to reduced strain transfer into the conductive traces, a reduction in modulus ratio necessarily leads to reduced E_{XX}-dependence in the unit cell's inductance.

Figure 30 show the capacitance as a function of E_{XX} and modulus ratio. E_{XX} alters the parameter "*W*" in Eqs. {4}, which is also a dimension relating to the conductive traces. As a result, lower values of Y^* similarly translate into reduced sensitivity in the metamaterial's capacitance, when subjected to applied normal strains in the X-direction (E_{XX}).

Since both the inductance and capacitance of the metamaterial exhibit reduced sensitivity to E_{XX} at low values of Y^*, the resonant frequency similarly becomes less sensitive to E_{XX} at low values of Y^*; thus explaining the trends depicted in Figure 27.

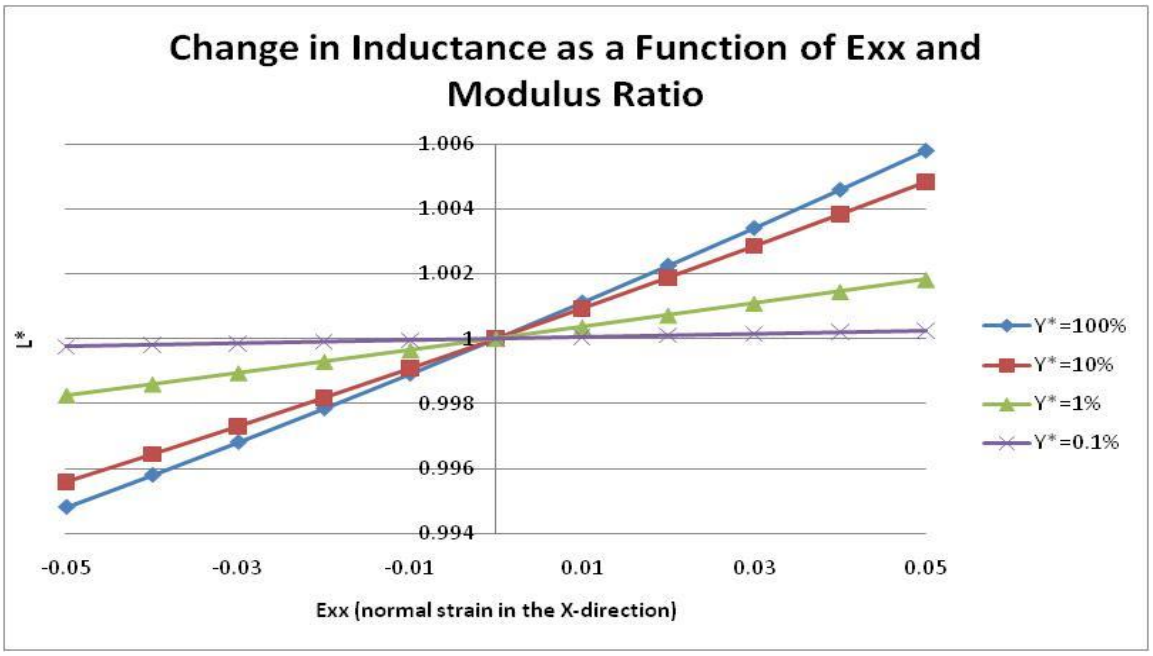

Figure 29. *Analytically-derived, normalized change in unit cell inductance, as a function of E_{XX} and modulus ratio.*

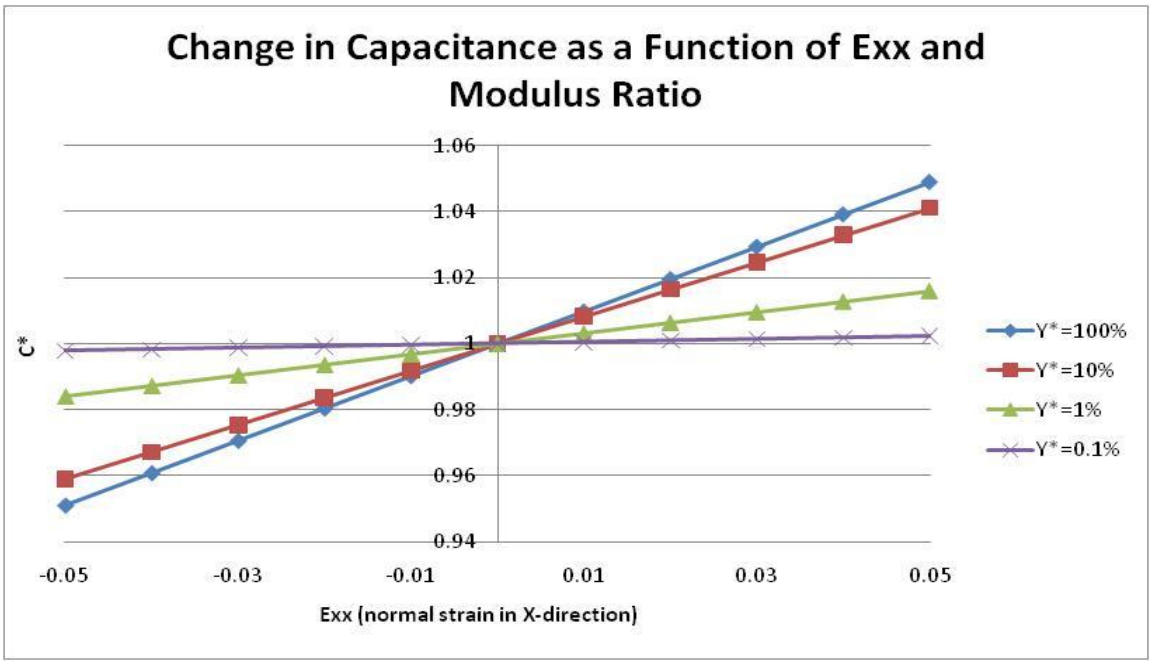

Figure 30. *Analytically-derived, normalized change in unit cell capacitance, as a function of E_{XX} and modulus ratio.*

Figure 31 and Figure 32 show the change in the unit cell's inductance and capacitance, respectively, as a function of E_{YY} and Y^*. Similar to the X-directed strains, boundary displacements in the Y-direction impart changes to the dimensions "*l*" and "*b*" in Eq. {5}. Thus, a lower Y^* value translates into lower strain levels being conveyed into the conductive traces, and a unit cell inductance that demonstrates lower sensitivity to applied strain. This trend is depicted in Figure 31.

A Y-directed strain imparts changes to the dimensions "*s*" and "H" in Eqs. {4}; note that $H=2b+s$. "*b*" is a dimension of the conductive traces, and "s" is a substrate dimension. As shown in Table 1, the substrate dimensions demonstrate much greater sensitivity to applied strains at lower values of Y^*; thus, Eqs. {4} demonstrate increased sensitivity to Y-directed strains at lower values of Y^*. Additionally, as shown in Figure 32, Eqs. {4} become increasingly non-linear at low Y^* values.

It now becomes apparent that the features of Figure 28 (non-linearity, reversal of trend) depict a change from inductance-dominated behavior at high Y^* values to capacitance-dominated behavior at low Y^* values.

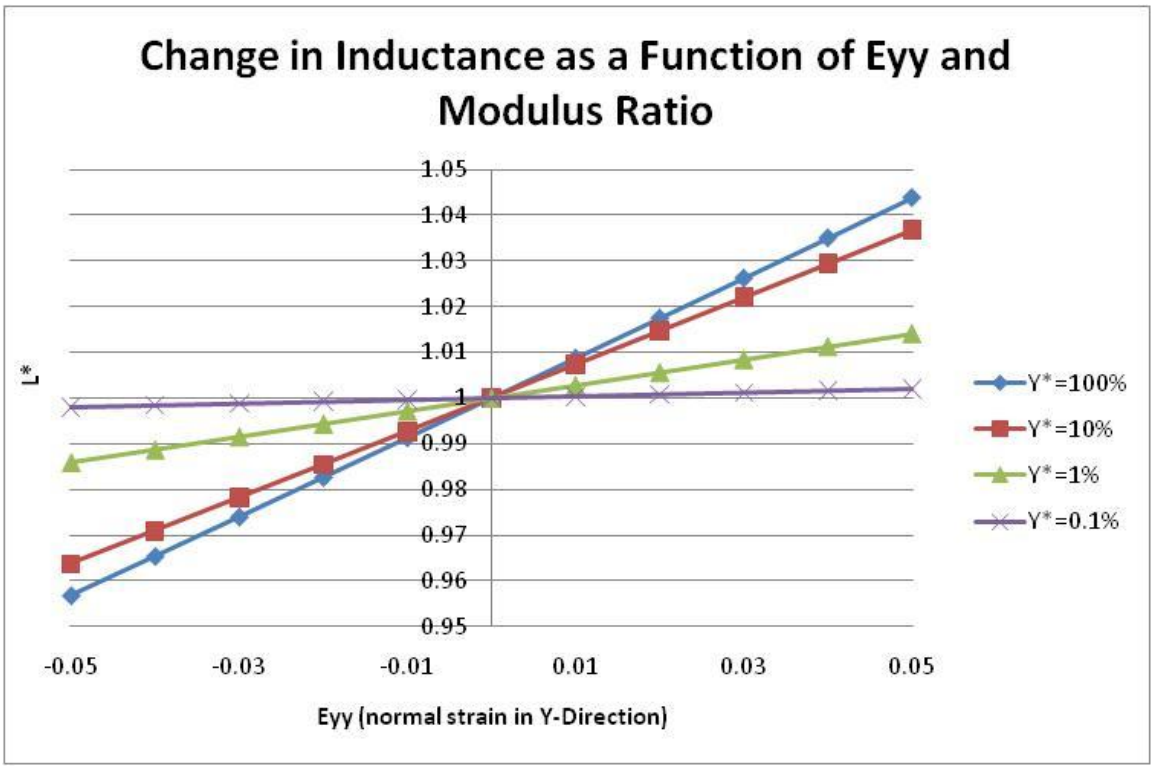

Figure 31. *Analytically-derived, normalized change in unit cell inductance, as a function of E_{YY} and modulus ratio.*

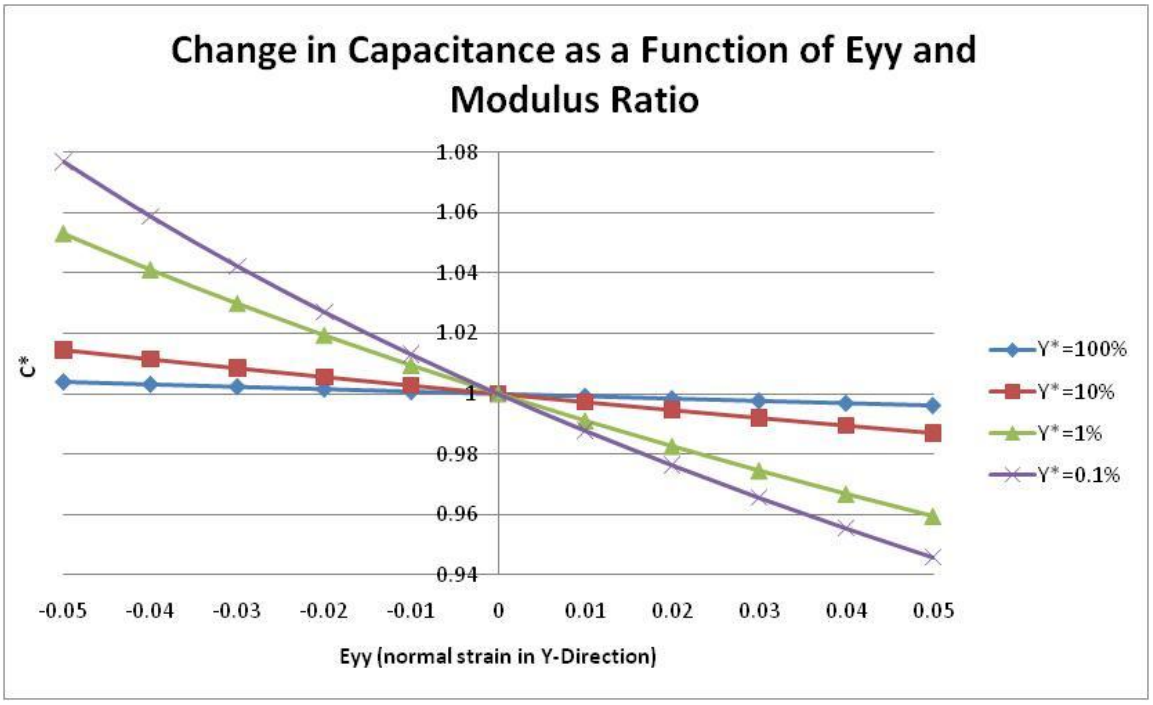

Figure 32. *Analytically-derived, normalized change in unit cell capacitance, as a function of E_{YY} and modulus ratio.*

2.4.2.3 Finite Element Modeling (FEM)

To effectively model the complex interplay between mechanical loading, constituent mechanical properties, and EM performance, COMSOL Multiphysics 3.5a [57] was utilized to directly measure the EM performance of the mechanically-strained unit cell. The unit cell does not incorporate electro- or magneto-strictive materials so it is assumed that the relationship between mechanical strain and EM performance is causal (as opposed to coupled), implying that mechanical strain influences the EM performance, but the EM environment does not directly impart mechanical loading/strain on the unit cell. Consistent with the previous analyses, mechanical loads/strains are conveyed into the unit cell via displacements at the periodic boundary surfaces to enable direct comparison of the strain-dependent response of metamaterials with differing substrate moduli. Additionally, this loading method enabled direct comparison with the ANSYS-HFSS [39] results from [50],[54] and Section 2.2, which ensured consistency between the disparate models and software packages (i.e. model verification) and allowed model validation with the test results, presented later.

The Structural Mechanics module in COMSOL was utilized to determine the complex, 3-D deformed geometry of the loaded metamaterial unit cell (some examples shown in Figure 21 and Figure 22). As in the previous sections, the mechanical model assumes linear elastic behavior in the constituent materials. The deformed geometry was then tracked by the Arbitrary Lagrangian-Eulerian (ALE) moving mesh mode in order to serve as the configuration for the EM analysis in the RF Module.

The model was constructed to take advantage of nested parameter sweeps. Boundary displacements were stepped from -5 to +5% $(\Delta d/d)$, in one direction, while

the orthogonal boundaries were constrained. Within each loading step, the deformed geometry was incorporated into the RF Module in order to perform a frequency sweep and extract S-parameter data.

Figure 33 and Figure 34 show the COMSOL results detailing the change in resonant frequency as a function of strain and modulus ratio. The dimensions and parameters are the same as those described in Figure 13 and Figure 23. As in Section 2.2, the shift in the metamaterial's resonant frequency is the superposition of the influence of the individual strain components. Note the similarity between the numerical results (Figure 33 and Figure 34) and the first-order analytic approximations (Figure 27 and Figure 28).

As in Figure 27, Figure 33 shows a reduction in modulus ratio leads to a decrease in the metamaterial's sensitivity to X-directed normal strains. As described earlier, a softer substrate conveys less strain into the conductive traces, resulting in less change in the unit cell's inductance and capacitances. Additionally, the trend remains approximately linear over the range of material properties investigated.

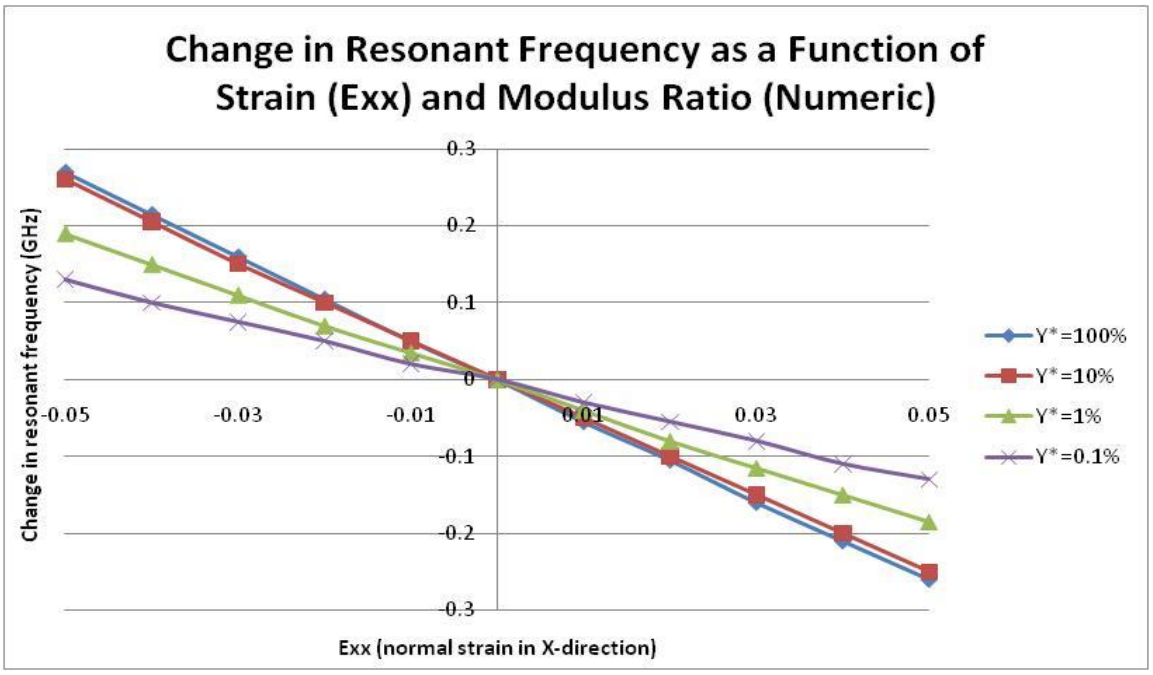

Figure 33. *Numerically derived shift in resonant frequency as a function of strain (Exx) and modulus ratio*

Figure 34 shows the metamaterial's shift in resonant frequency as a function of modulus ratio and strain in the Y-direction. Similar to the trends depicted in Figure 28, as the substrate's modulus is continuously decreased, the numerical results predict a decrease in the metamaterial's sensitivity to strain, eventually resulting in a departure from linearity, and an eventual reversal of the trend. As detailed in Section 2.4.2.2, when the modulus of the substrate drops below a critical value, a tensile strain in the Y-direction now results in an *increase* in the metamaterial's resonant frequency.

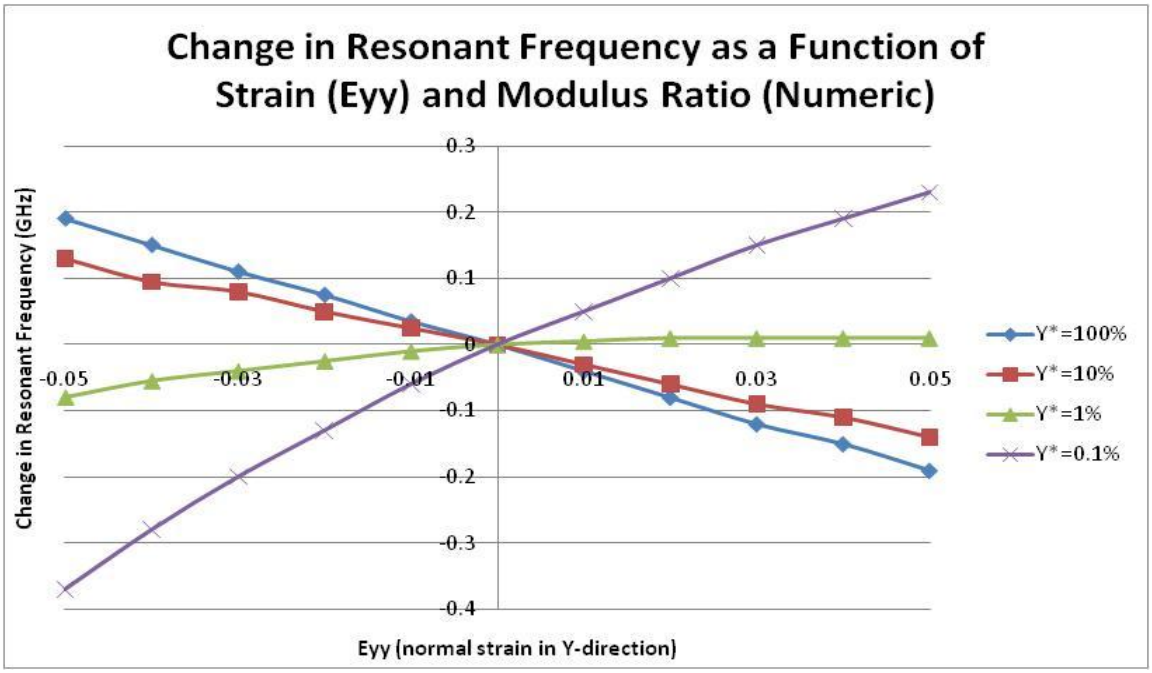

Figure 34. *Numerically derived shift in resonant frequency as a function of strain (Eyy) and modulus ratio*

Figure 21 and Figure 22 show some of the simulations results depicting the electric fields superimposed over the deformed geometry of the unit cell. Figure 21 (E_{XX}) shows that the capacitors remain approximately parallel, even when utilizing a low modulus substrate and applying relatively large levels of strain. Additionally, the softer substrate conveys a diminished level of strain into the conductive traces, resulting in decreased sensitivity to the applied boundary displacements.

Figure 22 (E_{YY}) demonstrates a similar reduction of the extension in the conductive layer, when using a softer substrate. However, of particular interest are the exaggeration of the change in the capacitive gap and the non-parallel orientation between the capacitor faces (for low values Y^*). Both of these factors help to explain the departure from linearity as the modulus of the substrate is reduced.

2.4.3 Testing

2.4.3.1 Metamaterial Samples

The metamaterial samples tested in this effort featured a 6”x6” metamaterial section (array of copper traces), centered on a 6”x12” piece of dielectric substrate material. This provided a large metamaterial region for free-space characterization, and provided a near-uniform strain-field within the central portion of the sample; where the majority of the energy from the Gaussian microwave beam was focused. The substrate materials chosen for this effort were Rogers RT/Duroid 5880 [38] and Pyralux [65].

Three different configurations, with two samples per configuration, were produced to test different strain profiles and material properties. The sample configurations are shown in Table 2.

2.4.3.1.1 Mechanical Characterization

To verify the mechanical properties required for analytic and numerical analyses, as well as the development of the loadframe control schemes (detailed later), substrate materials were tested in accordance with ASTM D 3039 [66] or ASTM D 882 [67], depending upon the thickness of the materials. Figure 35 and Figure 36 show the stress strain curves for the 5880 and Pyralux, respectively.

As seen in the curves, the 5880 is an inherently non-linear material; removing the load also demonstrated the material to be inelastic over the tested range. The Pyralux, on the other hand, demonstrated a higher degree of linearity and elasticity. For both materials, it was assumed they could be approximated as linear, for the range of anticipated strains, with minimal loss of accuracy. For the 5880, a Young’s Modulus of 1.75 GPa / 254 ksi was utilized, while a value of 8 GPa / 1160 ksi was used for the

Pyralux. Both values were significantly higher than the published values provided by the vendors.

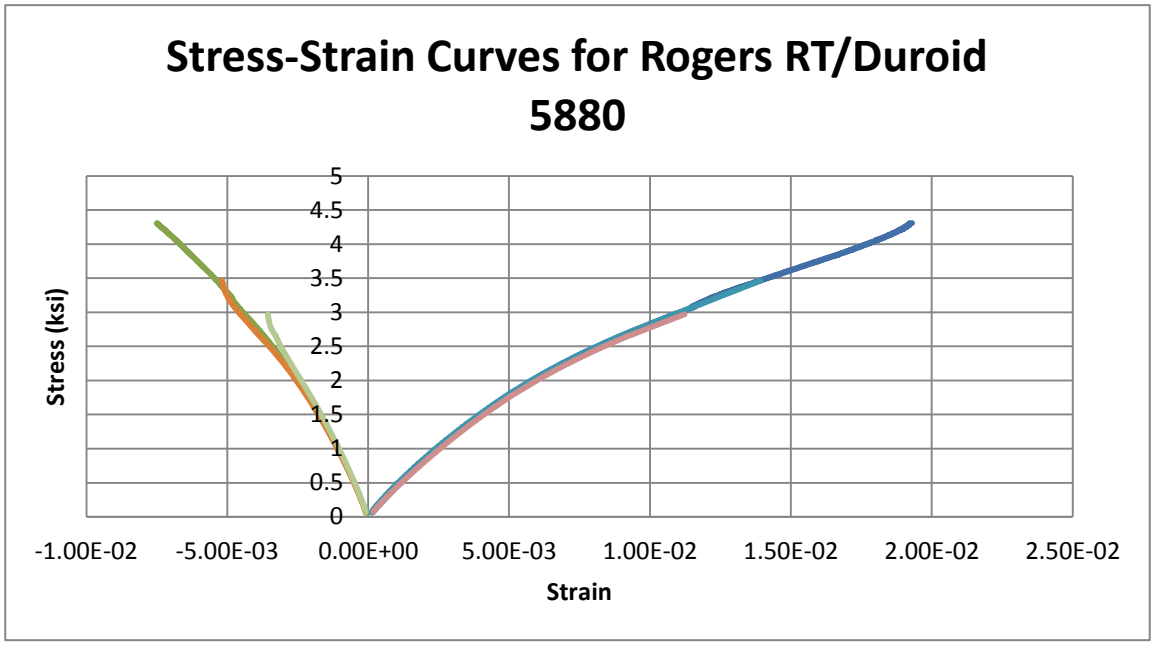

Figure 35. *Stress-strain curves for RT/Duroid 5880. Curves to the right show strain in the direction of loading, curves to the left show strain in the orthogonal direction.*

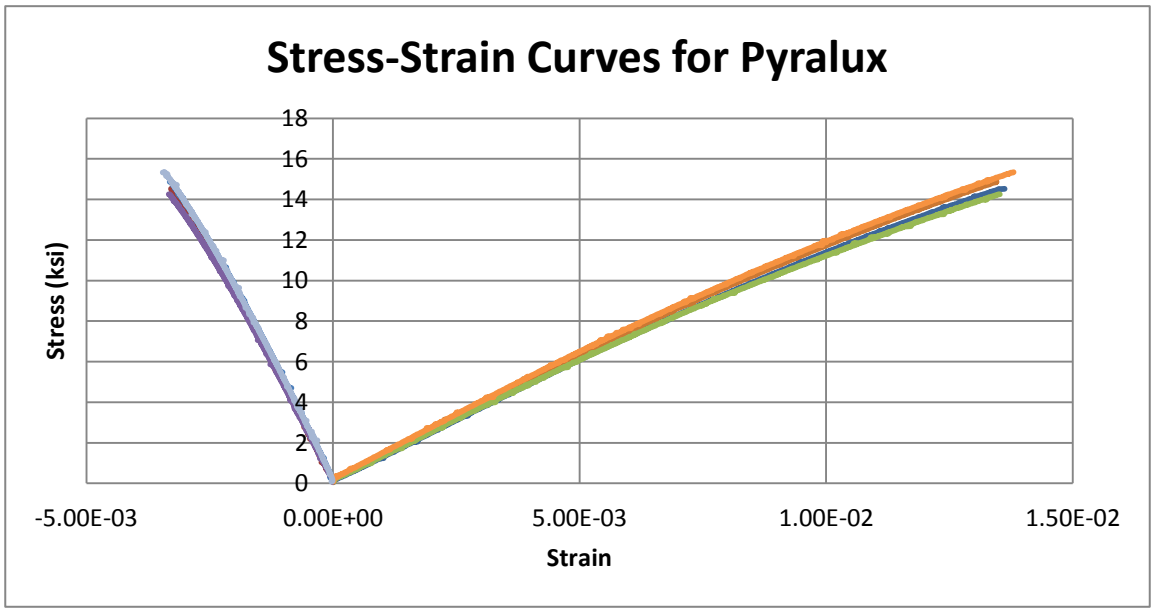

Figure 36. *Stress-strain curves for the Pyralux. Curves to the right show strain in the direction of loading, curves to the left show strain in the orthogonal direction.*

Table 2 shows the different configurations, and the as-tested values of Y*, t*, ψ, χ, and ε_s for the samples.

Substrate Material	**Copper Thickness**	**Y***	**t***	**Y*t***	ψ	χ	ε_s
Pyralux	0.5oz/17µm	7.3%	12.3	0.9	0.33	4.6	3.5
Pyralux	1oz/34µm	7.3%	6.2	0.5	0.44	4.0	3.5
5880	1 oz/34µm	1.6%	46.7	0.8	0.47	3.8	2.2

Table 2. *Metamaterial sample configurations.*

2.4.3.1.2 Numerically-Predicted Strain-Dependence

COMSOL was used to predict the metamaterial samples' sensitivity to boundary displacements. Figure 37 shows the results from the multi-physics modeling. Of note is the similarity in the trends. While the modulus of the 5880 is much lower than that of the Pyralux, the 5880 samples were significantly thicker. Additionally, the copper traces were much thinner (i.e. "*b*" in Eqs. {4 and 5} was ~0.1mm, as opposed to the 0.254mm specified to the vendor), resulting in less structural rigidity and a greater amount of strain being conveyed into the copper. According to the COMSOL simulation results (Figure 37), the shift in resonant frequency can be described via the following set of equations, which allow predictions of the resonant frequency for arbitrary strain profiles (values of E_{XX} and E_{YY}) in the metamaterial:

$$\Delta f_0^{Pyralux} = -4.37E_{XX} - 1.87E_{YY}$$
$$\Delta f_0^{5880} = -4.78E_{XX} - 1.97E_{YY} \quad . \qquad \{25\}$$

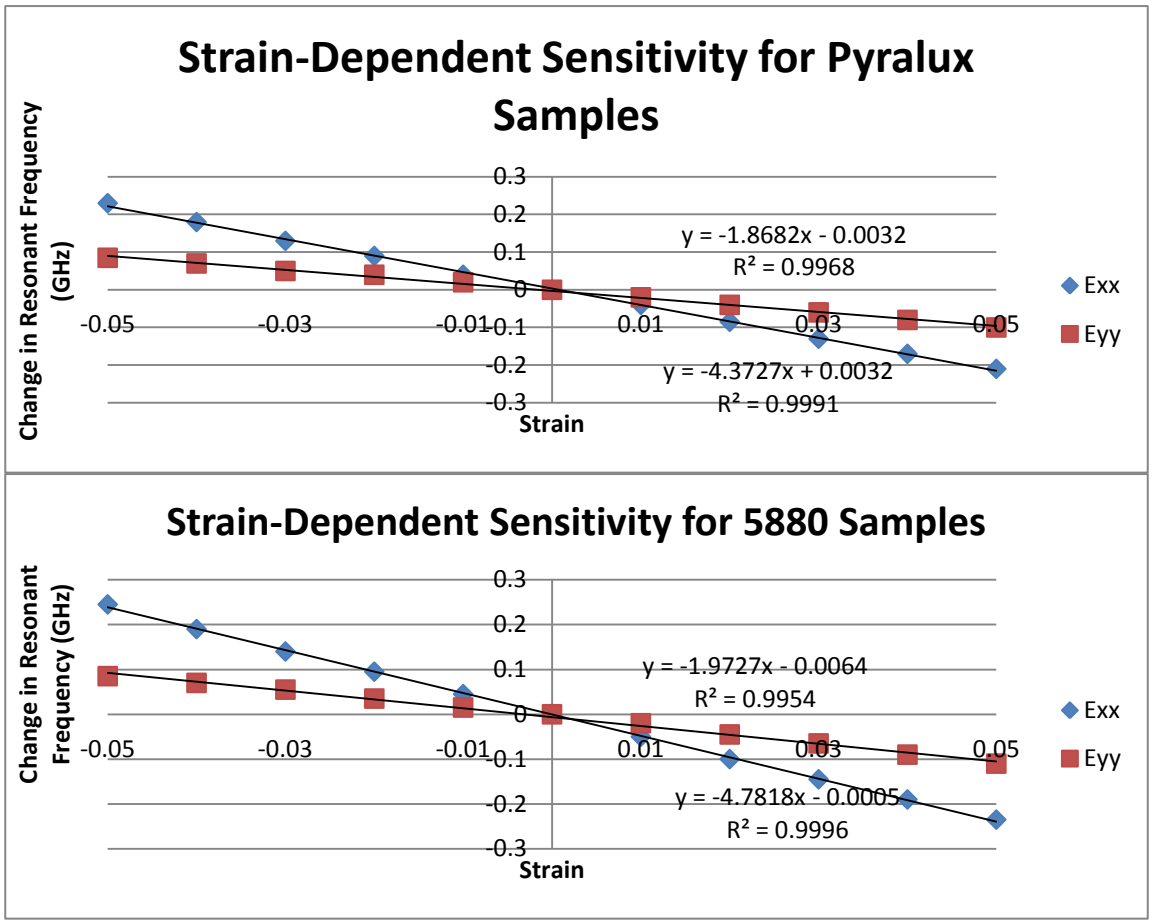

Figure 37. *Numerically derived (COMSOL) sensitivity with applied strain for the Pyralux and 5880 samples. Included are linear curves, fit to the data. These trends are required to correlate the strain profile with the change in resonant frequency. The Pyralux samples with ½ and 1 oz copper traces exhibited a 2% difference in the trends predicted in the modeling.*

2.4.3.2 *EM Characterization of Mechanically-Loaded Metamaterials*

2.4.3.2.1 Set-Up

A unique test facility was established at the Center for Metamaterials and Integrated Plasmonics at Duke University in order to generate empirical data on the strain-dependent EM performance of metamaterial samples. An Instron [68] 5567, 30 kip electromechanical loadframe served as the centerpiece for the facility and was used to impart mechanical loads into the metamaterial sample, via a set of 6-inch wide wedge grips, developed by Wyoming Test Fixtures [69]. The wedged design grips the sample

with a compressive force proportional to the tensile load applied via the loadframe (i.e. the clamping force increases as the loading on the sample is increased). This prevents the sample from prematurely tearing due to excessive compressive loading at the grip faces. Due to the smooth surface finish of the metamaterial samples, tungsten-carbide grit was chosen for the grip-face surfaces in order to prevent slippage during tensile testing. Additionally, the design of the wedges ensure the central plane of the sample is coincident with the load axis of the test frame. S-parameter characterization of the metamaterial sample was accomplished with an Agilent Technologies N5245A PNA-X Network Analyzer [70]. Rozendal Associates [71] RF Horns (frequencies of operation: 8.2-12.4 GHz) with 2 foot focal length lenses, provided a focused Gaussian beam at the center of the metamaterial sample. Figure 38 shows the test facility at Duke University.

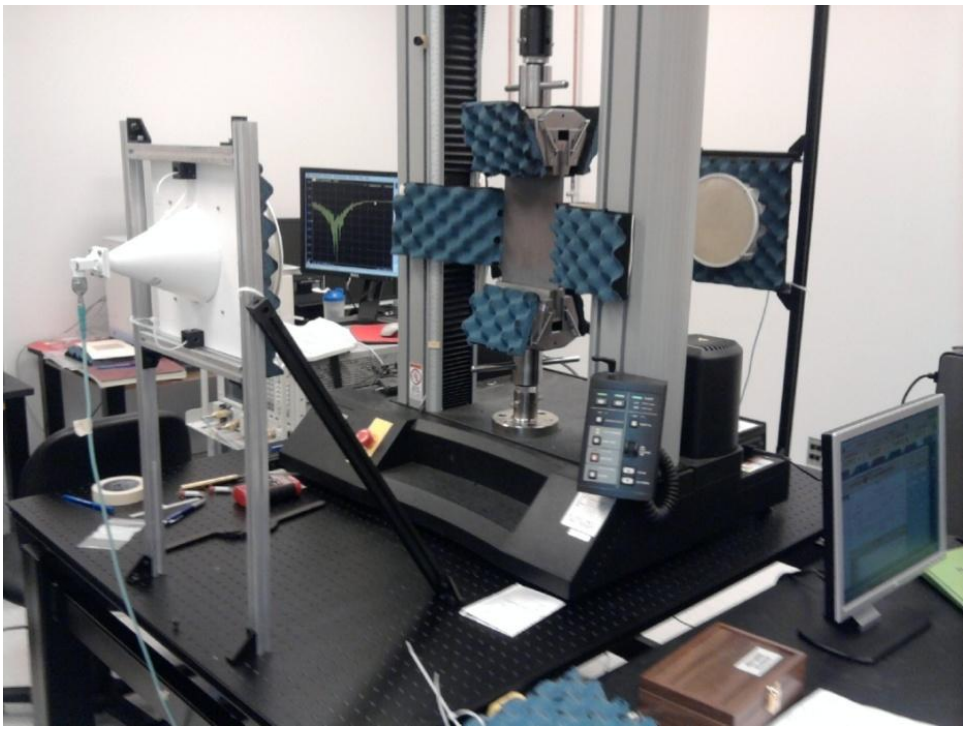

Figure 38. *Multiphysics metamaterial test facility. Shown in the picture are the metamaterial sample, the loadframe, loadframe control computer, wedge grips, RF horns and focusing lenses, and vector network analyzer*

This research also required a method for assessing the strain-field on the metamaterial surface. Photogrammetry was chosen because it a) provides a continuous description of the strain-field over a large area and b) does not interfere with the RF characterization of the metamaterial. A 16 megapixel Nikon/Kodak Professional SLR camera [72], with a non-zooming, wide angle lens, and high performance flash were used to generate the high-resolution imagery necessary to determine the strain profile on the loaded metamaterial samples.

2.4.3.2.2 Test Conduct

To prepare the facility for the metamaterial characterization, a thick metal plate was placed in the wedge grips and tension was applied from the loadframe. This was performed to ensure the wedge grips were coplanar (not rotated with respect to one another) and maintained that relationship as load was applied to the sample. Twin laser levels were then aligned with witness marks on the sides of the wedge grips. The mechanical linkage between the loadframe and wedge grips provided some laxity about the Y-axis. The laser levels and witness marks provided assurance that the front plane did not translate or rotate between the calibration steps and testing of the metamaterial samples (critical for future retrieval of the sample's permittivity and permeability). In tests conducted at the Air Force Research Laboratory/Space Vehicles Directorate (detailed in the Appendix), a VICON IR motion capture system [73] validated this process, determining out-of-plane displacements (between samples) were on the order of $1/50^{th}$ of a wavelength ($\lambda/50$). The laser levels and witness marks were utilized every time a sample was replaced, ensuring the grips did not rotate between RF characterization

steps. Additionally, the "return to zero" function on the loadframe was utilized to ensure a consistent Y-location of the grips for all calibration steps and metamaterial tests.

This testing required a high level of resolution in the S-parameter data generated from the testing. As a result, a Gated Reflect Line (GRL) calibration, utilizing the Agilent's Freespace Calibration software [70], was performed to mitigate the effects of standing waves in the facility. To ensure the accuracy of the GRL calibration, samples (acrylic, styrene) with known material properties (permittivity and permeability) were tested to validate the quality of the calibration.

After calibration, the metamaterial sample was clamped, via the wedge grips, within the loadframe. Baseline/no load RF characterization was performed on the sample. A number of time-gates were utilized to ensure the test data captured the resonant behavior of the metamaterial while minimizing the effects of standing waves. Figure 39 shows the S-parameters retrieved from a sample, using a variety of time-gates. The time gates used are shown in Table 3; a time of zero equates to the time at which the electromagnetic wave hits the front surface of the sample. All test results given in the remainder of this paper utilize time gate #2.

	Gate Entrance	**Gate Exit**
Gate 1	-500 ps	1 ns
Gate 2	-500 ps	2 ns
Gate 3	-500 ps	3 ns
Gate 4	-500 ps	4 ns

Table 3. *Entrance and exit times for the timegates used for the RF characterization of the metamaterial samples. For the times shown, a value of zero indicates the time at which the electromagnetic wave hits the front surface of the sample.*

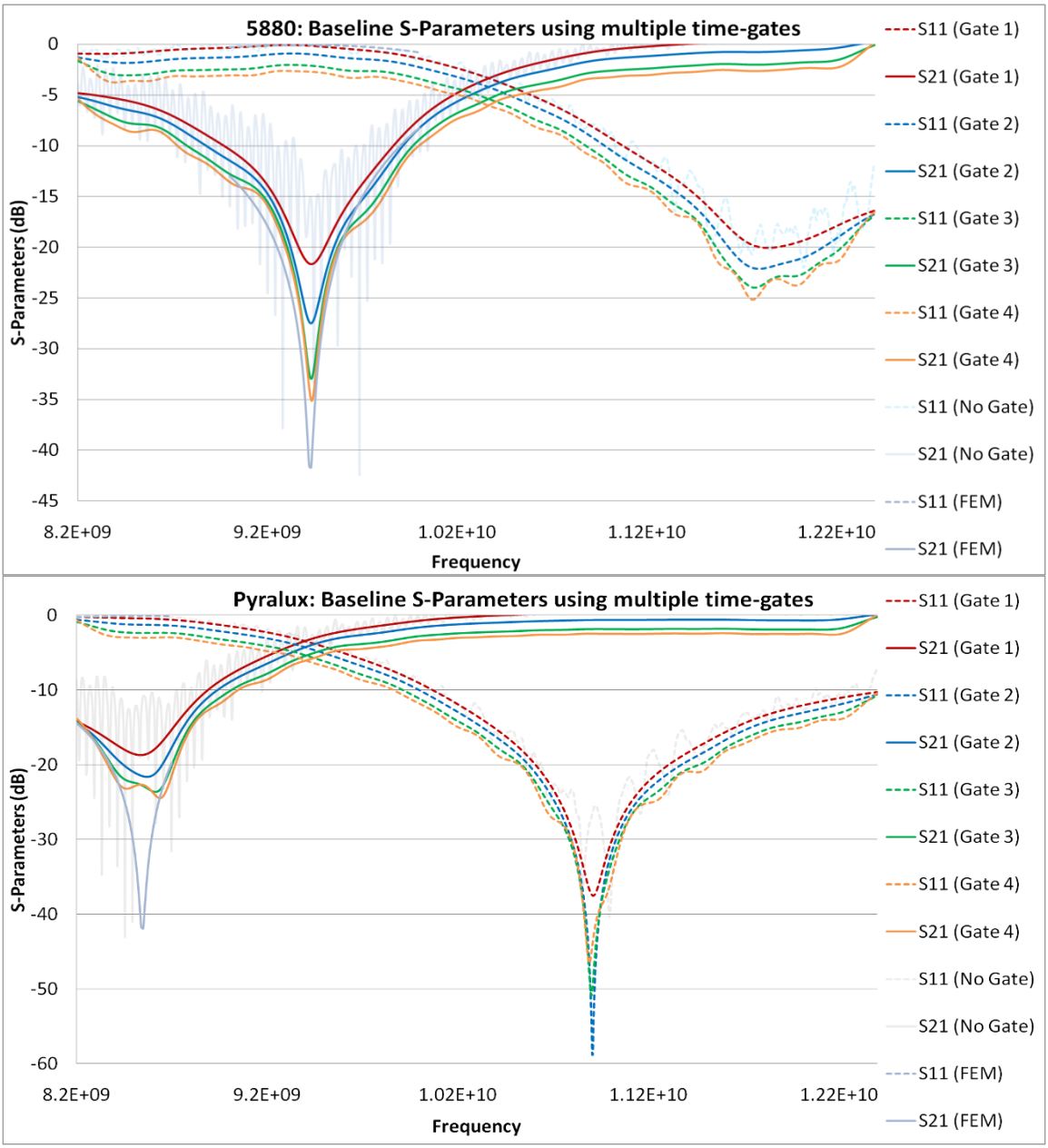

Figure 39. *Experimental baseline readings on a 5880 and Pyralux sample, showing a number of timegates. As the graphs demonstrate, an increase in the window for data collection allows improved capture of the resonant response, but at the expense of also capturing additional spurious reflections from the test facility. The response with no time gating is shown for reference. Also shown are numerical simulation results (FEM in COMSOL). The simulated frequency range was truncated to focus on the resonance, in an effort to reduce computation time.*

After RF characterization, a precision scale (ruler) was attached to the front of the sample (provided a length reference for the photogrammetry) and a number of pictures were taken, from a variety of angles, in order to determine the baseline geometry of the sample. Figure 40 contains two pictures taken during this effort.

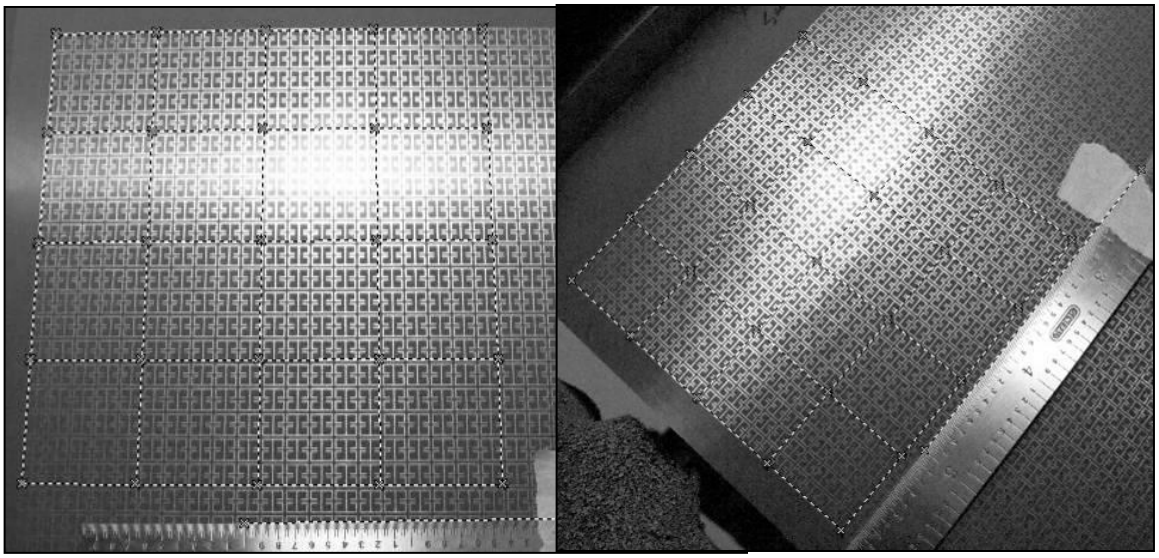

Figure 40. *Pictures of the metamaterial surface for strain-mapping via photogrammetry. Photographs were taken from a variety of angles in accordance with best practices [74]. Included in both pictures is the ruler used to provide a length reference*

After collecting data on the baseline RF performance and geometry, tensile loading was applied to the metamaterial sample. The loadframe was controlled via Bluehill2 version 2.9 [68] software, and utilized several programmed hold points during the loading profile. Once the loadframe hit a pre-determined load level, a "hold" was initiated to maintain a constant cross-head displacement/strain level. The sample was allowed to stress-relieve for 2-3 minutes (depending upon material) to ensure the unit cell geometry was stable at the new displacement level.

Figure 41 shows the load history from one of the tests. The curve demonstrates significant stress-relief in the metamaterial sample.

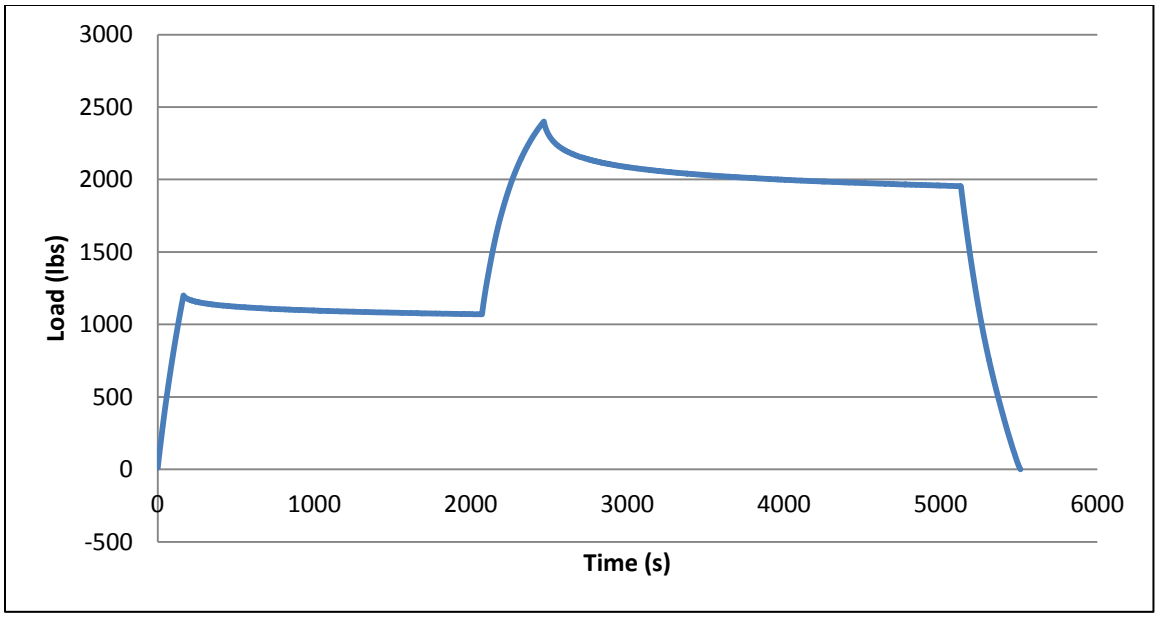

Figure 41. *Typical load/time curve from one of the Pyralux sample tests. The graph demonstrates significant stress relief in the samples during each of the programmed holds (i.e. mechanical loadframe crosshead maintains constant position). RF characterization and photography from strain mapping were performed after the load had stabilized during one of the hold periods.*

Once the load level had attained a near steady state, RF characterization was performed at the deformed geometry, the scale/ruler re-applied, and pictures taken for assessing the sample's strain profile at the loaded/deformed geometry. The "hold" on the loadframe control was ended, and the process (load the specimen to the next programmed hold, allow material stress-relieving to settle, perform RF characterization, take photographs) was repeated for each "hold" position delineated in the control scheme.

2.4.3.2.3 Results

To correlate the COMSOL model predictions with the results, it was necessary to determine the strain profile (E_{XX} and E_{YY} values) of the metamaterial sample. Photomodeler version 6 [74] software was utilized to integrate 10-12 photographs at each load increment and determine the spacing between the points denoted in Figure 40. That

large number of photographs over-defined the geometry, but improved the precision of the generated geometric solution. Assessing the strain in the loaded sample was then distilled to determining the change in length between points. Multiple examination distances were recorded to a) ensure a consistent strain field over the center of the metamaterial sample, and b) provide better statistics for the strain values and the resultant shift in resonant frequency.

Table 4 details the strains that were ascertained via photogrammetry (given as a range of values). The values were input into Eqs. {25} to determine the software predicted shift (Δf_{ave}) in the metamaterial's resonant frequency. This is also given in Table 4, along with the standard deviation in the predictions, and the results from the free-space EM characterization. As the table shows, the predictions are in agreement with the tests. This agreement is noteworthy, due to the numerous sources of errors in the process: mechanical properties and the approximation as a linear trend, dimensional tolerances of the sample, numerical analysis, the onset of plasticity in the samples, the photogrammetric determination of the strain values, and the accumulation of multiple round-off errors.

Table 4 also demonstrates how the different materials exhibit disparate EM responses when subjected to similar loading scenarios. Applying a Y-directed load to the Pyralux samples generated a decrease in the resonant frequency, while the same load input generated an increase in the resonant frequency of the 5880 samples. As Figure 37 shows, both materials exhibit similar sensitivities to each of the strain components (E_{XX} and E_{YY}). However, Figure 35 and Figure 36 show that the substrate materials exhibit significantly different Poisson's ratios ($-E_{XX}/E_{YY}$: 0.4 for the 5880 and 0.25 for the

Pyralux), so the same externally applied load/strain results in different strain values in the orthogonal direction. When these strain profiles are input into Eqs. {25}, they lead to predicted shifts in opposing directions.

	Pyralux, ½oz Cu, Sample 1, 2400 lbs	Pyralux, ½oz Cu, Sample 2, 2400 lbs	Pyralux, 1oz Cu, Sample 1, 2400 lbs	Pyralux, 1oz Cu, Sample 2, 2400 lbs	5880, Sample 1, 1200 lbs	5880, Sample 1, 1600 lbs	5880, Sample 2, 1250 lbs
E_{XX} (%)	-1.12 to -1.06	-1.12 to -0.99	-1.25 to -1.19	-1.12 to -1.06	-0.73 to -0.59	-1.26 to -0.99	-0.79 to -0.66
E_{YY} (%)	4.16 to 4.3	4.03 to 4.1	3.76 to 3.96	4.03 to 4.1	1.10 to 1.14	1.83 to 1.87	1.10 to 1.14
Predicted Δf_0 (GHz)	**-0.032**	**-0.030**	**-0.020**	**-0.029**	**+0.009**	**+0.018**	**+0.012**
StDev Δf_0 (GHz)	0.002	0.003	0.002	0.001	0.006	0.003	0.003
Test Results (GHz)	**-0.039**	**-0.032**	**-0.026**	**-0.029**	**+0.011**	**+0.018**	**+0.013**

Table 4. *Comparison of the predicted shift in the resonant frequency and the empirical results. Also shown are the strain values determined via Photogrammetry, which are required to determine the predicted shift.*

Figure 42 shows the S21 values retrieved during a test on one of the samples. Of note is the decrease in the strength of the resonant response when the sample is loaded. Unlike standard "dog-bone" tensile specimens [66], which provide consistent levels of stress and strain throughout the test section, the edges of the metamaterial sample (which had a thin and wide configuration) display significant deviations from the strain profile at the center of the sample. While the majority of the EM energy does interact with the center of the metamaterial sample, the non-uniformity in the strain profile effectively spreads the spectrum of the response (because unit cells with different strain profiles resonate at different frequencies) and decreases the strength of the sample's resonant response. Other efforts experimentally demonstrated this phenomenon [28][29], but did not detail the underlying physical mechanisms.

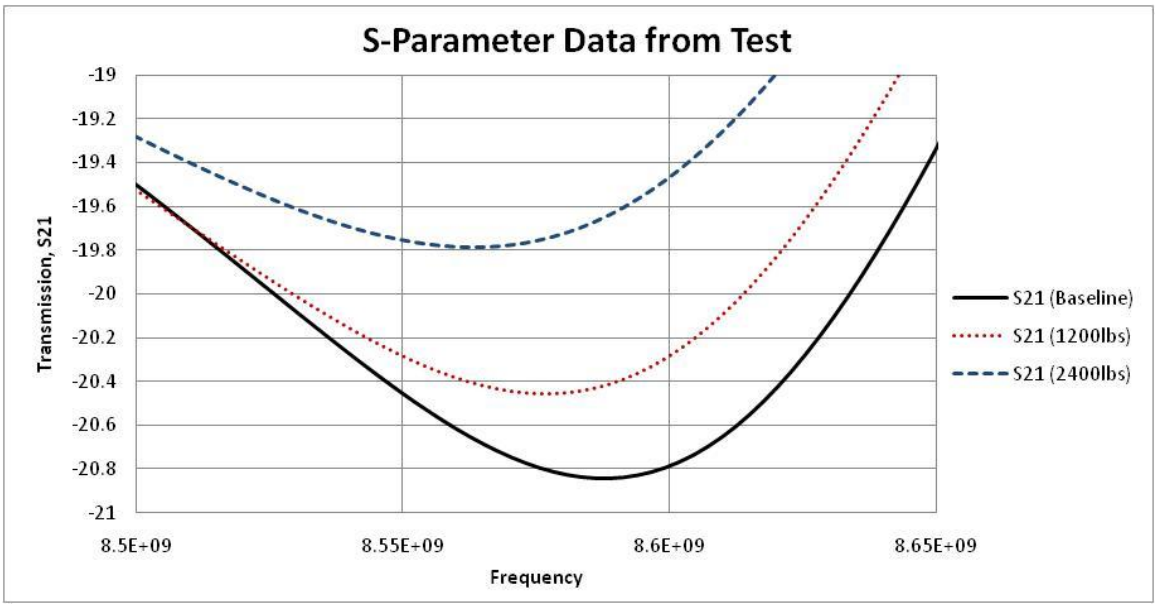

Figure 42. *Data set from one metamaterial sample (Pyralux, 1oz, #1). The loads shown refer to the loadframe hold points at which the data was taken. Typical of the results from the testing conducted during this effort, the figure demonstrates: a) the strain-dependent shift in the resonant frequency, and b) spreading of the spectral response and c) a decrease in the resonant strength, at load.*

2.4.4 Conclusions

This section demonstrates that the substrate's modulus plays a significant role in the strain-dependent electromagnetic performance of metamaterial structures. Depending upon the relative thickness and modulus of the constituent materials, the metamaterial can exhibit dramatically different strain-dependent responses when subjected to mechanical loading. Shear-lag models were utilized to describe load transfer from the dielectric substrate into the conductive traces on the surface of the substrate, and how load transfer changes as a function of substrate modulus. Equivalent circuit parameters are leveraged to explain how the different strain values in the substrate and conductive traces translate into changes in the metamaterial's resonant frequency. Multiphysics modeling is then utilized to predict the relationship between mechanical strain, material moduli, and electromagnetic performance. To validate these models, a unique test

facility at Duke University was established to generate empirical data on the EM performance of mechanically-loaded metamaterial samples.

In order to successfully transition metamaterials onto operational systems, these relationships must be understood to enable predictions of EM performance in a relevant environment. Additionally, developing a better understanding of the intimate linkage between mechanical properties and EM performance will allow engineers to more intelligently design and perform multi-dimensional optimization of these unique multifunctional structures.

3 METAMATERIAL TEMPERATURE-DEPENDENCE

Section 2 details processes used to understand and predict metamaterial strain-dependent electromagnetic response. These processes are now leveraged and expanded to fully describe metamaterial temperature-dependence. The analysis in this section returns to the assumption of a stiff substrate, as utilized in Sections 2.2 and 2.3.

3.1 TEMPERATURE DEPENDENCIES

As in [32], the temperature-dependence of the metamaterial is attributed to three primary causes:

1) Thermally-induced strains
2) Temperature-dependence of the substrate permittivity
3) Temperature-dependent conductivity of the copper

As detailed in [22] and Section 2.3, the ELC's permittivity and permeability can be approximated via the following analytic expressions

$$\varepsilon = \bar{\varepsilon}\frac{\frac{\theta d}{2}}{\sin\frac{\theta d}{2}cos\frac{\theta d}{2}} \qquad \{26\}$$

$$\mu = \frac{\frac{\theta d}{2}}{\sin\frac{\theta d}{2}}cos\frac{\theta d}{2}.$$

where d is the length of the unit cell and θ is the propagation constant ($\theta = n_{eff}\frac{\omega}{c}$), computed from the numerical simulation. As stated previously, Eqs. {26} are valid for a

metamaterial that has a predominantly electric resonant response; $\bar{\varepsilon}$ represents the relative homogenized permittivity in the absence of spatial dispersion, with the remaining terms accounting for the finite phase advance of the wave across the unit cell. Note that while there is no magnetic response expected, spatial dispersion creates an effective relative permeability described by the second of Eqs. {26}.

Typically, Eqs. {26} would be used to confirm the retrieved parameters obtained from numerical simulations. However, if an analytic form is known for the homogenized permittivity, then Eqs. {26} can be applied to find an analytical expression for the metamaterial unit cell. As in Section 2.3, by using the equivalent circuit model shown in Figure 16 for the ELC, along with known analytical expressions for the circuit parameters, an approximate analytical form for the effective permittivity of a thin ELC layer ($\bar{\varepsilon}$) can be obtained

$$\bar{\varepsilon} = \varepsilon_b + \frac{C_{ext}}{d\varepsilon_0} \frac{\omega_0^2 - \omega^2}{\omega_0^2 - \omega^2\left(1 + \frac{C_{ext}}{C_{\text{int}}}\right)} \qquad \{12\}$$

Where

$$\omega_0^2 = \frac{1}{LC_{\text{int}}} \text{ and } L \to L + \frac{R}{i\omega}.$$

For this study, ε_b is equal to 1.495 (not 1) at the reference condition, due to the non-negligible thickness of the substrate. It should be noted that if the exact expressions are used for the circuit parameters in Eq. {12}, the effect of interactions between elements is effectively neglected. The generic resonant form of Eq. {12}, however, is flexible enough that the basic behavior of the ELC medium can be predicted and

extrapolated using the quasi-analytic expressions that incorporate the ELC geometry, as will be shown.

Adding to Eqs. {26} and {12} the dispersion relation [22]

$$\sin\frac{\theta d}{2} = \sqrt{\bar{\varepsilon}}\,\frac{kd}{2}\ , \qquad \{15\}$$

it again becomes apparent that describing a metamaterial's strain- and temperature-dependence can be distilled to understanding the strain- and temperature-dependence of the four equivalent circuit elements; C_{int}, C_{ext}, L, and R.

For the unit cell depicted in Figure 13, the following values for the circuit elements provide strong agreement (depicted in Figure 43) between the simulation (performed in HFSS™) and analytic expressions: C_{int}=2.94*10^{-14} F, C_{ext}=4.84*10^{-14} F, L=3.74*10^{-9} H, and R=0.74 Ω.

Following the process of Sections 2.2 and 2.3, analytic expressions are leveraged to describe the changes in the equivalent circuit parameters of Eq. {12} when the metamaterial is subjected to an operational environment (i.e. mechanical loading and/or temperature changes). Provided again for clarity, the capacitance (C) for a co-planar capacitor can be approximated as [51]

$$\begin{aligned} C &= C_a + C_s \\ C_a &= \varepsilon_0 \frac{2}{\pi}\ln\left(2\beta\frac{H}{s}\right)W \\ C_s &= \varepsilon_0 \frac{\varepsilon_s - 1}{\frac{s}{h_s} + \frac{4}{\pi}\ln\beta}W \end{aligned} \qquad \{4\}$$

W, s and H are the geometrical parameters of the ELC, as depicted in Figure 13, the subscripts a and s refer to air/vacuum and substrate, respectively, and β=5/2.

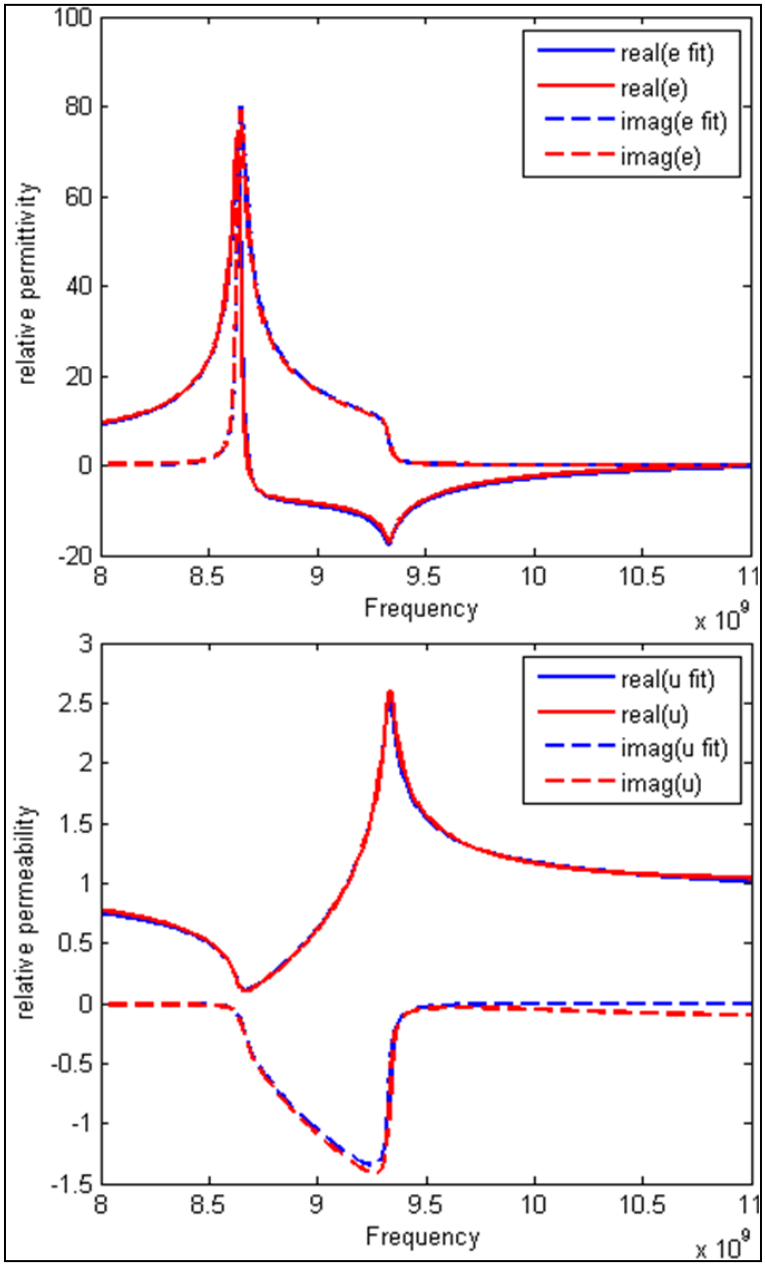

Figure 43. *Analytic (e fit, u fit) vs simulation-derived (e, u) permittivity and permeability curves for the unit cell being studies, in the baseline condition; at the reference temperature with no applied mechanical load [75].*

The self-inductance (L) of a thin, conducting strip can be approximated as [52]

$$L = \frac{\mu_0 l}{2\pi}\left[\ln\left(\frac{2l}{b}\right) + \frac{1}{2} + \frac{b}{3l} - \frac{b^2}{24l^2}\right] \quad \{5\}$$

where l is length and b is the width of the conducting strip.

The resistance of any length of conductor can be approximated by

$$R = \frac{l}{\sigma A} \quad \{13\}$$

Where σ is the conductivity, and l and A the length and cross-sectional area of the conductor (A=$b\delta$, and $\delta = \sqrt{2/\omega_0 \mu \sigma}$).

3.1.1 Thermally-Induced Strains

As before, the metamaterial unit cell is assumed part of a large (>10λ) load-bearing structure. As a result, the copper contributes insignificantly to the stiffness of the composite structure and the in-plane strain profile is assumed uniform across the unit cell (i.e. negligible local stiffening effects from the copper). Similarly, the temperature profile for the unit cell is assumed to be approximately uniform, owing to the gradients in the structure's temperature profile operating over large areas/many unit cells. The process in Section 2.2. was followed to develop a model in HFSS™ [39] capable of accommodating thermal strains and expanded to also include shifts in material properties due to changes in temperature. For the purposes of this effort, a temperature range of -150^0 to +150^0C was used, since it envelops the range of temperatures experienced by many structures in an orbital environment [76].

Eqs. {4-6} are utilized to describe the equivalent circuit parameters of this unit cell as a function of mechanical strain (E_{ij}). As before, these trends are linearized, with minor loss of accuracy, to produce

$$C'_{\text{int}} = C_{\text{int}}\left(1 + E_{XX} - 0.056E_{YY}\right) \quad \{27\}$$

$$C'_{ext} = C_{ext}\left(1 + E_{XX} - 0.042E_{YY}\right)$$

$$L' = L\left(1 + 0.11E_{XX} + 0.89E_{YY}\right)$$

$$R' = R\left(1 - 0.58E_{XX} + 0.58E_{YY}\right)$$

Where the primes denotes the non-reference (mechanically loaded and/or not at the reference temperature) condition and the non-primed values connote the parameter values at the reference condition. Shear strains are neglected, because the analysis of Section 2.2 demonstrated that the metamaterial is over an order of magnitude more sensitive to normal strains.

The relationship between changes in temperature and mechanical strain, for an isotropic material under free thermal expansion/contraction has the form [64]

$$E_{ii}^{T} = \int_{T}^{T'} \alpha(T)dT, i = 1,2,3 \quad \{28\}$$

Where E_{ii}^{T} is the normal, thermally-induced strain component (in this equation, the double indices do not connote summation), T is the reference temperature (chosen to be 25^0C), T' is the current temperature, and α is the material's coefficient of thermal expansion (CTE). Assuming a constant CTE over the range of interest, Eq. {28} reduces to the linear relationship

$$E_{ii}^{T} = \alpha\left(T' - T\right) \quad \{29\}$$

Table 5 shows the CTE values for a number of pertinent materials. Since the focus is on the implementation of metamaterials in operational platforms, it is reasonable to restrict the analysis to linear-elastic mechanical behavior. As a result, the thermally induced strains can be superposed with strains induced via mechanical loading [64] $\left(E_{ij} = E_{ij}^{M} + E_{ij}^{T}, i = 1,2,3,\ j = 1,2,3\right)$ and incorporated into Eqs. {27} to describe the resultant strain-dependent behavior of the metamaterial.

Material	CTE (α)	COε$_r$
Rogers, RT-Duroid-5880 [38]	28ppm/K (X) 41ppm/K (Y) 252ppm/K (Z)	-125ppm/K
Rogers, RT-Duroid-6002 [38]	16ppm/K (X,Y) 24ppm/K (Z)	12ppm/K
PTFE [77]	180-250ppm/K	-960ppm/K
Cross-linked Polystyrene [29]	70ppm/K	-183ppm/K
FR4 [32], [78]	10ppm/K	>2000ppm/K
Copper	17ppm/K	N/A

Table 5. *Coefficient of Thermal Expansion (CTE) and thermal Coefficient of Relative Permittivity (COεr) for a number of pertinent material systems. ppm=parts per million, or 1e-6.*

3.1.2 Temperature-dependent permittivity

As Table 5 shows, many pertinent substrate materials exhibit a temperature dependent permittivity. The COε$_r$ in the table is the thermal coefficient of relative permittivity, and is an electromagnetic analogue to the CTE. The relationship between changes in temperature and permittivity can be expressed as

$$\varepsilon_S' = \int_T^{T'} CO\varepsilon_r(T)dT + \varepsilon_S \qquad \{30\}$$

Where ε'_S is the permittivity at the current temperature and ε_S is the permittivity at the reference temperature. Assuming a constant $CO\varepsilon_r$ through the temperature range of interest, Eq. {30} reduces to the linear relationship

$$\varepsilon'_S = CO\varepsilon_r\left(T' - T\right) + \varepsilon_S \qquad \{31\}$$

Referring back to the equations for the circuit elements, the permittivity of the substrate only plays a role in the capacitances. Eq. {4} provides the following relationship between substrate permittivity and the internal and external capacitance of the unit cell. Again, the trends are linearized, with minor loss of accuracy, resulting in

$$C'_{\text{int}} = C_{\text{int}}\left(0.293\varepsilon'_S + 0.355\right)$$

$$C'_{ext} = C_{ext}\left(0.287\varepsilon'_S + 0.369\right) \qquad \{32\}$$

3.1.3 Temperature-dependent conductivity

The temperature-dependent conductivity of copper can be expressed as

$$\sigma' = \frac{\sigma}{1 + \beta\left(T' - T\right)} \qquad \{33\}$$

where σ is 58e6 Siemens/m at 25^0C and β is 0.004 for copper. Referring to the equations for the circuit elements, conductivity only plays a role in the resistance. However, the resistance change also results in a change in the skin-depth. Utilizing Eq. {13}, as well as the equation for the skin-depth provides the following relationship

$$R' = R\sqrt{\frac{\sigma}{\sigma'}} \qquad \{34\}$$

3.2 TEMPERATURE-DEPENDENT PERMITTIVITY AND PERMEABILITY CURVES

Taking advantage of the apparent linearity of the strain-dependence, as well as the independence of the substrate permittivity and copper conductivity, Eqs. {27, 32, and 34} are combined to produce the following strain- and temperature-dependent relationships for the circuit elements of the ELC

$$C'_{\text{int}} = C_{\text{int}}\left(0.293\varepsilon'_S + 0.355\right)\left(1 + E_{XX} - 0.056E_{YY}\right)$$

$$C'_{ext} = C_{ext}\left(0.287\varepsilon'_S + 0.369\right)\left(1 + E_{XX} - 0.042E_{YY}\right)$$

$$L' = L\left(1 + 0.11E_{XX} + 0.89E_{YY}\right)$$

$$R' = R\left(\sqrt{\sigma/\sigma'}\right)\left(1 - 0.58E_{XX} + 0.58E_{YY}\right) \qquad \{35\}$$

Incorporating the relationships in Eqs. {29 and 31} into the capacitance equations of Eqs. {35}, indicates that the greatest change in capacitance occurs when CTE and $CO\varepsilon_r$ are of the same sign. Conversely, when they are of opposite sign, they tend to negate the effects of one another.

The inductance equation of Eqs. {35} shows that it is purely strain-dependent, and not a function of material properties. The resistance equation shows nearly the opposite effect (for the unit cell of Figure 13, invoking the assumptions of isotropy and free thermal expansion results in no strain-dependence in the resistance).

An important observation from the relationships of Eqs. {35} is that sound engineering practices may be employed to mitigate a metamaterial's temperature-dependence; or conversely, to enhance it. Utilizing materials with low values of CTE (α) and $CO\varepsilon_r$ can lead to near negligible changes in the metamaterial's inductance and

capacitances; further reduction of the capacitance changes are possible if α and $CO\varepsilon_r$ are also of opposite sign. As for the resistance, it is an unfortunate fact that good conductors tend to exhibit strong temperature-dependent conductivities. Improving the thermal stability of this factor likely requires a trade with increased ohmic losses.

To demonstrate the dynamic range of the analytic expressions, the following analysis utilizes large values for the CTE (60 ppm/K, a reasonable value for many polymeric substrates) and $CO\varepsilon_r$ (960ppm/K, same sensitivity as PTFE, but with positive sign), as well as the temperature-dependent conductivity of copper. Eqs. {29, 32, and 33} were used to determine the material property values at -150 and +150 ^{0}C, which are shown in Table 6.

	-150^{0}C	**+150^{0}C**
$\acute{\varepsilon}_s$	2.032	2.32
$\acute{\sigma}$ (Siemens/m)	1.93e^9	3.87e^7
E_{XX}, E_{YY}, E_{ZZ}	-0.0105	0.0075
E_{ZZC} (Cu thickness)	0.0048	-0.0034

Table 6. *Strain and material properties at -150 and +150 ^{0}C, utilizing the following values: ε_S=2.2, α=60ppm/K, $CO\varepsilon_r$=9.6e^{-4}/K, σ=58e^{6}Siemens/m, and β=0.004*

The analysis assumes linear-elastic, isotropic materials, subjected to free thermal expansion, with constant CTE (α) and $CO\varepsilon_r$ throughout the temperature range. However, the process described in this paper is general, and able to accommodate anisotropy, non-linearity, more complicated material models, and/or combined mechanical and thermal loading. These complexities merely imply additional computational burden to arrive at the strain and material property values that serve as input into Eqs. {35}. The temperature-dependent strain and material property values from Table 6 can then be

incorporated into Eqs. {35} to provide the equivalent circuit parameters at the temperatures of interest; shown in Table 7.

	-150^{0}C	**+150^{0}C**
$\acute{C}_{int}$	0.942C_{int}	1.042C_{int}
$\acute{C}_{ext}$	0.942C_{ext}	1.043C_{ext}
$\acute{L}$	0.990L	1.008L
$\acute{R}$	0.301R	1.499R
$\acute{\varepsilon}_b$	1.426	1.544

Table 7. *Equivalent circuit parameters at -150 and +150 ^{0}C, utilizing the strain and material property values from Table 6.*

The values from Table 7 are incorporated into Eqs. {12}, to solve for $\theta d/2$ in Eq. {15}, and then both parts are incorporated into Eqs. {8} to determine the effective permittivity and permeability of the metamaterial. Figure 44 shows the analytic expressions for the permittivity compared to the results of the full-wave simulations. The figure demonstrates the high level of agreement, over a wide temperature-range, even when modeling materials with a high degree of temperature-sensitivity.

To understand the metamaterial's temperature-dependence, it is often useful to break that dependence down into its constituent parts. Figure 45, Figure 46, and Figure 47 show the permittivity, when the changes in capacitances, inductance, and resistance, respectively, are introduced independent of each other. In the figures, the black curves show the full temperature-dependent response, and the blue (cold/-150^{0}C) and red (hot/+150^{0}C) curves show the effects when only a subset of the circuit parameters are considered.

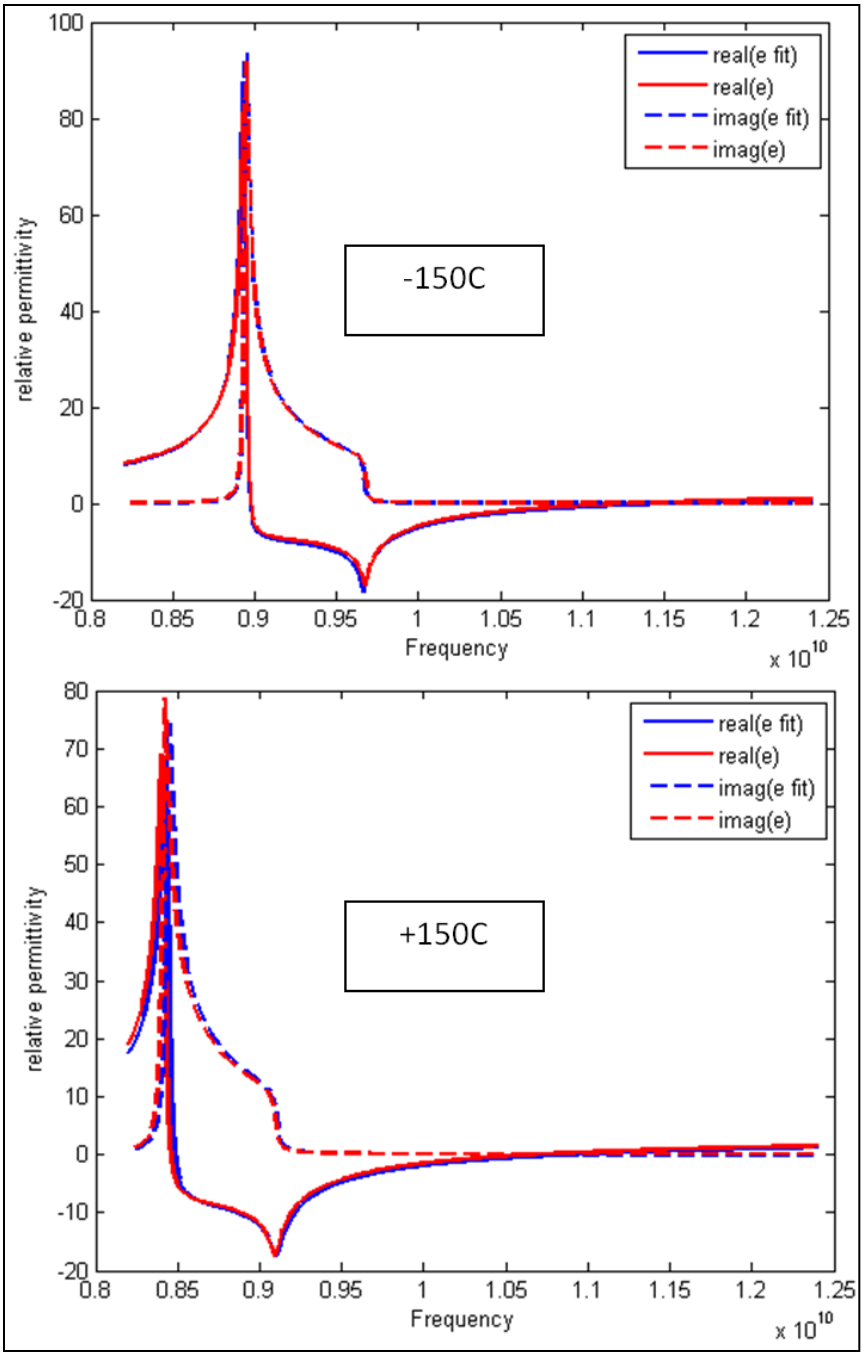

Figure 44. *Temperature-dependent analytic expression of the permittivity (e_fit) compared to full-wave simulations (e). The two graphs demonstrate strong agreement, over a wide temperature range, even when exaggerated temperature-sensitivities in the material properties are used.*

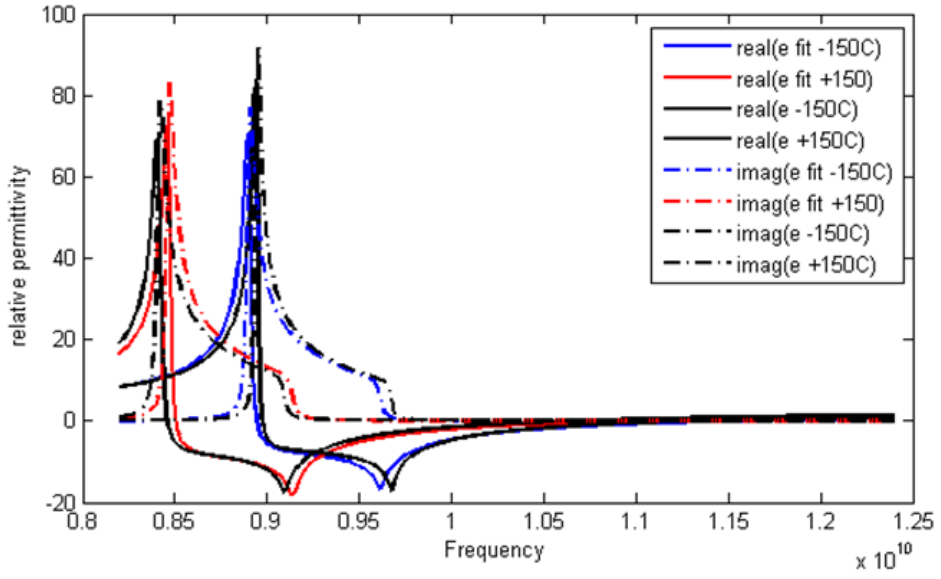

Figure 45. *Temperature-dependent analytic expression of the permittivity (e_fit), compared to the results from the full-wave simulation (e), at +/-150C. The analytic expressions only account for the temperature-dependence of the capacitances. Inductance and resistance are held constant.*

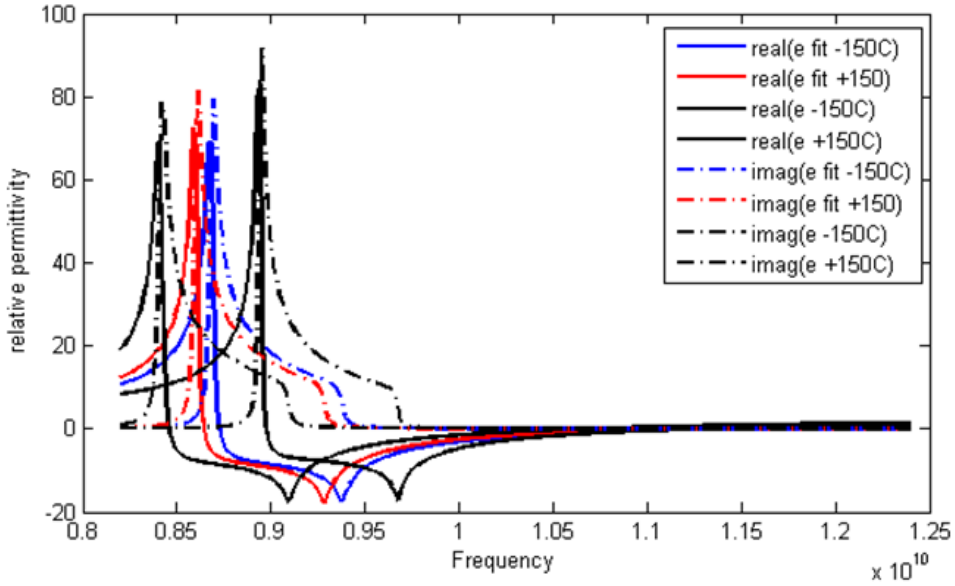

Figure 46. *Temperature-dependent analytic expression of the permittivity (e_fit), compared to the results from the full-wave simulation (e), at +/-150C. The analytic expressions only account for the temperature-dependence of the inductance. Capacitances and resistance are held constant.*

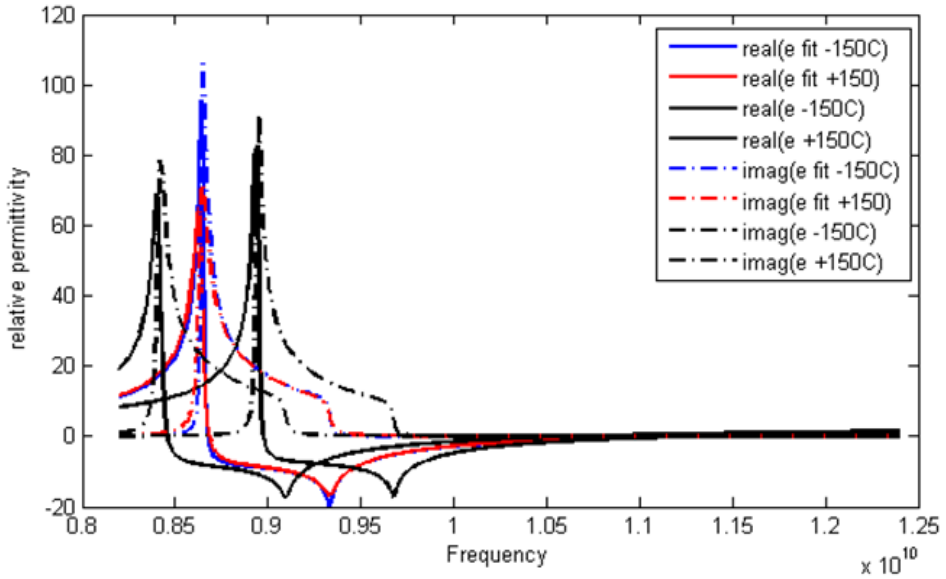

Figure 47. *Temperature-dependent analytic expression of the permittivity (e_fit), compared to the results from the full-wave simulation (e), at +/-150C. The analytic expressions only account for the temperature-dependence of the resistance. Capacitances and inductance are held constant.*

As the figures demonstrate, the capacitive change dominates the temperature-sensitivity, in large part because $CO\varepsilon_r$ is over an order of magnitude larger than the CTE. However, the inductive changes due to thermal strains have to be included to properly account for the full shift in resonance, due to the change in temperature. On the other hand, the resistance change does not induce a frequency shift in the response, but does allow the analytic expressions to reflect the respective strength of response at the different temperatures.

The use of analytic expressions also enables the description of the constitutive parameters continuously throughout the temperature range of interest. Figure 48 are surface plots depicting the temperature dependence of the real part of the permittivity, while Figure 49 shows the temperature dependence of the real part of the permeability. Similar processes can be utilized to describe the imaginary portions of both properties.

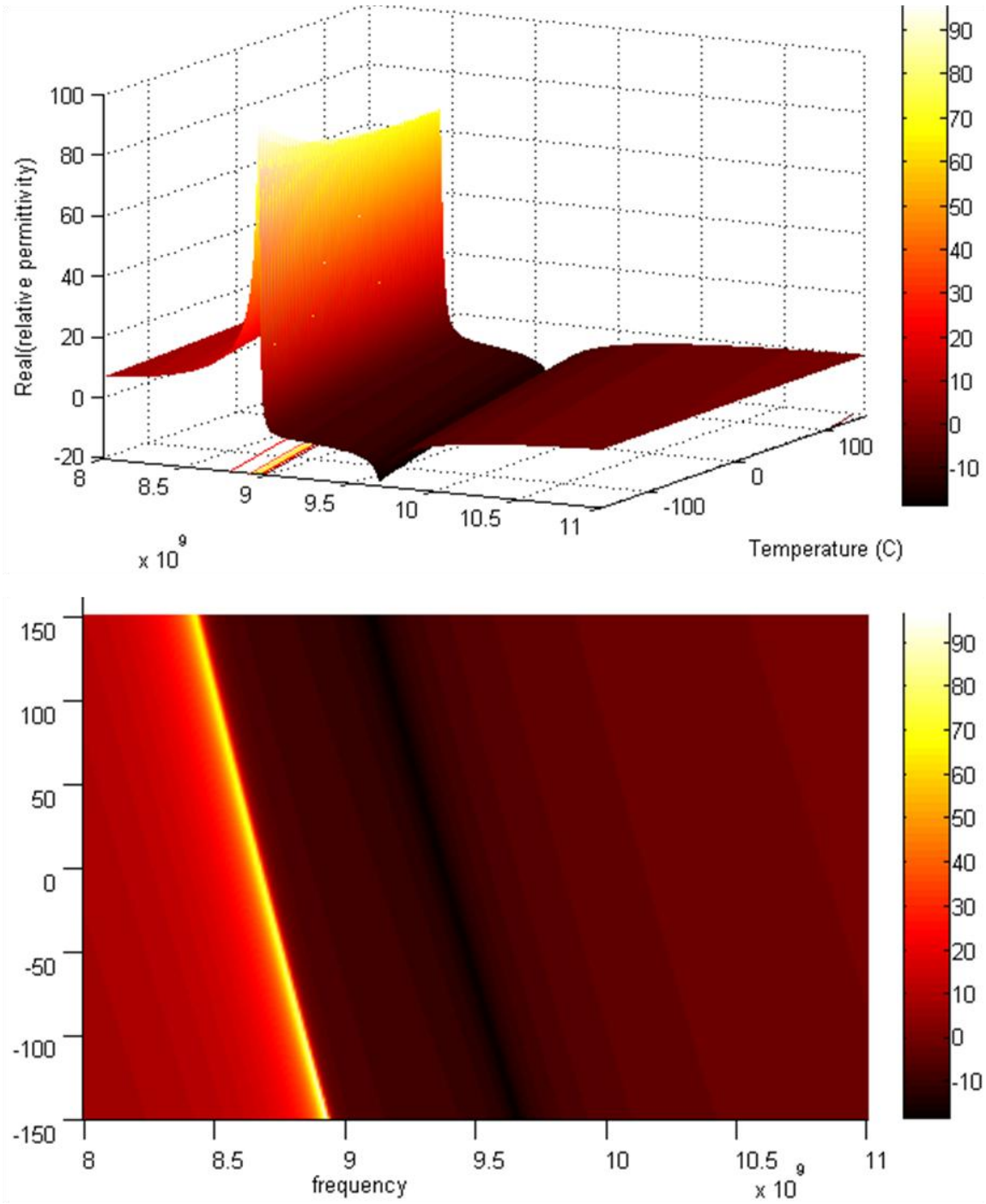

Figure 48. *3- and 2-D contour plots depicting the temperature-dependent real part of the permittivity. The expressions assume free thermal expansion/contraction and the following materials parameters:* ε_S*=2.2,* α*=60ppm/K, CO*ε_r*=9.6e*$^{-4}$*/K,* σ*=58e*^{6}*Siemens/m, and* β*=0.004.*

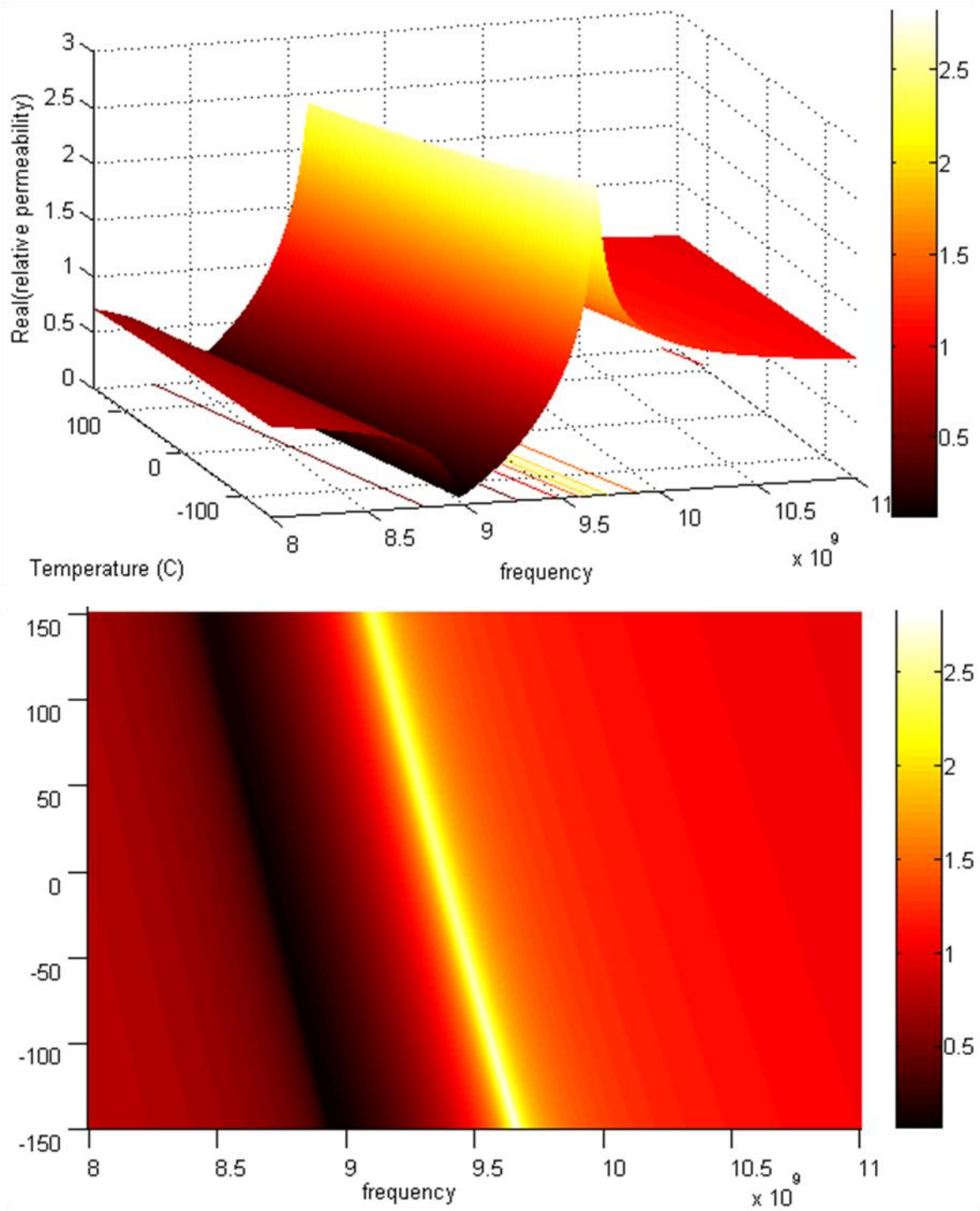

Figure 49. *3- and 2-D contour plots depicting the temperature-dependent real part of the permeability. The expressions assume free thermal expansion/contraction and the following materials parameters:* ε_S*=2.2,* α*=60ppm/K, CO*ε_r*=9.6e*$^{-4}$*/K,* σ*=58e*^{6}*Siemens/m, and* β*=0.004.*

3.3 EXTENSION TO MAGNETIC METAMATERIALS

To expand upon a point made at the conclusion of Section 2.3., the author believes similar processes can be utilized to successfully describe the strain- and temperature-dependent permittivity and permeability of magnetic metamaterials, owing to similar equivalent circuit parameters and analytic expressions for their constitutive properties.

A recent publication by Varadan and Ji [32] provided empirical data and a quantitative description of the temperature-dependent resonant frequency of metamaterial sample composed of Split-Ring-Resonators (SRRs). In [32] a low-temperature co-fired ceramic substrate's real part of the permittivity changed from 7.36 at room temperature (20^0C) to 7.88 at 400^0C. Incorporating that unit cell's geometry into Eqs. {4}, results in the following linearized function: $C'_{\text{int}} = 0.115\varepsilon'_S + 0.154$. Since the room temperature resonance is 10.3 GHz, the relationship $\omega_0^2 = 1/L_S C_S$ [43] can be utilized via the process in Section 2.2 to predict a resonance of 10.0 GHz at 400^0C, closely matching the actual value of ~9.95 GHz. However, the match is not exact because the analysis does not yet include the effects of thermal strain, which, as stated above and in [32], contributes to the shift in resonance.

The above analysis provides much poorer agreement with the FR4 data from [32]. Utilizing Eqs. {4} with the above process predicts a shift in resonance from 10.13 GHz at room temperature $\left(\varepsilon_s = 4.33\right)$ to 9.97 GHz at 90^0C $\left(\varepsilon'_S = 4.51\right)$, while the actual value was 10.03 GHz at 90^0C [32]. Eqs. {4} neglect the polarization of the material on the posterior (non-metalized) side of the substrate to calculate capacitance. However, the FR4 is relatively thin, with a lower dielectric constant; neglecting this term on this

sample overestimates the change in capacitance and the resonant frequency [79]. An alternative expression for the capacitance of coplanar strips that captures the fields on the posterior side of the side of the metamaterial is given by [80]

$$C = C_a + C_s + C_P$$

$$C_a = \varepsilon_0 \frac{2}{\pi} \ln\left(2\beta \frac{H}{s}\right) W$$

$$C_s = \varepsilon_0 \frac{\varepsilon_s}{\frac{s}{h_s} + \frac{4}{\pi} \ln \beta} W$$

$$C_p = \varepsilon_0 \frac{1}{\pi} \ln\left(2\beta \frac{H}{s}\right) W$$

Where the parameters are the same as those utilized in Eqs. {4}, and the subscript *p* refers to the posterior side of the sample. Utilizing this expression results in the following linearized function $C'_{\text{int}} = 0.1276\varepsilon'_S + 0.4474$, which leads to a predicted resonance of 10.02 GHz at 90^0C; providing much better agreement with the actual value of 10.03 GHz.

Analytically describing the strain- and temperature-dependent permittivity and permeability of magnetic metamaterials will require the development of a $\bar{\mu}$ analogue to Eq. {12}, which can be found in [22]. Additionally, an alternative form of the self-inductance (L) expression, which includes the loop inductance (such as the form found in [81]) must be utilized.

3.4 CONCLUSIONS

This section demonstrates that equivalent circuit elements and relatively simple analytic expressions for their parameters can be used to accurately predict a metamaterial's temperature-dependent constitutive properties (ε and μ). Additionally, the apparent linearity of the trends, over ranges pertinent for most mechanical systems, allows the prediction of those constitutive properties for arbitrary combinations of temperature and strain.

The expressions for a metamaterial's circuit parameters are straightforward functions of geometry and material properties. They are, therefore, easily modified to accommodate mechanical strain (by definition, a small change in geometry) as well as changes in those material properties brought about by a change in temperature.

While standard numerical techniques can be used to model metamaterial strain- and temperature-dependence, analytic expressions provide a number of unique benefits:

1. Analytic expressions can be leveraged to *rapidly* predict the unique strain- and temperature-dependent constitutive properties of a wide range of unit cell designs that share a common equivalent circuit model.
2. Analytic expressions describe the behavior over the continuum of strains and temperatures of interest, whereas numerical techniques provide discrete sets of results for the conditions explicitly modeled.
3. As a result, the use of analytic expressions enable the efficient determination of the EM performance of large structures, with multiple unit cell designs, subjected to complex strain and temperature profiles.

It is also believed that similar analytic processes can be utilized to describe the strain- and temperature-dependent behavior of magnetic metamaterial resonators, owing to similar circuit models and analytic expressions for their constitutive properties.

4 CONCLUSIONS AND RECOMMENDATIONS FOR FUTURE WORK

4.1 CONCLUSIONS

This research sought to develop an understanding of the physical mechanisms that drive metamaterial strain- and temperature-dependence. By understanding the physical mechanisms, one can develop processes that enable quantifiable and accurate predictions of those interdependencies. As stated multiple times within this document, this understanding, and the ability to predict metamaterial behavior in an operational environment, are critical for transitioning this technology from laboratory novelty to fielded capability.

This research demonstrates that equivalent circuit models can be extremely powerful tools for understanding and quantifying metamaterial strain- and temperature-dependence. By leveraging relatively simple analytic expressions for a metamaterial's equivalent circuit parameters, one can quickly predict a metamaterial's strain- and temperature-dependent behavior and EM constitutive material parameters.

As stated in the introduction, while standard numerical techniques can be used to model metamaterial strain- and temperature-dependence, analytic expressions provide a number of unique benefits:

1. Analytic expressions can be leveraged to rapidly predict the unique strain- and temperature-dependent constitutive properties of a wide range of unit cell designs that share a common equivalent circuit model.

2. Analytic expressions describe the behavior over the continuum of strains and temperatures of interest, whereas numerical techniques provide discrete sets of results for the conditions explicitly modeled.
3. Analytic expressions for metamaterial constitutive properties enable the use of continuum approaches for EM modeling. The use of continuum approaches, as opposed to directly solving interactions with a metamaterial's complex geometry, reduces model size by at least five orders of magnitude.
4. As a result, the use of analytic expressions are absolutely crucial for the efficient determination of the EM performance of large structures, with multiple unit cell designs, subjected to complicated strain and temperature profiles.

Additionally, the use of analytic expressions provide insight into the mechanisms that drive metamaterial strain- and temperature-dependence. Similar insight is not afforded via multiphysics numerical modeling.

In Section 2.2, expressions for inductance and capacitance are utilized to accurately predict the metamaterial's strain-dependent resonant frequency. The expressions for the metamaterial's equivalent circuit parameters are straight-forward functions of geometry; thus strain (a change in geometry) is easily accommodated within the expressions. Additionally, the resonance is a critical parameter in many metamaterial designs and provides an important data point for describing and understanding the structure's effective medium properties. Section 2.4 leveraged that understanding to describe the strain-dependent resonant frequency of metamaterials constructed on soft/low modulus substrates. Simple shear-lag models and multiphysics modeling were

utilized to describe the role that substrate modulus plays in the strain-dependence of the metamaterial's inductance and capacitances.

Section 2.3 expanded upon the analysis of 2.2 by including an expression for Ohmic resistance, as well as a new analytic expression for the effective permittivity of the thin-ELC layer ($\bar{\varepsilon}'$), within the metamaterial cubic lattice. This enabled prediction of the metamaterial's strain dependent permittivity and permeability curves, while accommodating spatial dispersion and losses. A metamaterial's effective constitutive properties (ε and μ) are the key parameters that enable efficient EM modeling of large and/or complex metamaterial structures.

Section 3 leveraged the equivalent circuit expressions from Sections 2.2 and 2.3 to describe the metamaterial's temperature-dependent constitutive material properties. Temperature-dependence was broken into three primary causes: thermally driven strains, and temperature-dependent permittivity and conductivity. The previous sections demonstrated the expressions' ability to accommodate strain. Those same expressions also accommodated the pertinent temperature-dependent material properties, enabling accurate prediction of the metamaterial's temperature-dependent permittivity and permeability.

Although not explicitly stated in the previous sections, these expressions demonstrate a high degree of flexibility to changes in metamaterial configuration. Referring to Figure 13, the parameters "s," and "W," and the substrate's permittivity were varied by up to +/-20% with little loss of accuracy between the analytic descriptions and numerical simulations. Many of the more famous metamaterial designs [11][13][14] utilize unit cells of the same design family, but with minor changes in critical dimensions,

to deliver point-wise control of the EM constitutive properties throughout the volume of a structure. These expressions allow the designer to efficiently ascertain the strain- and temperature-dependence of the entire family of unit cell designs utilized in a complex metamaterial structure.

However, caution must be observed in determining which analytic expressions to utilize to describe metamaterial strain- and temperature-dependence. As described in Section 3, the thickness of the substrate (as well as its permittivity) will drive whether or not one has to consider the fields on the posterior (non-metallized) side of the unit cell when calculating capacitance. In [79], Chaim, et al., also demonstrated the EM performance of a metamaterial constructed on a thin substrate is very sensitive to the dielectric constant of the material placed on the posterior (non-metallized) side of the sample. That sensitivity diminishes as the substrate increased in thickness.

4.1.1 The Case Against Direct Solution

One may pose an argument against utilizing a continuum-based approach and effective constitutive parameters when modeling complex metamaterial structures. The claim is that recent advances in computing allow modeling these highly complex structures directly. The experiences and lessons detailed in this document refute those claims. The models developed to accurately describe metamaterial strain- and temperature-dependence, at the unit cell level, required between 100,000 to 300,000 tetrahedra; even though these models utilized symmetric or periodic boundary conditions and truncated waveguides in order to reduce model complexity. Many envisioned applications require millions of unit cells, with tens of thousands of unique cell designs. Attempting to capture this complexity, in a relevant loading environment, is intractable

via direct solution. Just as in mechanics, metamaterials require the use of effective constitutive parameters to effectively and efficiently model these complex structures, especially when the engineer must consider time-variant loading scenarios.

4.1.2 Modeling EM Performance of Complex, Mechanically-Loaded Metamaterial Structures

To understand how an engineer could implement the process detailed in this dissertation, reconsider the composite flat-plate lens from Section 1.1 (Figure 50). This metamaterial structure utilizes a radially-varying index of refraction in order to focus microwaves. The high-modulus glass-fiber composite structure is designed to incorporate both load-bearing and advantageous EM capabilities.

To model the baseline/unloaded behavior of the lens, standard practice dictates that the engineer must first understand the EM behavior (S-parameters, resonance, permittivity and permeability curves, index of refraction, wave impedance) of each unique unit cell design, and their placement within the lens [11].

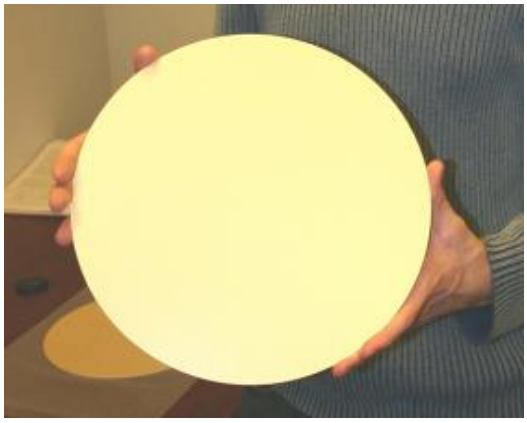

Figure 50. *Flat-plate microwave lens. Lensing is enabled through a radially-varying index of refraction [11].*

Given these baseline properties, simple scripts (via software tools such as MatLab) can determine $\bar{\varepsilon}$, $\theta d/2$, and the magnitude of the equivalent circuit parameters (inductances, capacitances, resistances). Analytic expressions can then rapidly ascertain the strain- and temperature-dependence of the equivalent circuit parameters, for each of the unique unit cell designs in the metamaterial structure.

Utilizing standard mechanical FEM packages (ANSYS [39], COMSOL [57], etc.), an engineer can determine the strain fields and temperature profile throughout the lens structure for a given loading scenario. These can then be used to establish the new circuit parameters, $\bar{\varepsilon}$, $\theta d/2$, and the EM constitutive properties (ε and μ). These values of ε and μ are then incorporated directly into the EM model to assess how the mechanical and/or thermal loads alter image quality (change in focal length, aberrations, etc.). The power of the technique proposed in this dissertation is shown in Figure 51, which provides a graphical depiction of the proposed process flow.

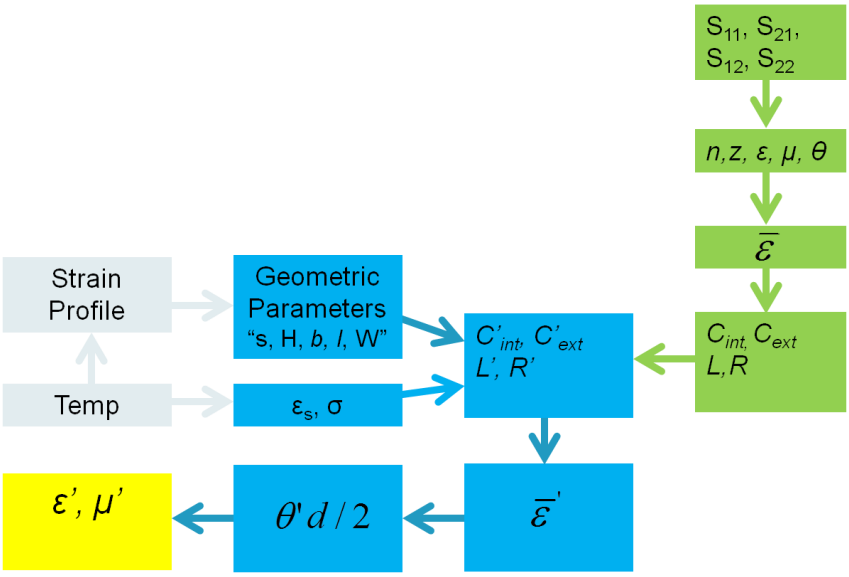

Figure 51. *Flow diagram for determining strain- and/or temperature-dependent permittivity and permeability. The green boxes denote values from the baseline structure. Light grey boxes denote values from a mechanical/thermal FEM package. Utilizing these inputs, simple scripts can be used to determine the new geometry, material properties, and equivalent circuit parameters. These eventually lead to the definition of the metamaterial's permittivity and permeability for the given loading scenario.*

4.2 RECOMMENDATIONS FOR FUTURE WORK

This research effort marks an early attempt to fundamentally understand, and quantifiably describe, metamaterial strain- and temperature-dependence. As such, there remains ample fertile ground for future research. The following are just a few areas that would provide significant benefit for the engineering community attempting to transition metamaterials into a variety of systems and applications.

4.2.1 Magnetic Metamaterials

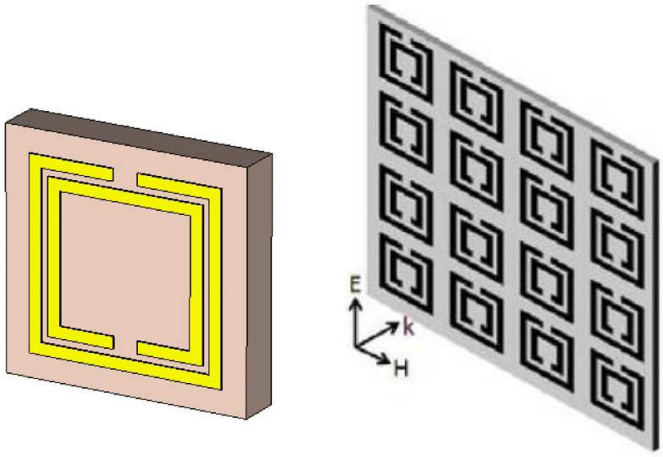

Figure 52. *Common design for Split-Ring Resonators (SRRs), which elicit a magnetic response to EM waves. Picture on left is from [32] and picture on right is from [82].*

The current effort focused on developing analytic expressions to describe the strain- and temperature-dependence of an electrically resonant metamaterial. However, magnetic resonators (such as those shown in Figure 52) are commonly used to excite a magnetic response to EM waves and are utilized to create negative permeability and negative index materials.

Analytically describing the strain- and temperature-dependence of the magnetic resonators will require the development of:

a) A new circuit model for the unit cell

The magnetic resonator will require the development of a new equivalent circuit model that captures its unique internal and external interactions. In particular, it must capture the loop and cell-to-cell inductive interactions that were not required for description of the electric resonator's behavior. Previous efforts in this area by Ricardo Marques' group [43][83][84] are likely to prove critical for this task.

b) New equivalent circuit expressions

For the electric resonator, the expressions negated the effects of loop inductance and mutual inductance between cells. However, these terms dominate the behavior of magnetic resonators. It is anticipated that the expressions for the capacitances and resistance, utilized for the current effort, can be leveraged for this purpose.

c) A new analytic expression describing the permeability of the metamaterial

The standard expressions for permittivity and permeability assume Drude-Lorentz-type resonant oscillation in the thin layer comprising the metamaterial. However, these forms are inexact and do not enable description via equivalent circuit elements. During this effort, the electrical resonator's wave impedance was utilized to develop a more exact form of the expression. Additionally, this form enabled direct description via the circuit parameters. To describe the behavior of magnetic resonators, an equivalent expression for magnetic response must be developed.

4.2.2 Off-Diagonal Permittivity and Permeability Terms

During the conduct of the current research effort, it was discovered when a polarization-independent unit cell (left picture in Figure 53) is subjected to shear strains, it will cause a rotation of the EM wave. In other words, this cell exhibits shear-dependent off-diagonal terms in the permittivity and permeability tensors (they are equal to zero in the unstrained state). However, there is currently no published work describing a process for retrieving the off-diagonal permittivity and permeability terms from numerical

simulations and/or empirical data (the only notable exception being the techniques from [23][24] that rely on the simulated creation of physically unrealizable magnetic currents to characterize fully bi-anisotropic structures).

Developing a parameter retrieval algorithm for off-diagonal terms will first require a general solution to the Fresnel equations using anisotropic media. These results could then be incorporated into the process detailed in [40][86] to create the appropriate retrieval algorithm. Additionally, performing the retrieval process will require attaining reflection and transmission data from 2 orthogonal polarizations.

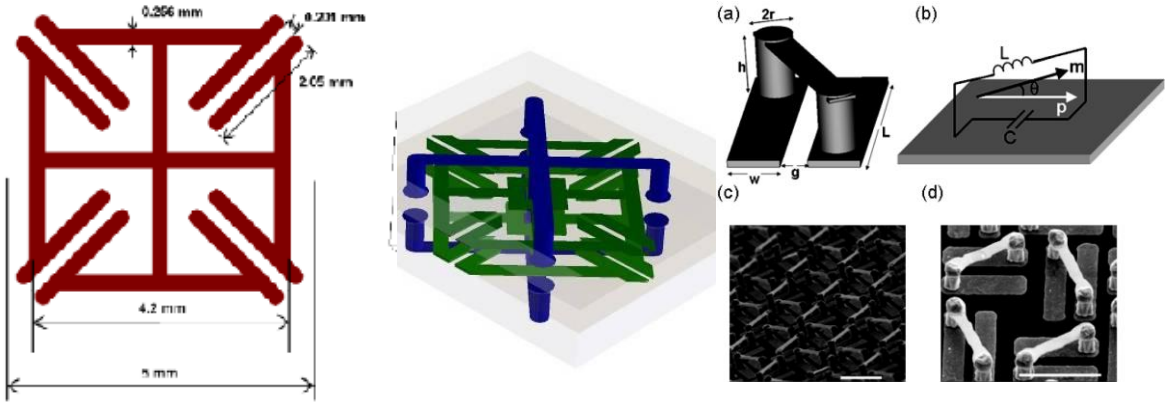

Figure 53. *On the left, a unit cell design that operates independent of polarization (assuming normal incidence). In the center, a fully isotropic unit cell: same performance independent of polarization and angle of incidence. Both courtesy of SensorMetrix [37]. On the right, a chiral metamaterial [85], which requires the definition of the coupling tensors (ξ and ζ).*

4.2.3 Terms in the Magneto-Electric Coupling Tensors

To develop a retrieval algorithm for the magnetoelectric coupling terms (ζ and ξ), one must again visit the Fresnel equations, and further generalize the solution to include bi-anisotropic media. It is hypothesized that a number of polarizations and/or angles of incidence coupled with the degree of non-reciprocity (The differences in the reflection

and transmission when the EM wave is propagated into and out of the plane of the metamaterial sample; i.e. in the + and – Z-direction in Figure 7.) will provide a sufficient number of equations with which to solve for the expanded set of unknowns required to fully characterize the material system.

It is important to note that there are currently NO analytic expressions for the off-diagonal permittivity and permeability or any of the coupling terms.

4.2.4 Effective Compliance Matrices

Efficient calculation of the mechanical and electromagnetic response of complex, composite parts is enabled via the utilization of continuum approaches. For metamaterials, the complex, subwavelength geometry of the unit cell implies effective medium properties for the incident EM radiation. These effective medium properties are the critical enabler for efficiently calculating ray-traces, and EM performance for large structures containing many thousands of unit cells exhibiting a multitude of unique cell designs.

Discretizing the mechanical and thermal models at the same level can enable efficient and seamless translation between these disparate physics, enabling rapid, physics-coupled optimization of load-bearing, EM-tailored structures for a variety of applications.

As discussed in Section 2.4, the relative stiffness contribution of the constituent layers (conductive traces and dielectric substrate) play a significant role in the strain-dependent EM response of metamaterial structures. Classical lamination theory, and other insights from the composite's industry may prove helpful in developing an overall

unit cell compliance; the 4th order tensor linking applied stress and resultant strain. This unit cell compliance could serve a critical role in enabling the metamaterial unit cell to serve as the representative volume element for mechanical and thermal modeling.

Typical metamaterial geometries and material choices imply that these compliance matrices will exhibit highly non-linear behavior. It is also paramount that elastic limits in the constituent materials are discerned and implemented in the mechanical modeling as feedback for any mechanical design and analysis activities.

Shear-lag models, modified to better accommodate the complexities of 3-D problems with finite dimensions, could more accurately predict strain-transfer between layers of the metamaterial structure. This would again serve as the bridge between strain at the unit cell level (global deformation) and changes in the pertinent dimensions in the equivalent circuit analytic expressions (local deformation).

4.2.5 Off-Resonant Structures

This research focused on analyzing a resonant metamaterial structure, at its resonant frequency. However, many metamaterial structures are non-resonant, or operate at frequencies far removed from the resonance. Many of these fit within the field of ε-only structures, and maintain values of $\mu=1$ and $\varepsilon\geq1$ throughout the volume of interest.

Resonant structures can provide extraordinary values for ε and μ, and enable strong interactions with EM waves over relatively few unit cells and exceedingly small length-scales. On the other hand, non-resonant metamaterials enable the attainment of exquisite, piece-wise control of the EM properties throughout the volume of a complex structure. As a result, non-resonant metamaterial structures typically require an EM wave to interact with 100s to 1000s of unit cells in order to create the designed ray tracing.

As shown during this research, resonant metamaterial structures have demonstrated significant strain- and temperature-sensitivities. This proposed effort would investigate the strain- and temperature-dependence of non-resonant metamaterial structures. While each non-resonant unit cell may be relatively insensitive to mechanical phenomena, the aggregation of the numerous interactions may lead to significant changes in the bulk metamaterial's EM performance. A significant question to address would be whether a similar process could provide the accuracy and precision necessary to correctly predict the propagation through 100s or 1000s of unit cells.

REFERENCES

[1] *American Heritage Science Dictionary* (Houghton Mifflin Company, Boston, MA, 2002)

[2] *Random House Dictionary* (Random House, Inc., New York, NY, 2008)

[3] Wood, J. ""The top ten advances in materials science" selected metamaterials as one of the Top Ten advances in materials in the last 50 years ." *Materials Today*, **11**, pp 40 (Jan 2008)

[4] The term "metamaterial" originated in a DARPA-DSO program of the same name. The DARPA definition of metamaterials is "a class of ordered nanocomposites that exhibit exceptional properties not readily observed in nature. These properties arise from qualitatively new response functions that are: (1) not observed in the constituent materials and (2) result from the inclusion of artificially fabricated, extrinsic, low dimensional inhomogeneities". See: http://www.darpa.mil/dso/thrust/matdev/metamaterials/index.html

[5] J. B. Pendry, A. J. Holden, W. J. Stewart, I. Youngs, "Extremely Low Frequency Plasmons in Metallic Mesostructures", *Physical Review Letters*, **76**, 4773 (1996)

[6] J. B. Pendry, A. J. Holden, D. J. Robbins, W. J. Stewart, "Low frequency plasmons in thin-wire structures," *Journal of Physics: Condensed Matter*, **10**, 4785 (1998)

[7] D. R. Smith, Willie J. Padilla, D. C. Vier, S. C. Nemat-Nasser and S. Schultz, "A composite medium with simultaneously negative permeability and permittivity", *Physical Review Letters*, **84**, 4184 (2000)

[8] R. Shelby, D. R. Smith and S. Schultz, " Experimental verification of a negative index of refraction", *Science*, **292**, 77 (2001)

[9] John Young, Director DDR&E, in a 24 August 2007 memo to Congress, identified metamaterials as an area of strategic investment for the Department of Defense, further warning that other nations are investing significant dollars, noting that the Chinese published over 250 papers on the topic in 2005. Estimated metamaterials Defense spending for 2008 was $30 to $50 million.

[10] J.B. Pendry, A.J. Holden, D.J. Robbins, and W.J. Stewart, "Magnetism from Conductors and Enhanced Nonlinear Phenomena," *IEEE Transactions on Microwave Theory and Techniques,* **47,** 0018-9480/99 (1999)

[11] T. Driscoll, D.N. Basov, A.F. Starr, P.M. Rye, S. Nemat-Nasser, D. Schurig, D.R. Smith, "Free-space Microwave Focusing by a Negative-index Gradient Lens," *Applied Physics Letters,* **88**, 081101 (2006)

[12] J.B. Pendry, "Negative Refraction Makes a Perfect Lens," *Physical Review Letters,* **85**, 3966 (2000)

[13] D. Schurig, J. Mock, B. Justice, S. Cummer, J.B. Pendry, A. Starr, D.R. Smith, "Metamaterial Electromagnetic Cloak at Microwave Frequencies," *Science,* **314**, 977 (2006)

[14] R. Liu, C. Ji, J.J. Mock, J.Y. Chin, T,J, Cui, D.R. Smith, "Broadband Ground-Plane Cloak," *Science,* **323**, 5912, pp 366-369 (2009)

[15] A. Ali, A., M.A. Khan, Z. Hu, "High Selectivity Lowpass Filter Using Negative ε Metamaterial Resonators," *Electronics Letters,* **43**, 9 (2007)

[16] N.I. Landy, S, Sajuyigbe, J.J. Mock, D.R. Smith, W.J. Padilla, "Perfect Metamaterial Absorber," *Physical Review Letters,* **100**, 207402 (2008)

[17] X. Zhang, and Z. Liu, "Superlenses to overcome the diffraction limit", *Nature Materials*, **7**, 435, (2008)

[18] J. B. Pendry, D. Schurig, D. R. Smith, "Controlling electromagnetic fields," *Science*, **312**, 1780 (2006)

[19] B.J. Justice, J.J. Mock, L. Guo, A. Degiron, D. Schurig, D.R. Smith, "Spatial Mapping of the Internal and External Electromagnetic Fields of Negative Index Metamaterials," *Optical Express*, **14**, 19, pp 8694-8705 (2006)

[20] D.J. Griffiths, *Introduction to Electrodynamics, Third Edition*, Prentice Hall, Upper Saddle River, NJ, 07458 (1999)

[21] P. Lorrain, D.P. Corson, F. Lorrain, *Electromagnetic Fields and Waves, Third Edition*, W.H. Freeman and Company, New York, NY (1988)

[22] D.R. Smith, "Analytic expressions for the constitutive parameters of magnetoelectric metamaterials," *Physical Review E*, **81**, 036605 (2010)

[23] C. Fietz, G. Shvets, "Metamaterial homogenization: extraction of effective constitutive parameters," *Metamaterials: Fundamentals and Applications II, Proceedings of the SPIE*, **7392**, 73920L-1 (2009)

[24] C. Fietz, G. Shvetz, "Current_Driven Metamaterial Homogenization," *Physica B: Condensed Matter*, **405**, 15, pp 2930-2934 (2010)

[25] M. Wegener, S. Linden, "Giving light another twist," *Physics*, **2**, 3 (2009)

[26] S. Zhang, Y-S. Park, J. Li, X. Lu, W. Zhang, X. Zhang, "Negative refractive index in chiral metamaterials," *Physical Review Letters*, **102**, 023901 (2009)

[27] H. Riesmann, P.S. Pawlik, *Elasticity: Theory and Applications*, Kreiger Publishing Company, Malabar, FL (1980)

[28] R. Melik, E. Unal, N.K. Perkgoz, C. Puttlitz, H.V. Demir, "Metamaterial-Based Wireless Strain Sensors," *Applied Physics Letters,* **95,** 011106 (2009)

[29] R. Melik, E. Unal, N.K. Perkgoz, C. Puttlitz, H.V. Demir, "Flexible Metamaterials for Wireless Strain Sensing," *Applied Physics Letters,* **95,** 181105 (2009)

[30] I. Pryce, K. Aydin, Y.A. Kelaita, R.M. Briggs, H.A. Atwater, "Highly Strained Compliant Optical Metamaterials with Large Frequency Tunability," *Nano Letters,* **10**, 4222 (2010)

[31] K.B. Alici, E. Ozbay, "Low-Temperature Behavior of Magnetic Metamaterial Elements," *New Journal of Physics,* **11**, 043015 (2009)

[32] V.A. Varadan, L. Ji, "Temperature Dependence of Resonances in Metamaterials," *IEEE Transactions on Microwave Theory and Techniques,* **58**, 10, pp 2673-81 (2010)

[33] H. Nemec, P. Kuzel, F. Kadlec, C. Kadlec, R. Yahiaoui, P. Mounaix, "Tunable Terahertz Metamaterials with Negative Permeability," *Physical Review B,* **79**, 241108 (2009)

[34] J. Han, A. Lakhtakia, "Semiconductor Split-Ring Resonators for Thermally Tunable Terahertz Metamaterials," *Journal of Modern Optics,* **56**, 4, pp 554-557 (2009)

[35] S. Xiao, U.K. Chettier, A.V. Kildishev, V. Drachev, I.C. Choo, V.M. Shalaev, "Tunable Magnetic Response of Metamaterials," *Applied Physics Letters,* **95**, 033115 (2009)

[36] D. Schurig, J.J. Mock, D.R. Smith, "Electric-Field-Coupled Resonators for Negative Permittivity Metamaterials," *Appl. Phys. Lett.,* **88**, 041109 (2005)

[37] SensorMetrix, Inc, 10211 Pacific Mesa Blvd, Ste 408, San Diego, CA 92121

[38] Rogers Corporation, 100 S. Roosevelt Ave, Chandler, AZ 85226

[39] ANSYS, Inc., Southpointe, 275 Technology Dr., Canonsburg, PA 15317, USA

[40] D. R. Smith, D.C. Vier, Th. Koschny, C.M. Soukoulis, "Electromagnetic Parameter Retrieval from Inhomogeneous Metamaterials," *Phys. Rev. E*, **71**, 036617 (2005)

[41] Y.A. Urzhumov, "Sub-Wavelength Electromagnetic Phenomena in Plasmonic and Polaritonic Nanostructures," PhD Dissertation, University of Texas at Austin (2007)

[42] M. Becchi, C. Oldano, and S. Ponti, "Spatial Dispersion and Optics of Crystals," *Journal of Optics A: Pure and Applied Optics*, **1**, pp. 713-718 (1999)

[43] J.D. Baena, J. Bonache, F. Martin, R. Marques Sillero, F. Falcone, T. Lopetegi, M.A.G. Laso, J. Garcia-Garcia, I. Gil, M.F. Portillo, M. Sorolla, "Equivalent-Circuit Models for Split-Ring Resonators and Complimentary Split-Ring Resonators Coupled to Planar Transmission Lines," *IEEE Trans. Micro. Theory and Tech.*, **53**, 4, pp 1451-61 (2005)

[44] S. Sajuyigbe, B. Justice, A. Starr, D.R. Smith, "Design and analysis of three-dimensionalized ELC Metamaterial Unit Cell," *IEEE Antennas and Wireless Propagation Letters*,**8**, 1268-1271 (2009)

[45] S. Sajuyigbe, M. Ross, P. Geren, S.A. Cummer, M.H. Tenalian, D.R. Smith, "Wide angle impedance matching metamaterials for waveguide-fed phased-array antennas," *IET Microwaves, Antennas, and Propagation*, **4**, 8, pp 1063-1072 (2010)

[46] K. Siwiak, T. Dowling, L. Lewis, "Boresight errors induced by missile radomes," *IEEE Transactions on Antennas and Propagation*, **27**, 6, pp 832-841 (1979)

[47] C. Fietz, C, G Shvets, "Metamaterial homogenization: extraction of effective constitutive parameters," *Metamaterials: Fundamentals and Applications II, Proceedings of the SPIE*, **7392**, 73920L-1 (2009)

[48] J. Lubliner, *Plasticity Theory* (Pearson Education, Inc., Upper Saddle River, NJ, 2006)

[49] S, Cummer, B.-I. Popa, D. Schurig, D. Smith, and J. Pendry, "Full-Wave Simulations of Electromagnetic Cloaking Structures," *Phys. Rev. E* **74**, 036621 (2006)

[50] B.J. Arritt, B. Adomanis, T. Khraishi, D.R. Smith, "Parametric Analysis of the Strain-Dependent Behavior of a Metamaterial Electric Resonator," *Applied Physics Letters*, **98**, 191907 (2010)

[51] O. G. Vendik, S. P. Zubko, and M. A. Nikol'skii, "Modeling and Calculation of the Capacitance of a Planar Capacitor Containing a Ferroelectric Thin Film," *Tech. Phys.* **44**, No 4, 349 (1999)

[52] E. B. Rosa, *Bulleting of the Bureau of Standards*, **4**, (Washington Government Printing Office, Washington DC, 1908)

[53] W. Withayachumnankul, C. Fumeaux, D. Abbott, "Compact Electric-LC Resonators for Metamaterials," *arXiv:1009.0139v1 [Physics.Optics]* (2010)

[54] B.J. Arritt, D.R. Smith, T.A. Khraishi, "Equivalent Circuit Analysis of Metamaterial Strain-Dependent Effective Medium Parameters," *Journal of Applied Physics*, **109**, 073512 (2011)

[55] MathWorks, 3 Apple Hill Drive, Natick, MA 01760-2098, USA

[56] S. Tretyakov, *Analytical Modeling in Applied Electromagnetics*, (Artech House, Boston, MA, 2003), p. 146

[57] COMSOL, Inc., 10850 Wilshire Blvd, Suite 800, Los Angeles, CA 90024, USA

[58] S.A. Martin, J.L. Blackshire, "Effect of Adhesive Material Properties on Induced Stresses in Bonded Sensors," *Defense Technical Information Center report number AFRL-ML-WP-TP-2006-476,* approved for public release (2006)

[59] J.L. Blackshire, S.A. Martin, A. Cooney, "Characterization and Modeling of Bonded Piezoelectric Sensor Performance and Durability in Simulated Aircraft Environments," *Proceedings of the Third European Workshop on Structural Health Monitoring*, pp 283-289, Granada, Spain (2006)

[60] U.A. Handge, "Analysis of a shear-lag model with nonlinear elastic stress transfer for sequential cracking of polymer coatings," *Journal of Materials Science*, **37**, 4775-4782 (2002)

[61] J. Sirohi, I. Chopra, "Fundamental Understanding of Piezoelectric Strain Sensors," *Journal of Intelligent Material Systems and Structures,* **11**, 246 (2000)

[62] W.B. Fraser, "Bending of a stretched plate containing an eccentrically plate reinforced hole of arbitrary shape," *International Journal of Solids and Structures*, **11**, pp 1245-1256 (1975)

[63] C. Haag, H. Suhr, "Improved Adhesion of Pre-Etched Polytetrafluoroethylene by PECVD Deposited Thin Metallic Layers," *Applied Physics A,* **47,** 199-203 (1988)

[64] G.T. Mase, G.E. Mase, *Continuum Mechanics for Engineers*, (CRC Press, New York, NY, 1999), pg 242

[65] DuPont, 1007 Market St., Wilmington, DE 19898, USA

[66] ASTM D3039-08 “Standard Method for Tensile Properties of Polymer Matrix Composite Materials”

[67] ASTM D882-10 “Standard Test Method for Tensile Properties of Thin Plastic Sheeting”

[68] Instron, 825 University Ave, Norwood, MA 02062, USA

[69] Wyoming Test Fixtures, Inc., 2960 E. Millcreek Canyon Rd., Salt Lake City, UT 84109, USA

[70] Agilent Technologies, Inc., 5301 Stevens Creek Blvd., Santa Clara, CA 95051, USA

[71] Rosendal Associates, Inc., 9530 Pathway St., Suite 101, Santee, CA 92071, USA

[72] Nikon, Fuji Bldg., 2-3 Marunouchi 3-chome, Chiyoda-ku, Tokyo 100-8331, Japan

[73] Vicon, 5419 McConnell Ave., Los Angeles, CA 90066, USA

[74] EOS Systems, Inc., 210-1847 W. Broadway, Vancouver, British Columbia, Canada V6J 1Y6

[75] B.J. Arritt, D.R. Smith, T.A. Khraishi, “Analytically Describing the Temperature-Dependent Constitutive Parameters of a Metamaterial,” submitted to the *Journal of Intelligent Materials and Structural Systems*

[76] J.R Wertz, W.J. Larson, *Space Mission Analysis and Design, 3rd Edition* (published jointly by Microcosm Press, Hawthorne, CA and Springer, New York, NY, 2007)

[77] J. Krupka, K. Derzakowski, B. Riddle, J. Baker-Jarvis, “A Dielectric Resonator for Measurements of Complex Permittivity of Low Loss Dielectric Materials as a Function of Temperature,” *Meas. Sci. Tech.*, **9**, 1751-1756 (1998)

[78] J.-M. Heinola, J.P. Strom, "Evaluation of Dielectric Properties of Printed Wiring Board Materials by Using a Microstrip-ring and Strip-line Ring Resonator Methods," *IEEE Elec. Insul. Mag.*, **23**, 3, pp 23-29 (2007)

[79] S.-Y. Chiam, R. Singh, W. Zhang, A.A. Bettiol, "Controlling Metamaterial Resonances via Dielectric and Aspect Ratio Effects," *Applied Physics Letters*, **97**, 191906 (2010)

[80] M. Vukadinovic, B. Malik, M. Kosec, D. Krizaj, "Modelling and Characterization of Thin Film Planar Capacitors: Inherent Errors and Limits of Applicability of Partial Capacitance Methods," *Measurement Science and Technology*, **20**, 115106 (2009)

[81] D.R. Smith, D.C. Vier, W. Padilla, S.C. Nemat-Nasser, S. Schultz, "Loop-wire Medium for Investigating Plasmons at Microwave Frequencies," *Appl. Phys. Lett.*, **75**, 101425 (1999)

[82] R. Melik, E. Unal, N.K. Perkgoz, B. Santoni, D. Kamstock, C. Puttlitz, H.V. Demir, "Nested Metamaterials for wireless strain sensors," *IEEE Journal of Selected Topics in Quantum Electronics*, **16**, 2 (2010)

[83] R. Marques, F. Mesa, J. Martel, F. Medina, "Comparative analysis of the edge- and broadside-coupled split ring resonators for metamaterial design-theory and experiments," *IEEE Trans. on Antennas and Propagation*, **51**, 10 (2003)

[84] R. Marques, F. Medina, R. Rafii-El-Idrissi, "Role of bianisotropy in negative permeability and left-handed metamaterials," *Phys. Rev. B*, **65**, 144440 (2002)

[85] S. Zhang, Y-S. Park, J. Li, X. Lu, W. Zhang, X. Zhang, "Negative refractive index in chiral metamaterials," *Phys. Rev. Letters*, **102**, 023901 (2009)

[86] Smith, D.R., S. Schultz, P. Markos, C.M. Soukoulis, "Determination of Effective Permittivity and Permeability of Metamaterials from Reflection and Transmission Coefficients," *Physical Review B,* 65, 195104 (2002)

APPENDIX: CONSISTENCY OF THE SAMPLE FRONT PLANE

The information regarding phase advance is critical for performing parameter retrievals (using either modeling or test data) to determine the material's EM constitutive properties (permittivity and permeability). However, at the beginning of this effort, there were significant concerns regarding the movement of the front plane during testing; specifically during the switch between the calibration and test samples. If the front plane moved significantly between samples, it would artificially shift the phase advance across the cell, resulting in complications within the retrieval code and errors in the interpretation of the test data.

The use of the relatively rigid mechanical loadframe helps to minimize a great deal of flexibility in the system and provided a stable platform when switching samples. However, the design of the wedge grips allowed a significant amount of rotational laxity about the loadframe's loading axis. To minimize the potential movement from this degree of freedom, retro-reflective tape and a laser level (oriented to project a plane vertically) were utilized to maintain a consistent orientation of the samples.

The following process was used to place the samples into the loadframe:

1) The wedge grips are aligned with each other, using a thick piece of metal plate-stock, and all mechanical connections within the load path are tightened. This minimizes the potential for rotation of the sample, after load is applied.

2) The laser level is aligned with targets (lines) on the retro-reflective tape. A major assumption of this process is that the loadframe provides a consistent loading axis, while the laser level projects another line onto the

wedge grips. Both lines now define a consistent plane in 3D space that will be used for all subsequent alignment steps.

3) The plate-stock is removed, and the calibration sample is placed in the wedge grips. During the switch between samples, the loading axis is assumed stationary, and the projected laser beam is used to align the retro-reflective targets.

4) Other samples can similarly be characterized, as long as the new samples are the same thickness and the grips are again aligned with the laser level.

To ensure the quality and consistency of this alignment process, the Air Force Research Laboratory/Space Vehicles Directorate's Vicon™ IR (Infra-Red) Motion Capture System [1] (camera depicted in Figure 54) was utilized to quantify the degree of movement when switching between samples. The test sample was a 10mil thick piece of spring steel. A low-stiffness sample was purposefully chosen in order to provide the worst case potential for movement, as it was repeatedly switched in and out of the wedge grips. The sample was outfitted with the two kinds of retro-reflective targets; spheres and circles, as detailed in Figure 55. Three IR cameras were utilized to enable high-accuracy triangulation of the retro-reflective targets.

Figure 54. *Vicon™ IR Camera*

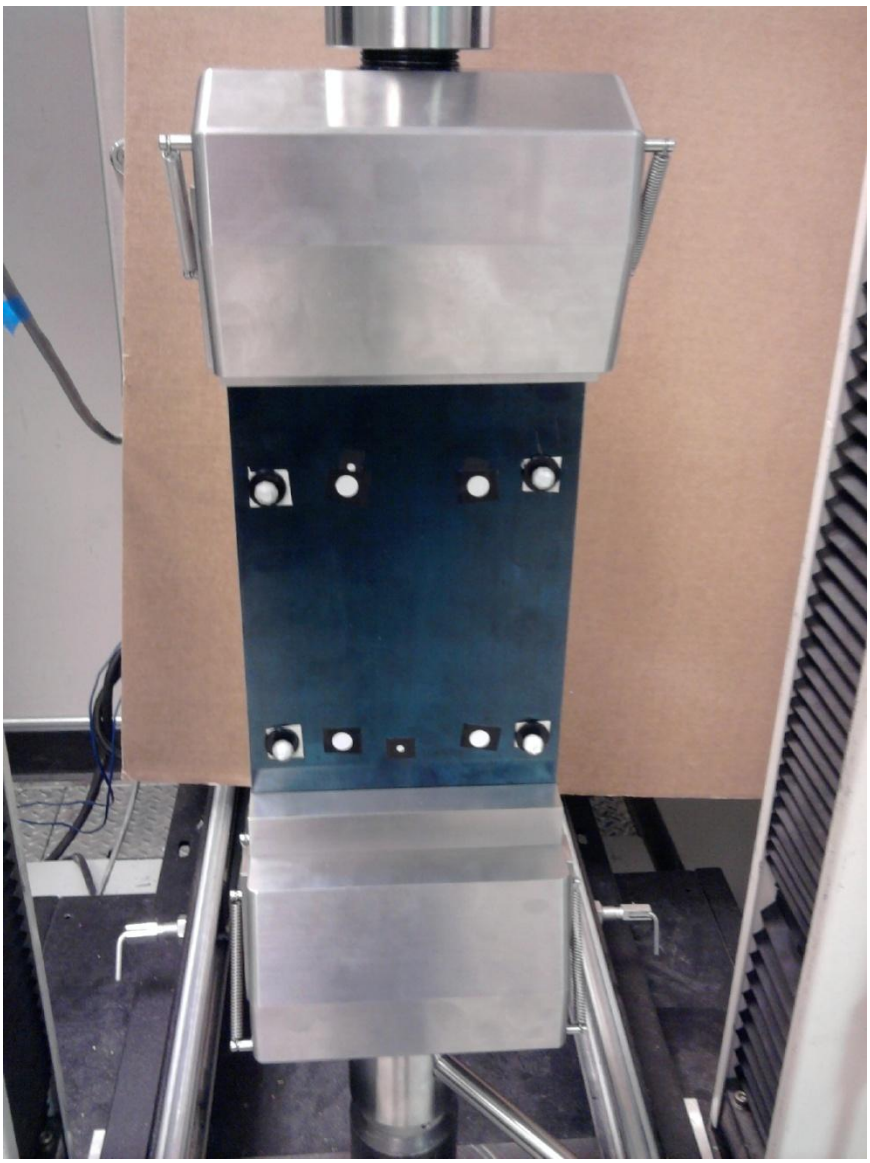

Figure 55. *Sample for front-plane movement tests. Includes two kinds of retro-reflective targets for increased confidence in the results; spheres and circles.*

Calibration of the Vicon™ system was relatively simple; a curved wand, with retro-reflective targets and known dimensions, was waved within the test volume as the cameras record the movement. The system then uses that data to determine the location of each of the cameras. Once the positions of the cameras are known, the system can use triangulation to determine locations during the actual test.

For these tests, data was taken at 120 Hz for 2 seconds. A baseline reading was taken, followed by ten trials, each featuring a full removal, replacement, and alignment of the test sample. Within each of the individual trials, the standard deviation in the data was routinely below 0.01 mm (10^{-5} m).

Table 8 shows the results from the testing. All measurements are in mm. Note the Standard Deviation and Delta (maximum difference between trials) near the bottom of the table. Even for the spherical targets (which have lower spatial resolution in the Z-direction), all values are under 1mm. The testable frequency range for this project is 8.2 to 12.4 GHz. The freespace wavelength at 12.4 GHz is approximately 24 mm; meaning that the *maximum* anticipated error due to front plane movement is on the order of $\lambda/25$. A search of the literature and vendor websites [2-7] shows that an error of less than $\lambda/20$ is commonly used as the reference standard for delineating extremely high quality optics.

	S1	S2	S3	S4	D1	D1	D3	D4		Planarity Check
	Z	Z	Z	Z	Z	Z	Z	Z		
Trail 0	57.24	57.77	56.37	57.24	49.24	49.12	49.67	49.84		0.03
Trial 1	57.18	57.76	55.80	57.70	48.90	49.29	49.63	49.82		0.65
Trial 2	57.27	57.67	56.37	57.71	49.34	49.38	49.69	49.77		0.13
Trial 4	57.21	57.89	56.50	57.52	49.40	49.37	49.69	49.91		0.18
Trial 5	57.04	57.71	56.07	57.52	49.07	49.15	49.55			0.04
Trial 6	57.01	57.73	56.28	57.18	49.17	48.99	49.53	49.78		0.45
Trial 7	56.92	57.77	56.06	57.55	49.07	49.16	49.47	49.82		0.40
Trial 8	56.97	57.73	56.23	57.75	49.25	49.34	49.51	49.80		0.08
Trial 9	56.96	57.72	56.37	57.33	49.26	49.08	49.50	49.79		0.29
Trial 10	56.62	58.35	56.77	56.98	49.50	49.04	49.34	50.17		
Average	57.04	57.81	56.28	57.45	49.22	49.19	49.56	49.85		0.25
Standard deviation	0.19	0.20	0.26	0.26	0.17	0.14	0.11	0.12		0.21
Min	56.62	57.67	55.80	56.98	48.90	48.99	49.34	49.77		0.03
Max	57.27	58.35	56.77	57.75	49.50	49.38	49.69	50.17		0.65
Delta	0.65	0.69	0.96	0.77	0.60	0.40	0.35	0.40		0.62

Table 8. *Results from the testing with the Vison™ Motion Capture System. Trail 5, D4 is omitted due to apparent obscuration issues during that particular trial. On the top row, "S" refers to a spherical target and "D" stands for dot, referring to a flat, circular target. All measurements are given in mm.*

A check on the planarity of the sample was also performed, to further assess the quality of the data. Three of the dot targets, for each trial, were used to define the plane of the sample. The column to the far right of Table 8 shows the error between the plane and the location of the fourth dot. As the table shows, all error values are significantly less than 1mm.

Thus, the conclusion is that the alignment process provides the necessary consistency to enable quality data during the microwave interrogations.

References for Appendix:

[1] Vicon-Los Angeles, 5419 McConnell Ave, Los Angeles, CA, 90066, USA

[2] Linjie, L, RG Gattass, E Gershgoren, H Hwang, JT Fourkas, "Achieving λ/20 Resolution in One-Color Initiation and Deactivation of Polymerization," *Science*, **324**, 5929, pp 910-913, (2009)

[3] Rigaut, F, D Salmon, R Arsenault, J Thomas, O Lai, D Rouan, JP V'eran, D Crampton, JM Fletcher, J Stilburn, "Performance of the Canada-France-Hawaii Telescope Adaptive Optics Bonnette," *Publications of the Astronomical Society of the Pacific*, **110,** pp 152-164 (1998)

[4] www.photonicsonline.com/article.mvc/optical-surfaces-announces-highly-apheric-0001

[5] www.optotl.com/opts

[6] www.opcolab.com/page144.html

[7] http://www.p-wholesale.com/cn-pro/19/770to1/optical-parallel-and-plane-mirror-lqv-0846-701716.html